

---

Bulk and Structure Inversion  
Asymmetry in Semiconductor Quantum  
Well Structures

---



DISSERTATION

zur Erlangung des Doktorgrades der Naturwissenschaften  
doctor rerum naturalium  
(Dr. rer. nat.)  
der Fakultät für Physik  
Universität Regensburg  
im Mai 2012

vorgelegt von  
Dipl.-Phys. Vera Lechner  
geboren am 06.07.1983 in Trostberg

Die Arbeit wurde von Prof. Dr. Sergey D. Ganichev angeleitet.

Das Promotionsgesuch wurde am 14. Mai 2012 eingereicht.

Das Kolloquium fand am 19. Juli 2012 statt.

**Prüfungsausschuss:**

Vorsitzender: Prof. Dr. Tilo Wettig  
1. Gutachter: Prof. Dr. Sergey D. Ganichev  
2. Gutachter: Prof. Dr. Christian Schüller  
weiterer Prüfer: Prof. Dr. Josef Zweck



## Contents

<b>1</b>	<b>Introduction</b>	<b>4</b>
<b>2</b>	<b>Physical background</b>	<b>8</b>
2.1	Spin-orbit interaction . . . . .	9
2.1.1	Band structure in 3-dimensional semiconductors . . . . .	9
2.1.2	Band structure in 2-dimensional semiconductors . . . . .	11
2.1.3	Origin of the $\mathbf{k}$ -linear and $\mathbf{k}$ -cubic terms . . . . .	13
2.2	THz radiation induced photocurrents . . . . .	20
2.2.1	Magneto-gyrotropic photogalvanic effect . . . . .	21
2.2.2	Spin-galvanic effect . . . . .	25
2.2.3	Circular photogalvanic effect . . . . .	28
2.3	Spin relaxation mechanisms . . . . .	30
2.3.1	D'yakonov-Perel' mechanism . . . . .	31
2.3.2	Elliott-Yafet mechanism . . . . .	32
2.4	Weak localization and weak antilocalization . . . . .	33
<b>3</b>	<b>Experimental methods</b>	<b>36</b>
3.1	THz laser source . . . . .	36
3.2	Variation of the laser radiations's polarization state . . . . .	38
3.3	Experimental setup and calibration . . . . .	43
3.4	Description and preparation of the studied samples . . . . .	45
3.4.1	Set I: GaAs QWs differing in the doping position . . . . .	46
3.4.2	Set II: GaAs QWs differing in the well width . . . . .	48
3.4.3	Set III: InGaAs QWs differing in the well width . . . . .	49
3.4.4	Sample preparation . . . . .	50

3.5	Time-resolved Kerr rotation and Photoluminescence measurements . . . . .	51
3.6	Magneto transport measurements . . . . .	53
<b>4</b>	<b>Influence of the <math>\delta</math>-doping position on BIA and SIA</b>	<b>54</b>
4.1	Experimental results . . . . .	56
4.2	Discussion . . . . .	59
4.3	Summary . . . . .	61
<b>5</b>	<b>Study of BIA and SIA in InGaAs quantum wells</b>	<b>63</b>
5.1	Photocurrent measurements . . . . .	65
5.1.1	Experimental results . . . . .	65
5.1.2	Discussion . . . . .	72
5.2	Magneto-transport measurements . . . . .	75
5.2.1	Experimental results . . . . .	75
5.2.2	Discussion . . . . .	77
5.3	Summary . . . . .	81
<b>6</b>	<b>Spin and orbital mechanisms of the MPGE</b>	<b>83</b>
6.1	Sample characterization by PL and TRKR techniques . . . . .	85
6.2	Linear MPGE . . . . .	88
6.2.1	Experimental results . . . . .	88
6.2.2	Discussion . . . . .	90
6.3	Circular MPGE . . . . .	96
6.3.1	Experimental results . . . . .	96
6.3.2	Discussion . . . . .	98
6.4	Summary . . . . .	101
<b>7</b>	<b>Conclusions</b>	<b>103</b>

*CONTENTS*

3

**References**

**106**

## 1 Introduction

In recent years, great efforts have been made in solid state physics to extend the understanding of spin-dependent phenomena [1]. Consequently, spintronics [2], which is based on the electron's spin degree of freedom, became a fast growing research area and draw much interest, since it promises a change in information technology [3]. Key tasks in spintronics are the detection, manipulation and generation of spin polarized electrons in low dimensional semiconductors [4–6]. A versatile instrument to obtain these goals provides spin-orbit coupling, which lifts the spin degeneracy of the energy bands in quantum wells (QWs) based on III-V semiconductors [7]. The zero field spin splitting permits for example the control of the spin polarization via a gate voltage [8, 9], can be utilized for all-electric spin injection and determines the spin relaxation rate. The removal of the spin degeneracy is a consequence of the spin-orbit interaction and described by Rashba and Dresselhaus terms in the effective Hamiltonian  $H_{\text{SO}} = H_{\text{R}} + H_{\text{D}}$ , with:

$$\begin{aligned} H_{\text{R}} &= \alpha(k_y\sigma_x - k_x\sigma_y), \\ H_{\text{D}} &= \beta(k_x\sigma_x - k_y\sigma_y) + \gamma(-\sigma_x k_x k_y^2 + \sigma_y k_y k_x^2), \end{aligned}$$

where  $\sigma_x$  and  $\sigma_y$  are the Pauli spin matrices [1]. While the Rashba spin splitting [10] is linear in the electron wave vector  $\mathbf{k}$ , the Dresselhaus spin-orbit interaction (SOI) [11] consists of terms linear and cubic in  $\mathbf{k}$ . However, the cubic contributions are usually neglected, especially in materials with weak SOI as GaAs QWs. The microscopic origin of Rashba and Dresselhaus spin-orbit terms, is the structure and bulk inversion asymmetry (SIA and BIA), respectively [4–6]. The strength of the linear BIA-induced spin splitting,  $\beta = \gamma \langle k_z^2 \rangle$  (where  $\gamma$  is a material parameter), stems from crystal fields and depends on the QW width, temperature, and electron density. In contrast, SIA is caused by the confining potential. A common technique to control the strength of the SIA-induced splitting,  $\alpha$ , consists in using a gate electric field. Recently, it was shown that the built-in electric field in doped (110)-oriented GaAs QWs, due to a suitable choice of the  $\delta$ -doping layer position, allows to grow structures with controllable SIA [12]. The aim of this work is, to investigate the

anisotropy of the band spin splitting, which is caused by the interference of BIA and SIA. Furthermore, basic rules for the design of QW structures with a defined SIA/BIA-ratio should be obtained. These goals can be achieved applying a newly developed method, based on the analysis of the anisotropy of the magnetogyrotropic photogalvanic effect (MPGE). Additionally, photocurrents resulting from the circular photogalvanic effect (CPGE) as well as the spin-galvanic effect (SGE) are employed for this purpose. A further aim is to study the microscopic origin of the here used MPGE.

In the first part of this work, the MPGE is used to investigate SIA and BIA in (001)-grown GaAs/AlGaAs QWs regarding their dependence on the position of the  $\delta$ -doping layer [7]. Hereby, the role of the segregation and its influence on SIA shall be clarified. Furthermore, the experiments are aimed to estimate the growth parameters for QW structures with predetermined SIA. Herewith, QWs with almost equal Rashba and Dresselhaus spin splittings get achievable. In this case, if the  $\mathbf{k}$ -cubic terms can be neglected, a special situation occurs:  $\alpha = \pm\beta$  [13]. Now, the spin relaxation is suppressed [14, 15]. Due to the co-linear alignment of the effective magnetic field, resulting from Rashba and Dresselhaus spin splitting, any spin precesses around one fixed axis, which results in spatially periodic modes [15] referred to as persistent spin helix (PSH) [16]. The PSH is robust against all forms of spin-independent scattering. This leads to an advantageous situation: On the one hand, the spin relaxation is suppressed, while, on the other hand, the spin degree of freedom can still be controlled by a gate voltage. Hereby, diverse theoretical proposals for future spintronic applications arise [15, 17, 18], which use the tuneability of  $\alpha$  via a gate voltage, to reach  $\alpha = \beta$ .

In the second part, the usually neglected  $\mathbf{k}$ -cubic Dresselhaus terms and their influence on the formation of a PSH are considered. Hence, BIA and SIA are investigated in InGaAs/InAlAs QWs, which are characterized by a strong SOI and the substantial contribution of  $\mathbf{k}$ -cubic terms [13]. The questions, if a PSH survives under these conditions and how robust it is in this general case, will be considered by two independent, optical and transport, experiments as well as numerical analyses. At this, the CPGE as well as the SGE allow to estimate the  $\alpha/\beta$ -ratio, due to the phenomenological equivalence of the second rank

pseudo tensors describing spin splitting and photogalvanic effects. Furthermore, the investigation of quantum corrections to the magneto-conductance reveals information on the role of the cubic terms.

As yet, Rashba and Dresselhaus terms were analyzed, using the phenomenological equivalence of the corresponding second rank pseudo tensors. At the same time, the microscopic origin of the photocurrent is an important issue. Therefore, two mechanisms - spin-related and spin-independent - are addressed in the literature. Actually, an interplay of spin and orbital mechanisms is expected for the magnetogyrotropic photogalvanic effect. The spin-related mechanisms of the MPGE have already been widely discussed in the past (see Section 2.2), however, also orbital mechanisms were proposed [19, 20].

In the last part of this work, two roots of the MPGE, the linear and the circular MPGE, are investigated in GaAs/AlGaAs QWs of different width, concerning the interplay of spin and orbital mechanisms [21]. The realized experiments are dedicated to a clear distinction between both mechanisms underlying the MPGE formation. Herewith, the existence of orbital mechanisms in the linear as well as the circular MPGE shall be evidenced. To discriminate between both mechanisms, their qualitatively different behavior upon a variation of the  $g^*$  factor, which depends on the well width in GaAs/AlGaAs QWs, is utilized.

This thesis is organized as follows. Chapter 2 starts with the theoretical background, which is important to study Rashba and Dresselhaus spin-splittings, utilizing different photocurrents. First, the impact of the SOI on the band structure of 2D and 3D semiconductor systems, based on zinc-blende structure, is introduced and the resulting spin-splitting covered. Subsequently, THz radiation induced electric currents occurring in gyrotropic media, will be discussed with their phenomenological descriptions and microscopic models. Additionally, the most important spin-relaxation mechanisms are introduced. Finally, the weak anti-localization, which is a further effect of BIA and SIA, and its connection with the weak localization are presented. In Chap. 3, the experimental methods including the functionality of the THz laser, optic components influencing the polarization state of light as well as the whole experimental setup are implemented. Furthermore, details and properties of the studied samples are presented. Based on these fundamentals, the next chapters are aimed to

the experimental results, obtained in this work. In Chap. 4, BIA and SIA are investigated in GaAs/AlGaAs QWs upon a variation of the  $\delta$ -doping position. Afterwards, in materials with a strong SOI, the influence of  $\mathbf{k}$ -cubic terms on the Rashba/Dresselhaus spin-splitting is analyzed. Therefore, in Chap. 5 experiments concerning BIA and SIA in InGaAs/InAlAs QWs of different widths are addressed. Finally, another interesting question on the microscopic origin of the magneto-gyrotropic photogalvanic effect (MPGE) is treated. Chap. 6 discusses the interplay of spin and orbital mechanisms in two roots of the MPGE, namely the linear and the circular MPGE. Both mechanisms, underlying the current formation, are experimentally and theoretically investigated. Last but not least, all findings, obtained in this work, will be summarized in the conclusions.

## 2 Physical background

This chapter introduces the theoretical background, whereon the present work is based. It starts with the spin-orbit interaction (SOI), which is crucial for this work, since all phenomena discussed here are associated with it. This effect can be derived from the relativistic Dirac equation [22]. It describes the coupling of the electron's spin and orbital momentum degrees of freedom via the magnetic field  $\mathbf{B}_{\text{so}}$  that arises in the rest frame of an electron due to its motion in an electric field. In gyrotropic quantum wells (QWs) based e.g. on III-V semiconductors this coupling causes a spin-dependent force for moving electrons. As a result terms, linear in the electron wave vector  $\mathbf{k}$  and in the spin Pauli matrix  $\boldsymbol{\sigma}$ , emerge in the Hamiltonian and the spin degeneracy of the energy bands is removed. First, the resulting band structure and following the  $\mathbf{k}$ -linear as well as  $\mathbf{k}$ -cubic terms will be discussed in particular. The  $\mathbf{k}$ -linear terms in the Hamiltonian describe the spin splitting and can be divided into Dresselhaus and Rashba terms, which are mainly investigated in this work and thus, analyzed. Their microscopic origins are the bulk and structure inversion asymmetry (BIA and SIA), respectively. As next important issue, spin photocurrents are discussed, which in this work are mainly used as a tool to investigate BIA and SIA. Hereby, three effects occurring in gyrotropic media were applied: First, the magneto-gyrotropic photogalvanic effect (MPGE), which yields a spin polarized current due to the conversion of spin currents into an electric current via an external magnetic field. Second, the spin-galvanic effect (SGE), where the asymmetric relaxation of an in-plane nonequilibrium spin polarization results in an electric current. And third, the circular photogalvanic effect (CPGE), here a photocurrent originates on account of the asymmetric excitation of charge carriers in  $\mathbf{k}$ -space via circularly polarized light. In the following, these effects are explained with their phenomenological equations and microscopic models. Furthermore, this chapter covers the main spin relaxation mechanisms for (001)-grown zinc-blende structure based QWs. It discusses the D'yakonov-Perel' mechanism, which describes the spin relaxation as precession around effective magnetic fields. Additionally, the Elliott-Yafet mechanism, where the electron loses its spin orientation during a collision with an impurity, is considered. The Bir-Aronov-Pikus mechanism is just briefly

mentioned, since it explains the spin-flip relaxation due to scattering on holes, which is unimportant in  $n$ -type samples. Finally, weak antilocalization (WAL) and weak localization (WL) will be discussed in a few words. Hereby, the focus lies on their employment, in magneto-transport experiments, for the investigation of the Rashba/Dresselhaus ratio.

## 2.1 Spin-orbit interaction

### 2.1.1 Band structure in 3-dimensional semiconductors

Figure 1 illustrates the influence of the SOI on the dispersion relation of bulk semiconductors. It shows the  $s$ -type ( $l = 0$ ) conduction band (CB) states, which are separated by a direct band gap  $E_g$  from the  $p$ -type ( $l = 1$ ) valence band (VB) states. Here  $l$  is the atomic orbital angular momentum and  $m_l$  its projection on an arbitrary axis. Each state can be occupied by two electrons (spin-up and spin-down). The SOI leads to a removal of the 3-fold VB degeneracy ( $m_l = 0, \pm 1$ ), now  $\mathbf{L}$  and  $\mathbf{S}$  are no longer conserved separately but only

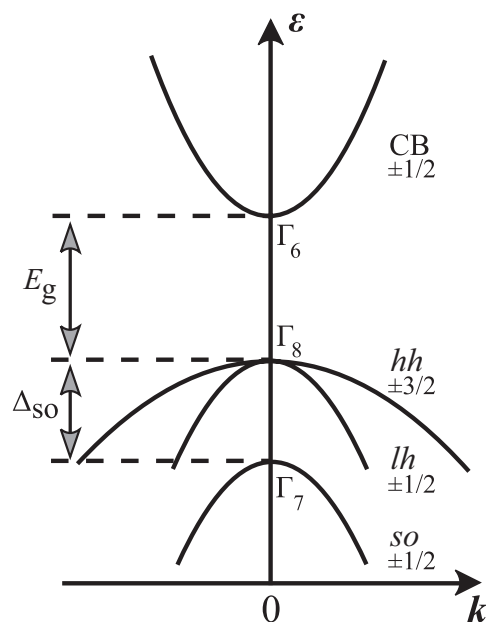


**Figure 1:** Band structure of a bulk semiconductor close to the  $\Gamma$ -point ( $\mathbf{k} = 0$ ) including SOI.

the total angular momentum  $\mathbf{J} = \mathbf{L} + \mathbf{S}$ . Hence, the VB state with  $l = 1$  is split into two states with  $j = 3/2$  and  $j = 1/2$ , while the CB state with  $l = 0$  is not affected. The 2-fold degenerated ( $J_z = \pm 3/2$ ) heavy hole band ( $hh$ ,  $j = 3/2$ ) and the 2-fold degenerated ( $J_z = \pm 1/2$ ) light hole band ( $lh$ ,  $j = 3/2$ ) are degenerated at the  $\Gamma$ -point, and both are separated in energy by the so called SO gap  $\Delta_{\text{SO}}$  from the 2-fold degenerated ( $J_z = \pm 1/2$ ) split-off band ( $so$ ,  $j = 1/2$ ). The weaker curvature of the  $hh$  band indicates the larger effective mass of the heavy holes compared to the light holes.  $\Delta_{\text{SO}}$  increases with the atomic mass, in e.g. GaAs it is about 0.3 eV ( $E_g \approx 1.46$  eV).

The spin degeneracy, visible in Figure 1, can be described as:

$$E_{\uparrow}(\mathbf{k}) = E_{\downarrow}(\mathbf{k}). \quad (1)$$

In Equation (1) spatial and time inversion symmetry are both fulfilled. The spatial inversion symmetry can be expressed via the energy of spin states:

$$E_{\uparrow}(\mathbf{k}) = E_{\uparrow}(-\mathbf{k}), \quad E_{\downarrow}(\mathbf{k}) = E_{\downarrow}(-\mathbf{k}), \quad (2)$$

and the time inversion symmetry yields the Kramers doublets:

$$E_{\uparrow}(\mathbf{k}) = E_{\downarrow}(-\mathbf{k}). \quad (3)$$

Commonly, the spin degeneracy can be removed by the application of an external magnetic field. Hereby, the time inversion symmetry is broken and, thus, the Kramers doublets exist no longer. Consequently, due to the Zeeman effect, the spin subbands are separated in energy. The strength of the Zeeman splitting is characterized by the effective Landé factor  $g^*$  that can strongly differ from the free-electron  $g$  factor  $g_0 = 2$ . This effective  $g$  factor is influenced by the SOI, as well. L. Roth et al. [23] first showed via  $\mathbf{k} \cdot \mathbf{p}$  method that the effective Landé factor  $g^*$  of an electron is connected with  $\Delta_{\text{SO}}$  and  $E_g$ . Following Ref. [24], this relation can be denoted as:

$$\frac{g^*}{g_0} = 1 - \frac{\Delta_{\text{SO}}}{3E_g + 2\Delta_{\text{SO}}} \left( \frac{m_0}{m^*} - 1 \right), \quad (4)$$

where  $m^*$  is the effective mass and  $m_0$  the mass of a free electron.

Usually, in bulk materials the spin degeneracy is removed by a magnetic field. To complete the picture, however, this degeneracy can also be removed in a

different way. Zinc-blende structure based bulk semiconductors have no crystal inversion center. Therefore, the spatial inversion symmetry is broken, which leads to the removal of spin degeneracy. Now,  $\mathbf{k}$ -cubic Dresselhaus terms are allowed in the Hamiltonian. While these terms are usually neglected, they lead to an additional, very small spin-splitting. In this case, the spin-up and spin-down parabolas are slightly shifted against each other along the  $\mathbf{k}$  axis. Thereby, as important fact, the Kramers doublets remain.

### 2.1.2 Band structure in 2-dimensional semiconductors

In low dimensional structures, as for example quantum wells, a 2-dimensional electron gas (2DEG) results, if the well width  $L_{\text{QW}}$  is smaller than the Fermi wave length  $\lambda_{\text{F}}$  of an electron in the corresponding material. As main effect, the confinement of the electrons along the growth direction  $z$ , leads to quantization. Hence, size-quantized subbands evolve in the conduction and valence band. Further, in 2-dimensional structures, the SOI removes the degeneracy of  $hh$  and  $lh$  band at the  $\Gamma$ -point [25]. At the same time, the spin degeneracy is not affected and remains. This is illustrated in Figure 2(a) for an inversion-symmetric structure.

Furthermore, the reduction of dimensionality causes a reduction of symmetry. Thus, a system with space inversion asymmetry, called gyrotropic medium, can arise. Gyrotropic media are materials with sufficient low symmetry, where the coupling of an axial  $A_m$  and a polar vector  $P_l$  via a second rank pseudo tensor  $M_{lm}$  is allowed:  $P_l = M_{lm}A_m$ . In such a structure certain components of axial (e.g. spin or magnetic field) and polar vectors (e.g. current or momentum) transform in the same way under all symmetry operations [26–28]. Typical for gyrotropic media is a spatial dispersion that depends linearly on the light or electron wave vector  $\mathbf{k}$  and yields optical activity (gyrotropy) or Rashba/Dresselhaus band spin-splitting in semiconductor structures, respectively [26, 28–31]. Required but not enough for gyrotropy is that the material is non centro-symmetric. There exist 21 inversion-asymmetric crystal classes, three of them are non-gyrotropic ( $T_d$ ,  $C_{3h}$  and  $D_{3h}$ ). Seven of the 18 gyrotropic crystal classes are non-enantiomorphic ( $C_s$ ,  $C_{2v}$ ,  $C_{3v}$ ,  $S_4$ ,  $D_{2d}$ ,  $C_{4v}$  and  $C_{6v}$ ),

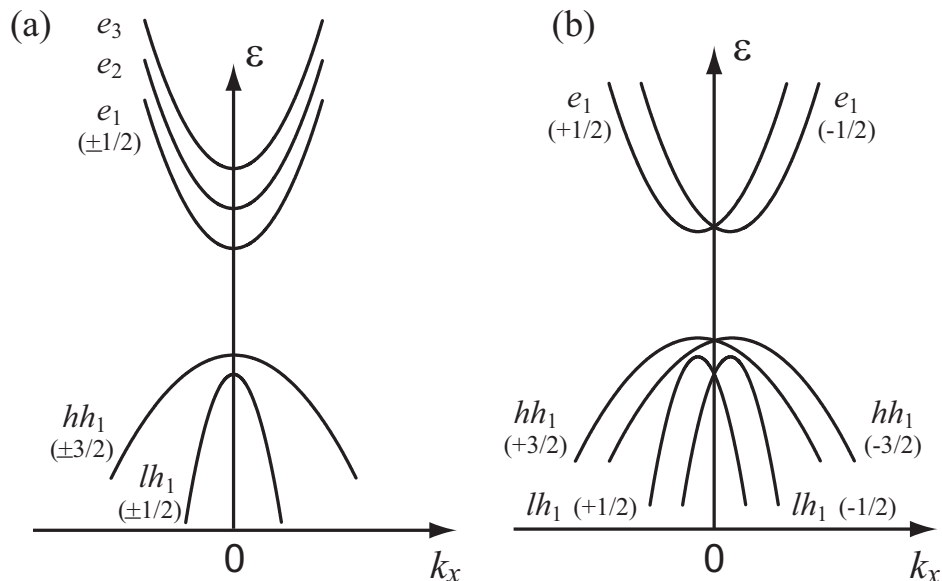


**Figure 2:** Band structure of a 2DEG close to the  $\Gamma$ -point ( $\mathbf{k} = 0$ ) including SOI, for (a) an inversion-symmetric semiconductor and (b) a non-centrosymmetric crystal. Both panels show the size quantized subbands, the split-off subbands are not drawn for clarity.

the other eleven are enantiomorphic (chiral) classes, which means that they have no reflection planes or rotation-reflection axes [26, 30, 31].

In gyrotropic media, as a consequence of the SOI, an additional spin-splitting emerges [25, 32–34]. Figure 2(b) illustrates the dispersion relation for gyrotropic media and shows that the spin degeneracy is lifted. This spin-splitting is described by spin dependent  $\mathbf{k}$ -linear terms  $H_{\text{SO}}$  in the Hamiltonian, which shift spin-up and spin-down subbands by  $-\Delta\mathbf{k}$  or  $+\Delta\mathbf{k}$  with respect to  $\mathbf{k} = 0$ . These terms  $H_{\text{SO}}$  cause, amongst other things, the in this work essential spin photocurrents, determine the spin relaxation [3, 35, 36] and permit the control of spin orientation by external fields [3, 8, 37–43]. The additional terms  $H_{\text{SO}}$  describing the spin splitting are given by:

$$H = \frac{\hbar k^2}{2m^*} + H_{\text{SO}} = \frac{\hbar k^2}{2m^*} + \sum_{lm} \beta_{lm} \sigma_l k_m. \quad (5)$$

Here, the first term characterizes the parabolic approximation of the conduction band,  $\beta$  is a material-specific second rank pseudo tensor,  $\sigma$  are the Pauli

spin matrices and  $l, m$  are coordinates. One can also write  $H_{\text{SO}}$  in the following form:

$$H_{\text{SO}} = \frac{\hbar}{2} \boldsymbol{\sigma} \cdot \boldsymbol{\Omega}(\mathbf{k}), \quad (6)$$

where  $\boldsymbol{\Omega}(\mathbf{k})$  is the effective Larmor frequency, which can be interpreted as  $\mathbf{k}$ -dependent effective magnetic field. For a certain  $\mathbf{k}$ , it yields a spin splitting of  $2\hbar|\boldsymbol{\Omega}(\mathbf{k})|$  between states with its spin parallel or perpendicular to  $\mathbf{k}$ .

The in Equation (5) arising  $\sigma_l k_m$  can be separated into a symmetric and an antisymmetric product, yielding:

$$H_{\text{SO}} = \sum_{lm} (\underbrace{\beta_{lm}^s \{\sigma_l, k_m\}}_{\text{Dresselhaus}} + \underbrace{\beta_{lm}^a [\sigma_l, k_m]}_{\text{Rashba}}) = H_{\text{SO}}^{\text{BIA}} + H_{\text{SO}}^{\text{SIA}}. \quad (7)$$

Here  $\beta^s$  and  $\beta^a$  are the corresponding symmetric and antisymmetric pseudo tensors. The symmetric term is called Dresselhaus term [11] and the other Rashba term [37, 44], their microscopic origins are the bulk [36, 45] and structure inversion asymmetry [37] (BIA and SIA), respectively. The interface inversion asymmetry (IIA) may cause additional  $\mathbf{k}$ -linear terms [46, 47], which can be neglected or assigned to BIA as both behave phenomenologically identical.

### 2.1.3 Origin of the $\mathbf{k}$ -linear and $\mathbf{k}$ -cubic terms

**2.1.3.1 BIA and SIA:** Since the Dresselhaus spin splitting is based on BIA and the optionally additionally appearing Rashba splitting is SIA-induced, these two types of inversion asymmetry will be considered here more closely. BIA results from the lack of inversion center that already exists in the bulk crystal of zinc-blende structure based materials. It can be influenced by e.g. the variation of the QW width, temperature or the charge carrier density. SIA represents an additional symmetry reduction introduced during the growth process of 2D structures or by external parameters, as e.g. an electric field or strain. This additional built-in asymmetry occurs for instance from nonequivalent normal and inverted interfaces, asymmetric doping or a special shape of the QW (see Fig. 3). SIA may also exist in QWs based on inversion-symmetric materials like Si and Ge. An external electric field along the growth direction tilts the band structure and therefore yields SIA. Thus, via the SIA term it

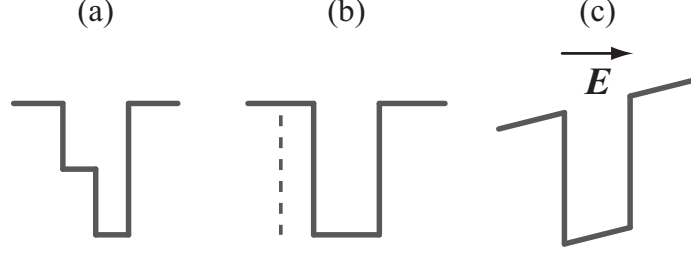


**Figure 3:** Different built-in asymmetries yielding SIA: (a) step shaped QW, (b) onesided, asymmetric doping and (c) tilted conduction band due to an electric field.

is possible to control the spin polarization by an externally applied electric field [37], which shows the importance of these spin-orbit coupling terms for spintronics.

BIA-induced zero magnetic field spin splitting already occurs in 3D materials without inversion center ( $T_d$  symmetry), here  $\mathbf{k}$ -linear terms are forbidden and solely  $\mathbf{k}$ -cubic terms appear in the conduction band Hamiltonian, which can be obtained by an expansion in a power series of  $\mathbf{k}$ :

$$H_{\text{SO},3\text{D}} = \gamma_c [\sigma_x k_x (k_y^2 - k_z^2) + \sigma_y k_y (k_z^2 - k_x^2) + \sigma_z k_z (k_x^2 - k_y^2)], \quad (8)$$

where  $\gamma_c$  is a material-specific constant,  $x \parallel [100]$  and  $y \parallel [010]$  [6, 48].

*2.1.3.2 BIA-induced  $\mathbf{k}$ -linear terms [49]:* Considering 2D structures based on zinc-blende crystals with symmetric interfaces, having  $D_{2d}$  symmetry, both  $\mathbf{k}$ -linear and -cubic terms in the Hamiltonian are allowed. The  $\mathbf{k}$ -linear terms for the lowest conduction subband  $e_1$  in (001)-grown QWs are regarded first. They can be obtained from the cubic term Eq. (8) describing the removal of spin degeneracy of the conduction-band states in a bulk semiconductor. To derive them, the quantum confinement effect has to be taken into account. Hereby, the transition from 3D to 2D is followed by the replacement of  $k_z$  and  $k_z^2$  by their average values  $\langle k_z \rangle = 0$  and  $\langle k_z^2 \rangle \neq 0$  ( $\langle k_z^2 \rangle \approx \pi^2/L_{\text{QW}}^2$ ), respectively, yielding:

$$H_{\text{SO},2\text{D}}^{\text{BIA},\text{lin}} = \gamma_c \langle k_z^2 \rangle (-\sigma_x k_x + \sigma_y k_y) = \beta (-\sigma_x k_x + \sigma_y k_y). \quad (9)$$

This term originates from BIA and is called Dresselhaus term, the coefficient  $\beta$  is commonly used to give its relative strength. Comparing Equation (9) with the before mentioned Eq. (6) containing the effective Larmor frequency  $\Omega_{\mathbf{k}}$  we obtain:

$$\begin{aligned}\Omega_{\mathbf{k},x}^{\text{lin}} &= -\frac{2\gamma_c}{\hbar} \langle k_z^2 \rangle k_x = -\frac{2\gamma_c}{\hbar} \langle k_z^2 \rangle k \cos\varphi, \\ \Omega_{\mathbf{k},y}^{\text{lin}} &= \frac{2\gamma_c}{\hbar} \langle k_z^2 \rangle k_y = \frac{2\gamma_c}{\hbar} \langle k_z^2 \rangle k \sin\varphi, \\ \Omega_{\mathbf{k},z}^{\text{lin}} &= 0,\end{aligned}\tag{10}$$

where  $k = \sqrt{k_x^2 + k_y^2}$  is composed of the components  $k_x = k \cos\varphi$  and  $k_y = k \sin\varphi$  and  $\varphi$  is defined as the angle between  $\mathbf{k}$  and the axis [100]. The corresponding spin splitting due to the  $\mathbf{k}$ -linear Dresselhaus term is angular independent and given by:

$$\Delta E^{\text{lin}} = \hbar \Omega_{\mathbf{k}}^{\text{lin}} k = 2\gamma_c \langle k_z^2 \rangle k.\tag{11}$$

Figure 4 shows the corresponding electron dispersion (a) and the contours of constant energy (b) in the  $k_x$ - $k_y$  plane [33]. Thereby (a) results from the revolution of two parabolas, being symmetrically displaced with respect to

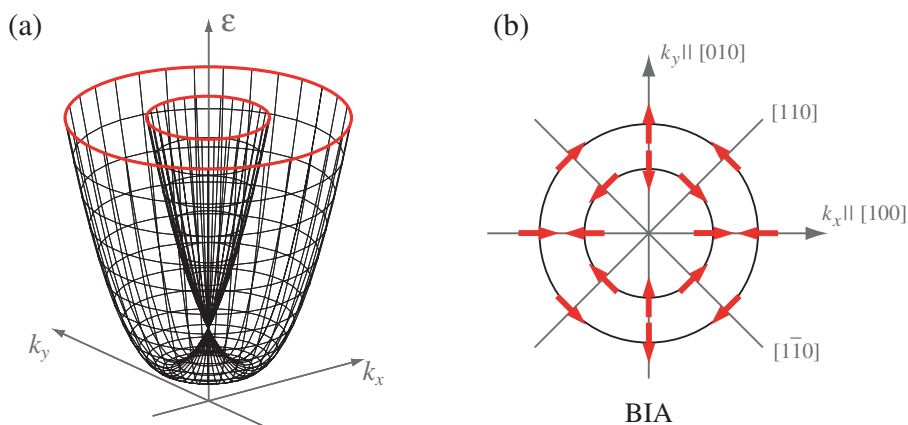


**Figure 4:** (a) Schematic conduction band structure of a 2DEG due to BIA-induced  $\mathbf{k}$ -linear terms. The energy  $\varepsilon$  is plotted as a function of  $k_x$  and  $k_y$ . (b) Contours of constant energy with corresponding spin orientation.

$\mathbf{k} = 0$ , around the energy axis. And (b) illustrates the orientation of the spins, which are always aligned along the cubic axes and perpendicularly to the crystallographic axes, forming an antivortex.

*2.1.3.3 BIA-induced  $\mathbf{k}$ -cubic terms and their separation into first- and third-order harmonics [49]:* Now the remaining  $\mathbf{k}$ -cubic terms are considered, they are given by:

$$H_{\text{SO},2\text{D}}^{\text{BIA,cub}} = \gamma_c(\sigma_x k_x k_y^2 - \sigma_y k_y k_x^2). \quad (12)$$

Utilizing the trigonometric formulas  $\sin^2\varphi = (1 - \cos 2\varphi)/2$  and  $2\cos\varphi \cos 2\varphi = (\cos\varphi + \cos 3\varphi)$ , the  $\mathbf{k}$ -cubic  $x$ -component of  $\Omega_{\mathbf{k}}$  can be expressed as:

$$\begin{aligned} k_x k_y^2 &= k^3 \cos\varphi \sin^2\varphi = k^3 \cos\varphi \frac{1 - \cos 2\varphi}{2} = \\ &= \frac{k^3}{2} \cos\varphi - \frac{k^3}{4} 2\cos\varphi \cos 2\varphi = \frac{k^3}{4} \cos\varphi - \frac{k^3}{4} \cos 3\varphi. \end{aligned} \quad (13)$$

Analogously the  $\mathbf{k}$ -cubic  $y$ -component of  $\Omega_{\mathbf{k}}$  can be derived applying  $\cos^2\varphi = (1 + \cos 2\varphi)/2$  and  $2\sin\varphi \cos 2\varphi = (\sin 3\varphi - \sin\varphi)$ :

$$\begin{aligned} -k_x^2 k_y &= -k^3 \cos^2\varphi \sin\varphi = -k^3 \sin\varphi \frac{1 + \cos 2\varphi}{2} = \\ &= -\frac{k^3}{2} \sin\varphi - \frac{k^3}{4} 2\sin\varphi \cos 2\varphi = -\frac{k^3}{4} \sin\varphi - \frac{k^3}{4} \sin 3\varphi. \end{aligned} \quad (14)$$

Accordingly the complete  $\mathbf{k}$ -cubic Dresselhaus contribution to  $\Omega_{\mathbf{k}}$  arises as:

$$\begin{aligned} \Omega_{\mathbf{k},x}^{\text{cub}} &= -\Omega_1^{\text{cub}} \cos\varphi - \Omega_3 \cos 3\varphi, \\ \Omega_{\mathbf{k},y}^{\text{cub}} &= \Omega_1^{\text{cub}} \sin\varphi - \Omega_3 \sin 3\varphi, \\ \Omega_{\mathbf{k},z}^{\text{cub}} &= 0, \end{aligned} \quad (15)$$

with:

$$\Omega_1^{\text{cub}} = -\frac{\gamma_c}{2\hbar} k^3 \quad \text{and} \quad \Omega_3 = \frac{\gamma_c}{2\hbar} k^3. \quad (16)$$

The corresponding spin splitting due to the bulk inversion asymmetry induced  $\mathbf{k}$ -cubic terms is given by:

$$\begin{aligned}\Delta E^{\text{cub}} &= \hbar \Omega_{\mathbf{k}}^{\text{cub}} = \frac{\gamma_c k^3}{2} \sqrt{(\cos\varphi - \cos 3\varphi)^2 + (\sin\varphi + \sin 3\varphi)^2} = \\ &= \frac{\gamma_c k^3}{2} \sqrt{2 - 2(\cos\varphi \cos 3\varphi - \sin\varphi \sin 3\varphi)} = \\ &= \frac{\gamma_c k^3}{2} \sqrt{2 - 2\cos 4\varphi} = \gamma_c k^3 |\sin 2\varphi|. \end{aligned} \quad (17)$$

Equation (17) reveals the anisotropy in  $\mathbf{k}$ -space of the  $\mathbf{k}$ -cubic contributions to the Hamiltonian  $H_{\text{BIA}}$ . This anisotropy is described by the  $\varphi$ -dependence of the  $\mathbf{k}$ -cubic contributions to the Hamiltonian (see Eqs. (15)). These  $\varphi$ -dependences are given by the linear combinations of the first- and third-order harmonics, i.e., as combinations of  $\cos\varphi$ ,  $\sin\varphi$  and  $\cos 3\varphi$ ,  $\sin 3\varphi$  terms. Figure 5 depicts the angular behavior of the anisotropic spin splitting due to the  $\mathbf{k}$ -cubic Dresselhaus terms, this plot was obtained experimentally in an earlier work of B. Jusserand [50].

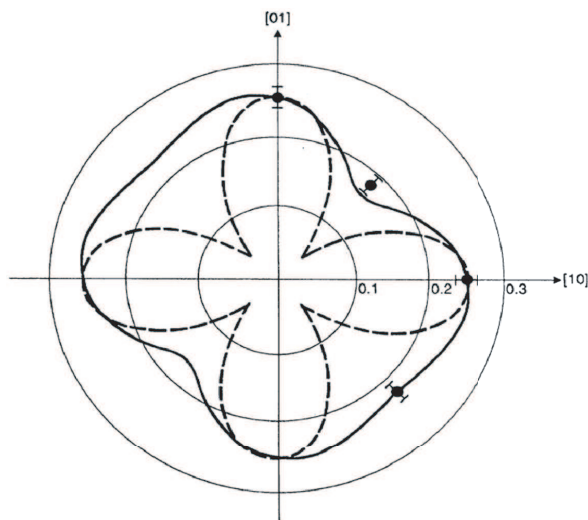


**Figure 5:** Angular variation of the spin splitting due to the BIA-induced electric field only (dashed line) and the total electric field of BIA and SIA (solid line) after Ref. [50]. The dots give the experimental values obtained by Raman-scattering experiments.

In literature, it is commonly used to combine the first-order harmonics of the  $\mathbf{k}$ -linear and  $\mathbf{k}$ -cubic Dresselhaus terms. This leads to a renormalization of the  $\mathbf{k}$ -linear Dresselhaus contribution. The resulting spin-dependent part of the energy dispersion consists of both linear and cubic contributions and has the form:

$$\begin{aligned}\Omega_{\mathbf{k},x} &= -\Omega_1 \cos\varphi - \Omega_3 \cos 3\varphi, \\ \Omega_{\mathbf{k},y} &= \Omega_1 \sin\varphi - \Omega_3 \sin 3\varphi, \\ \Omega_{\mathbf{k},z} &= 0,\end{aligned}\tag{18}$$

with:

$$\Omega_1 = \frac{2\gamma_c}{\hbar} k \left( \langle k_z^2 \rangle - \frac{1}{4} k^2 \right) \quad \text{and} \quad \Omega_3 = \frac{\gamma_c}{2\hbar} k^3.\tag{19}$$

According to these equations, the  $\mathbf{k}$ -cubic spin splitting may be neglected for low electron energies ( $k^2$  is actually  $k_F^2$ , where  $k_F$  gives the Fermi-wavevector). Whereas at higher wavevectors corresponding to high temperatures or large electron concentrations, the  $\mathbf{k}$ -cubic term should be considered as well.

The in this work carried out photocurrent measurements are sensitive to the first-order harmonics ( $\propto \sin\varphi$  and  $\cos\varphi$ ) in the Fourier expansion of the non-equilibrium electron distribution function only, but not to third-order harmonics. Hence, the photocurrent measurements reflect only the renormalized Dresselhaus constant given by  $\Omega_1$  in the Equations (18). Other phenomena, such as the spin relaxation, spin-flip Raman scattering or the weak anti-localization are in contrast sensitive to both, first- and third-order harmonics of  $\mathbf{\Omega}$ . This leads to a corresponding anisotropy in these effects (compare e.g. Fig. 5 of Ref. [50]).

*2.1.3.4 SIA-induced  $\mathbf{k}$ -linear terms [49]:* The SIA-induced  $\mathbf{k}$ -linear terms in the Hamiltonian are called Rashba terms (sometimes Bychkov-Rashba terms), they appear due to the additional symmetry restrictions in asymmetric 2D structures. (001)-grown asymmetric QWs belong to the  $C_{2v}$  symmetry class,

here the SIA related Hamiltonian has the following form, where the coefficient  $\alpha$  indicates the relative strength of the Rashba spin splitting:

$$H_{\text{SO}}^{\text{SIA}} = \alpha(\sigma_x k_y - \sigma_y k_x). \quad (20)$$

Equation (20) shows that the form of this term is independent of the choice of the Cartesian coordinates in the QW plane. The distribution of the spin orientation in the  $\mathbf{k}$ -space can be visualized by the introduction of an effective magnetic field. The from  $H_{\text{SO}}^{\text{SIA}}$  resulting spin splitting is illustrated in Figure 6(d), it forms a vortex, where the spins are always oriented perpendicularly to the corresponding wavevector  $\mathbf{k}$ . This is a consequence of the vector product in the Rashba spin-orbit interaction.

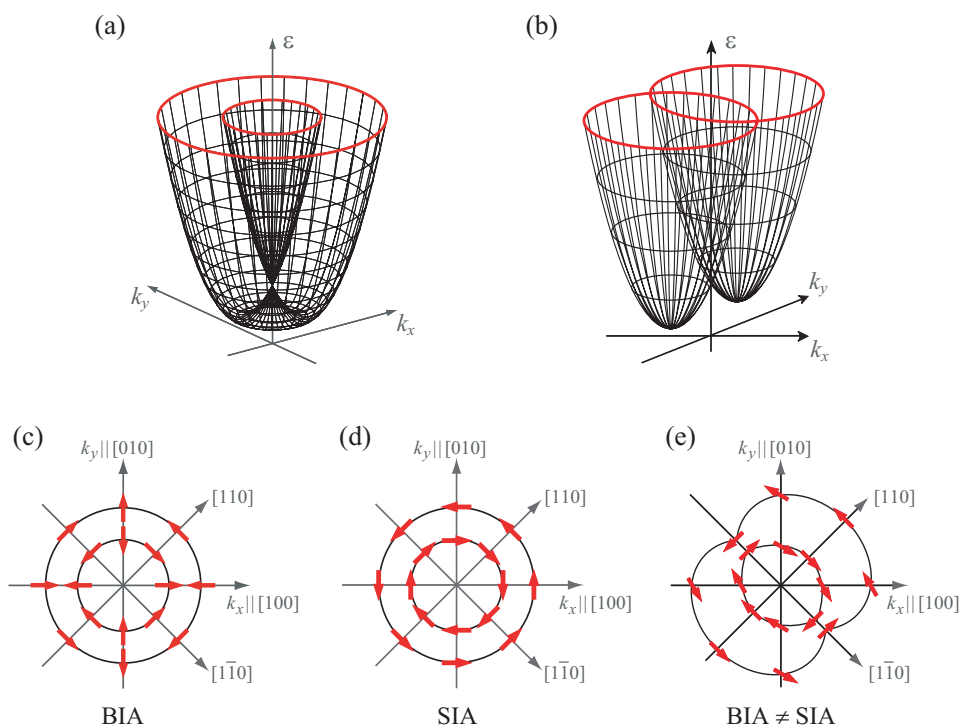


**Figure 6:** Schematic 2D band structure for  $\mathbf{k}$ -linear terms in a structure with  $C_{2v}$  symmetry. The energy  $\varepsilon$  is plotted as a function of  $k_x$  and  $k_y$  in (a) with only one type of inversion asymmetry (BIA or SIA) and in (b) for both BIA- and SIA-induced  $\mathbf{k}$ -linear terms. The bottom panel shows the distribution of spin orientations for the 2D Fermi energy for different strengths of BIA and SIA terms.

Figure 6 gives an overview of different band structures resulting *just* from  $\mathbf{k}$ -linear terms. The upper panel shows the band structure with (a) only one type of inversion asymmetry and with (b) both types at equal strength. In the illustration positive coefficients  $\alpha, \beta \geq 0$  are assumed. If the strengths of BIA and SIA are the same, then the 2D band structure consists of two revolution paraboloids with revolution axes symmetrically shifted in opposite directions with respect to  $\mathbf{k} = 0$  (see Fig. 6(b)). Figure 6(e) shows the most common case, where BIA and SIA exist but have different strengths.

## 2.2 THz radiation induced photocurrents

In this work spin photocurrents were mainly used as a workhorse to investigate the inversion asymmetry in the different QW structures. Hereby, three diverse in gyrotropic media occurring effects were applied: First, the magneto-gyrotropic photogalvanic effect (MPGE), an effect that yields a spin polarized current due to the conversion of the zero-bias spin separation [51] induced spin current into an electric current via an external magnetic field. Second, the spin-galvanic effect (SGE), where the asymmetric relaxation of a nonequilibrium spin polarization  $\mathbf{S}$ , which lies in the QW plane owing to an external magnetic field, results in an electric current. And third, the circular photogalvanic effect (CPGE), here a photocurrent originates without magnetic field just on account of the asymmetric excitation of charge carriers in  $\mathbf{k}$ -space via circular polarized light having the propagation direction  $\hat{\mathbf{e}}$ .

To analyze the  $\mathbf{k}$ -linear spin splitting with the help of these photogalvanic effects, an approach based on the equivalence of the different second rank pseudo tensors  $\boldsymbol{\beta}$ ,  $\boldsymbol{\gamma}$ ,  $\mathbf{Q}$  and  $\boldsymbol{\mu}$  was used:

$$\begin{aligned}
 H_{\text{SO}} &= \sum_{lm} \beta_{lm} \sigma_l k_m && \mathbf{k}\text{-linear terms in the Hamiltonian} && (21) \\
 j_l &= \sum_m Q_{lm} S_m && \text{SGE} \\
 j_l &= \sum_m \mu_{lm} P_{\text{circ}} \hat{e}_m E^2 && \text{CPGE}
 \end{aligned}$$

Since, the irreducible components of the second rank pseudo tensors, mentioned in the Eqs. (21), differ by a scalar factor only (and  $\boldsymbol{\beta}$  is inverse to the others), it

is possible to gain knowledge about the anisotropy in spin-splitting by mapping the magnitude of the photocurrents [52, 53]. In Chapter 4 it will be shown that the spin-splitting can also be investigated with the MPGE induced by unpolarized radiation.

Thereby, these photocurrents are just linked to the first-order harmonics ( $\propto \sin \varphi$  and  $\cos \varphi$ ). Thus, they are insensitive to the third harmonics in the Dresselhaus Hamiltonian ( $\propto \sin 3\varphi$  and  $\cos 3\varphi$ ) and reflect only the renormalized constant given by  $\Omega_1$  in Eq. (19).

In the following, these three photogalvanic effects with their phenomenological equations and microscopic models will be explained in detail [32].

### 2.2.1 Magneto-gyrotropic photogalvanic effect

The MPGE [12, 26, 32, 49, 51, 54, 55] arises under the excitation with polarized and even unpolarized THz radiation. By an appropriate experimental setup, the resulting current can be separated, to yield information about the strength of Rashba and Dresselhaus SOI in different materials, which was demonstrated during this work and already earlier [7, 12, 56, 57]. First the MPGE's fundamental theory will be considered closer.

*2.2.1.1 Phenomenological theory of the MPGE:* The phenomenological theory determines the complete experimental setup as e.g. the direction of the current with respect to the magnetic field or the crystallographic axes. It also describes the photocurrent's dependence on the radiation's polarization state. In the phenomenology, the knowledge of microscopic details is not necessary.

The phenomenological equation describing the MPGE [58] under normal irradiation within a linear approximation in the magnetic field strength  $\mathbf{B}$  is given by:

$$j_\alpha = \sum_{\beta\gamma\delta} \phi_{\alpha\beta\gamma\delta} B_\beta I \frac{(e_\gamma e_\delta^* + e_\delta e_\gamma^*)}{2} + \sum_{\beta\gamma} \xi_{\alpha\beta\gamma} B_\beta \hat{e}_\gamma I P_{\text{circ}}. \quad (22)$$

Here the fourth rank pseudo-tensor  $\phi$  is symmetric in the last two indices,  $\mathbf{e} = \mathbf{E}/|\mathbf{E}|$  gives the (complex) unit vector of the light polarization,  $\mathbf{E}$  is the

radiation's electric field,  $\hat{e}$  the unit vector pointing in the light propagation direction,  $I$  gives the radiation's intensity and  $P_{\text{circ}}$  the radiation's helicity. The first term on the right side of Eq. (22) describes the photocurrent due to unpolarized and linearly polarized radiation, i.e. the linear MPGE. The second term containing the third rank tensor  $\boldsymbol{\xi}$  is the helicity dependent contribution to the photocurrent, it occurs just for elliptically polarized light and in particular for circularly polarized light. Characteristic for the circular MPGE is its sign inversion upon switching the radiation's helicity.

In this work, mainly asymmetrically and few symmetrically doped (001)-grown QWs belonging to  $C_{2v}$  and  $D_{2d}$  symmetry, respectively, were investigated. For both, the phenomenological equations look similarly and differ only in the relations between the parameters  $S_1^\pm$  to  $S_4^\pm$ , which stem from the non-vanishing components of the tensors  $\boldsymbol{\phi}$  and  $\boldsymbol{\xi}$ . For  $C_{2v}$  symmetry and in the cubic coordinate system  $x \parallel [100]$ ,  $y \parallel [010]$  Eq. (22) reduces to [58]:

$$j_x = S_1^+ B_x I + S_1^- B_y I - (S_2^+ B_x + S_2^- B_y) (e_x e_y^* + e_y e_x^*) I \\ + (S_3^+ B_x - S_3^- B_y) (|e_x|^2 - |e_y|^2) I + (S_4^+ B_x - S_4^- B_y) I P_{\text{circ}}, \quad (23)$$

$$j_y = -S_1^- B_x I - S_1^+ B_y I + (S_2^- B_x + S_2^+ B_y) (e_x e_y^* + e_y e_x^*) I \\ + (-S_3^- B_x + S_3^+ B_y) (|e_x|^2 - |e_y|^2) I + (-S_4^- B_x + S_4^+ B_y) I P_{\text{circ}}. \quad (24)$$

The first terms of the Eqs. (23) and (24) proportional to the coefficients  $S_1^\pm$  are polarization independent and even occur under irradiation with unpolarized light. The other terms show the typical polarization dependencies that can be described by the Stokes parameters. The last fractions proportional to the coefficients  $S_4^\pm$  emerge only under illumination with circularly (or elliptically) polarized radiation. Due to these individual characteristics and the orientation of the magnetic field, the parameters  $S_1^\pm$  to  $S_4^\pm$  can be separated experimentally.

*2.2.1.2 Microscopic model of the MPGE:* The MPGE is described by a microscopic model that is based on a spin-dependent asymmetry in the electron scattering. This asymmetry leads under Drude absorption to the zero-bias spin separation [51, 54, 56]. In gyrotropic media, as the here investigated QW

structures, the spin-orbit interaction leads to an additional term in the scattering matrix element, being linear in both the wave vector  $\mathbf{k}$  and the Pauli spin matrices  $\boldsymbol{\sigma}$ :

$$\hat{V}_{\text{el-phonon}}(\mathbf{k}', \mathbf{k}) = \Theta_c \sum_j \varepsilon_{jj} + \Theta_{cv} \xi \sum_j [(\mathbf{k}' + \mathbf{k}) \times \boldsymbol{\sigma}]_j \varepsilon_{j+1 j+2}, \quad (25)$$

$$\xi = \frac{i\hbar V_{cv}}{3m_0^*} \frac{\Delta_{\text{so}}}{E_g(E_g + \Delta_{\text{so}})}.$$

In Eq. (25) the scattering matrix element of the electron-phonon interaction  $\hat{V}_{\text{el-phonon}}(\mathbf{k}', \mathbf{k})$  is given. Here  $\Theta_c$  and  $\Theta_{cv}$  are the intraband and interband constants and  $\varepsilon_{jj'}$  gives the phonon-induced strain tensor, which depends on the phonon wavevector  $\mathbf{q} = \mathbf{k}' - \mathbf{k}$ . The term  $\xi$  takes for zinc-blende based QWs the in Eq. (25) given form, it contains the free electron effective mass  $m_0^*$ , the bandgap  $E_g$ , the spin-orbit-splitting of the bulk-semiconductors valence band  $\Delta_{\text{so}}$  and the interband matrix element  $V_{cv} = \langle S | \hat{p}_z | Z \rangle$  of the momentum operator. The microscopic origin of the additional term in the scattering ma-

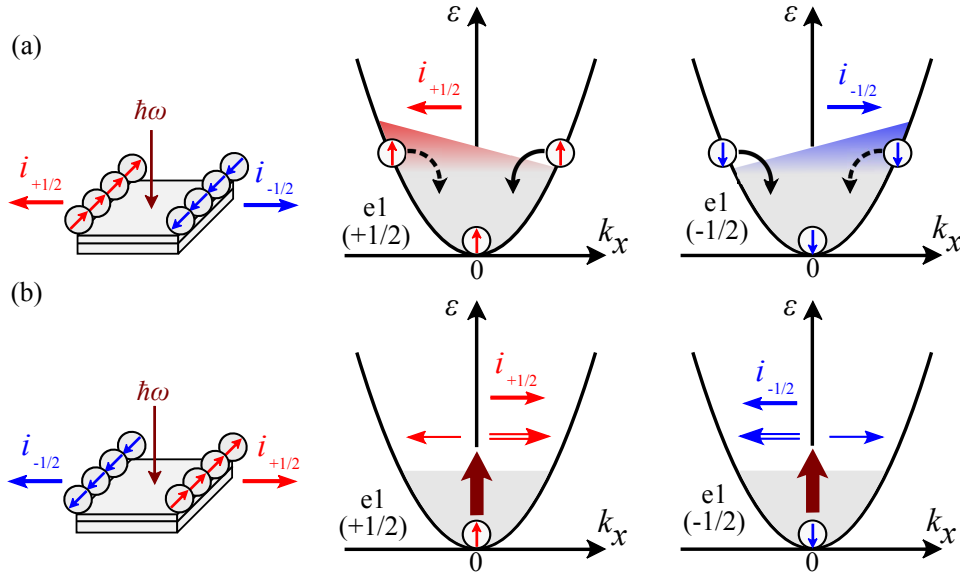


**Figure 7:** Asymmetry in (a) the relaxation process of a homogeneous heated electron gas and (b) the excitation via Drude absorption. The tilted shadowed areas indicate schematically the non-equilibrium distribution of states with positive and negative  $\mathbf{k}$ .

trix element is BIA and SIA, hence in the scattering both contributions are reflected.

In contrast to non-gyrotropic media, where the absorption of radiation or the relaxation of a heated electron gas leads to a symmetric distribution of electrons in the  $\mathbf{k}$ -space, in gyrotropic media the asymmetric scattering results in different scattering rates for transitions appearing via positive or negative phonon wavevectors  $\mathbf{q}$  [51]. For example in the excitation of carriers due to Drude-like absorption, the asymmetric scattering on phonons results in spin currents of equal strength propagating in opposite directions for spin-up and spin-down subbands (see Fig. 7(b)). These spin currents cancel each other and do not yield any net electric current.

If an external in-plane magnetic field is applied, the Zeeman effect separates spin-up and spin-down subbands in energy, which leads to an imbalance in the two spin currents. As a result the pure spin current is converted into a measurable spin polarized electric current, which depends on the magnetic field strength and the  $g$  factor. This mechanism is illustrated for the relaxation process in Fig. 8. The hereby evoked photocurrent is independent from the radiation's polarization state. In the excitation process also asymmetric scattering occurs (see Fig. 7(a)), which leads, similarly to the relaxation, to

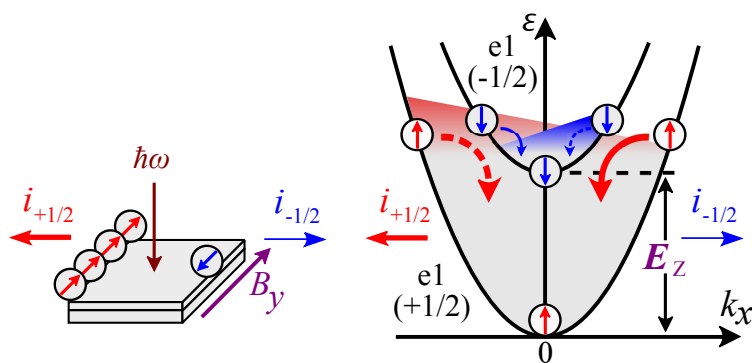


**Figure 8:** Asymmetry in the relaxation process of a homogeneous heated electron gas in the Zeeman splitted subbands. The tilted shaded areas indicate schematically the non-equilibrium distribution of states with positive and negative  $\mathbf{k}$ .

a photocurrent. However, a current, resulting from asymmetric excitation, possesses a characteristic polarization dependence.

The above explained microscopic model is based on the electron's spin. The question, if there is also a possible spin independent contribution in the current formation will be considered closer in the first part of the experimental results.

### 2.2.2 Spin-galvanic effect

The SGE is a current that occurs due to an imbalance in the spin polarization in low dimensional semiconductor structures [26,32,33,49,59]. Hereby, it is not important how the nonequilibrium spin polarization was reached. In our case the SGE emerges under normal incidence of circularly polarized THz radiation, and can also be used to gain information about the Rashba/Dresselhaus spin splitting. In the following the underlying phenomenological equations and the microscopic model will be explained.

*2.2.2.1 Phenomenological theory of the SGE:* In gyrotropic media, where  $\mathbf{k}$ -linear terms in the Hamiltonian are allowed, a uniform nonequilibrium spin polarization  $\mathbf{S}$  in the QW plane results due to asymmetric spin-flip scattering in an electric current  $\mathbf{j}$ :

$$j_i = \sum_m Q_{im} S_m. \quad (26)$$

Considering (001)-grown QWs belonging to the  $C_{2v}$  symmetry class and the cubic coordinate system  $x \parallel [100]$ ,  $y \parallel [010]$  Eq. (26) reduces to:

$$\mathbf{j}_{\text{SGE}} = b \begin{pmatrix} \beta & -\alpha \\ \alpha & -\beta \end{pmatrix} \mathbf{S}. \quad (27)$$

The constant  $b$  depends on the microscopic details of the SGE. Eq. (27) also shows that the current can be separated into BIA and SIA induced components.

*2.2.2.2 Microscopic model of the SGE:* Figure 9 illustrates the microscopic model of the SGE. It depicts the electron energy spectrum along  $k_x$  in a gyrotropic media. The unbalanced population in both spin subbands (see Fig. 9(a))

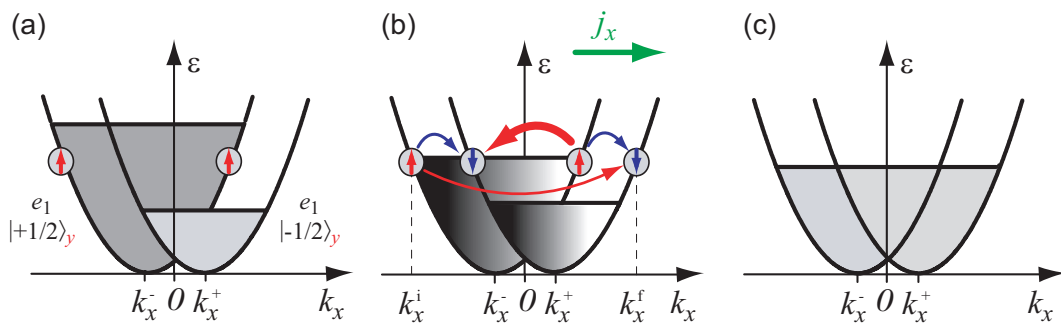


**Figure 9:** Microscopic model of the SGE. (a) Nonequilibrium spin polarization in the  $y$  direction. (b) Relaxation from an initial state  $k_x^i$  to a final state  $k_x^f$  occurs via asymmetric scattering. Different probability, given by the thickness of the bent arrows, results in an electric current. (c) Equilibrium occupation after the relaxation.

is a consequence of the spin orientation in the  $y$  direction. The photocurrent arises from  $\mathbf{k}$ -dependent spin-flip relaxation processes (see Fig. 9(b)): Spins from the higher filled, e.g. spin-up subband  $|+1/2\rangle_y$  are scattered along  $k_x$  to the less filled spin-down subband  $|-1/2\rangle_y$ . At this, four different transitions exist, whose scattering probability, given by the strength of the bent arrows, depends on  $\Delta k_x = k_x^f - k_x^i$  [60]. The two scattering processes indicated with blue arrows have the same probability, thus they preserve the symmetric carrier distribution in the subbands and do not contribute to a current flow. In contrast, the transitions indicated with red arrows are inequivalent and generate an asymmetric carrier distribution around the subband minima in both subbands. This asymmetric population yields a current flow  $j_x$  along the  $x$  direction, which decays with the spin relaxation time  $\tau_s$ . In the case of a higher filled spin-down subband, an inversion of the current flow direction would result. Additionally, it should be mentioned that the Elliott-Yafet mechanism determines the SGE current (spin-flip scattering), even if other spin relaxation mechanisms dominate. However, the SGE current decays with the spin relaxation time  $\tau_s$ , which is determined by the D'yakonov-Perel' mechanism in GaAs QWs [61].

*2.2.2.3 Spin orientation in the SGE:* In our experiments, we used a method based on optical orientation in the presence of a magnetic field, to reach the required spin polarization in the QW plane. This method generates a uniform distribution within each spin subband and, moreover, excludes the circular photogalvanic effect (see next paragraph) for  $C_{2v}$  symmetry. The absorption of circularly polarized radiation at normal incidence results in a steady-state spin polarization  $S_{0z}$  along the  $z$ -axis. Due to the in-plane magnetic field  $B_x$ ,  $S_{0z}$  is subjected to the Larmor precession and rotated into the 2DEG-plane (see Fig. 10). The resulting nonequilibrium spin polarization  $S_y$  is given by:

$$S_y = -\frac{\omega_L \tau_{s\perp}}{1 + (\omega_L \tau_s)^2} S_{0z}, \quad (28)$$

where  $\tau_s = \sqrt{\tau_{s\parallel} \tau_{s\perp}}$  is the spin relaxation time,  $\tau_{s\parallel}$  and  $\tau_{s\perp}$  are its longitudinal and transverse components and  $\omega_L$  is the Larmor frequency:

$$\omega_L = \frac{g\mu_B B_x}{\hbar}. \quad (29)$$

Here,  $g$  is the effective  $g$  factor in the QW plane and  $\mu_B$  is the Bohr magneton. The denominator of Eq. (28) gives the decay of  $S_y$ , if  $\omega_L$  exceeds the inverse spin relaxation time, and is well known from the Hanle effect [62]. For low magnetic field strengths  $\omega_L \tau_s < 1$  holds and the photocurrent depends linearly on  $B$ . For stronger  $\mathbf{B}$ -fields the current reaches a maximum and then drops, due to the Hanle effect. At the peak position of the current  $\omega_L \tau_s = 1$ , which allows to estimate  $\tau_s$ .

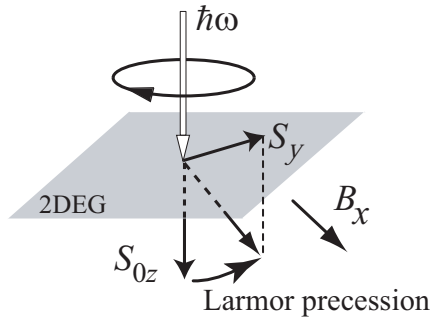


**Figure 10:** Circularly polarized radiation yields a spin polarization  $S_{0z}$  along the growth direction. Subsequently, the magnetic field  $B_x$  rotates  $\mathbf{S}$ , due to the Larmor precession, into the QW plane.

### 2.2.3 Circular photogalvanic effect

The third photogalvanic effect that is used to deduce the Rashba/Dresselhaus ratio, is the CPGE [26, 32, 33, 49, 63]. It is caused by a transfer of the angular momentum of a circularly polarized photon to an electron in a gyrotropic media, which results in an electric current. In  $C_{2v}$  symmetry the CPGE requires oblique incidence of radiation. This effect does not need a magnetic field, therefore, it is insensitive to e.g. the  $g$  factor. In the following, the phenomenological equations and the microscopic model will be considered.

*2.2.3.1 Phenomenological theory of the CPGE:* Typically for the CPGE is that the current reverses its direction upon switching the radiation's helicity from right- ( $\sigma^+$ ) to left-handed ( $\sigma^-$ ) circular polarization. This photocurrent is given by:

$$\mathbf{j}_l = \sum_m \mu_{lm} \mathbf{i} (\mathbf{E} \times \mathbf{E}^*)_m = \sum_m \mu_{lm} \hat{\mathbf{e}}_m P_{\text{circ}} E^2. \quad (30)$$

In Eq. (30) the current's sign inversion is obvious, as  $P_{\text{circ}}$  is +1 for  $\sigma^+$  light and -1 for  $\sigma^-$  radiation.

For (001)-grown QWs belonging to the  $C_{2v}$  symmetry class and using the coordinate system  $x \parallel [100]$ ,  $y \parallel [010]$  Eq. (30) can be written as [52]:

$$\mathbf{j}_{\text{CPGE}} = c \begin{pmatrix} \beta & -\alpha \\ \alpha & -\beta \end{pmatrix} \hat{\mathbf{e}} P_{\text{circ}} E^2. \quad (31)$$

The CPGE constant  $c$  is determined by the optical selection rules and by the momentum relaxation time. Eq. (31) also illustrates the current's separation into BIA and SIA induced components.

*2.2.3.2 Microscopic model of the CPGE:* A basic requirement for the occurrence of the CPGE is the spin splitting in gyrotropic materials [63]. In (001)-grown QWs belonging to the  $C_{2v}$  point group the CPGE current due to inter-subband transitions in the presence of inhomogeneous broadening can be estimated as [32]:

$$j_x = -\tilde{\Lambda} \frac{e}{\hbar} (\beta_{yx}^{(2)} - \beta_{yx}^{(1)}) \left[ \tau_p^{(2)} \eta_{\perp}(\hbar\omega) + (\tau_p^{(1)} - \tau_p^{(2)}) \bar{\varepsilon} \frac{d\eta_{\perp}(\hbar\omega)}{d\hbar\omega} \right] \frac{IP_{\text{circ}}}{\hbar\omega} \hat{\mathbf{e}}_y. \quad (32)$$

Here  $\beta_{yx}^{(1,2)}$  are different coefficients and  $\tau_p^{(1,2)}$  different momentum relaxation times for the subbands  $e1$  and  $e2$ ,  $\eta_{\perp}$  gives the absorbance for the polarization perpendicular to the QW plane and  $\bar{\varepsilon}$  denotes the mean value of the electron energy. The parameter  $\tilde{\Lambda}$  determines the absorbance for the light polarized in the interface plane, originates from  $\mathbf{k} \cdot \mathbf{p}$  admixture of valence band states to the electron wave function and is given by:

$$\tilde{\Lambda} = \frac{\varepsilon_{21}\Delta_{\text{so}}(2\varepsilon_g + \Delta_{\text{so}})}{2\varepsilon_g(\varepsilon_g + \Delta_{\text{so}})(3\varepsilon_g + 2\Delta_{\text{so}})}. \quad (33)$$

The current  $j_y$  results from interchanging the indices  $x$  and  $y$  in Eq. (32).

Figure 11(a) illustrates the microscopic model for the CPGE in  $C_{2v}$  symmetry systems at oblique incidence for  $\sigma^+$  radiation. The resulting current is caused by direct inter-subband transitions, which are spin-conserving due to selection rules [49, 65]. The rates of these transitions, indicated by the strength of

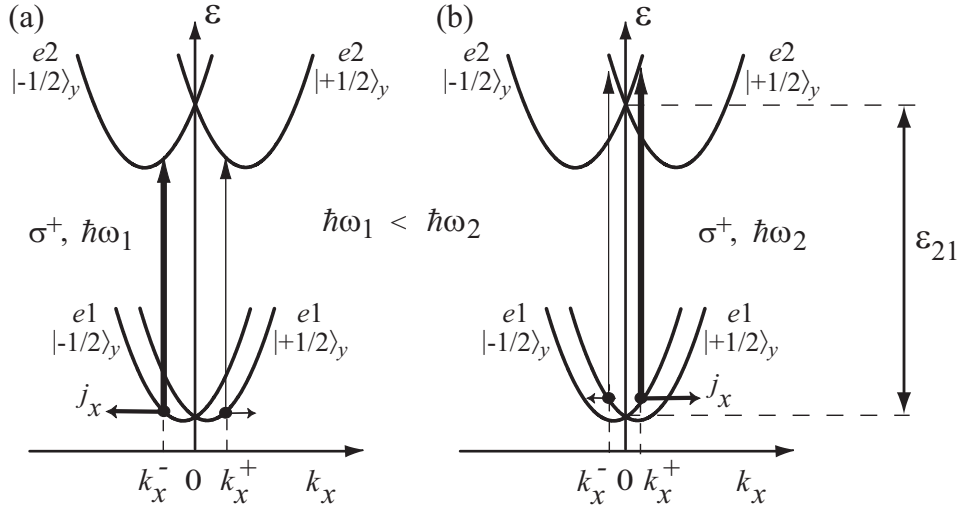


**Figure 11:** Microscopic model of the CPGE in  $C_{2v}$  point symmetry, describing its spectral sign inversion [64]. (a) Excitation at oblique incidence with  $\sigma^+$  radiation of  $\hbar\omega$  less than the energy of subband separation  $\varepsilon_{21}$  induces direct spin-conserving transitions (vertical arrows). The different rates of these transitions are indicated by the thickness of the arrows. A photocurrent results due to the asymmetrical distribution of carriers in  $\mathbf{k}$ -space. (b) Model for an increased photon energy: The position of the transitions is shifted, yielding a sign change in current.

the vertical arrows, differ for electrons, whose spin is oriented parallel ( $\mathbf{k} < 0$ ) or antiparallel ( $\mathbf{k} > 0$ ) to  $y$ . Therefore, an asymmetric distribution of photoexcited electrons results, if the splittings of the subbands  $e1$  and  $e2$  are not equal. This means, an electrical current follows from the spin-conserving but spin-dependent transitions (see Eq. (32)). If the angle of incidence is reversed, the transition rates (thickness of the arrows) are mirrored and thus, the current changes its direction. Figure 11(b) shows that an increased photon energy also leads to an inversion of the current direction. Since the CPGE is caused by spin-dependent spin-conserving optical transitions, it is proportional to the strength of subband spin splitting. Under absorption of  $\sigma^-$  light the microscopic model yields analogously an inversion of the current direction, compared to the case of  $\sigma^+$  radiation.

### 2.3 Spin relaxation mechanisms

In spintronics long spin lifetimes are of particular interest, therefore many efforts are ventured to suppress the spin relaxation in suitable materials, as e.g. by eliminating the D'yakonov-Perel' mechanism. Furthermore, spin re-

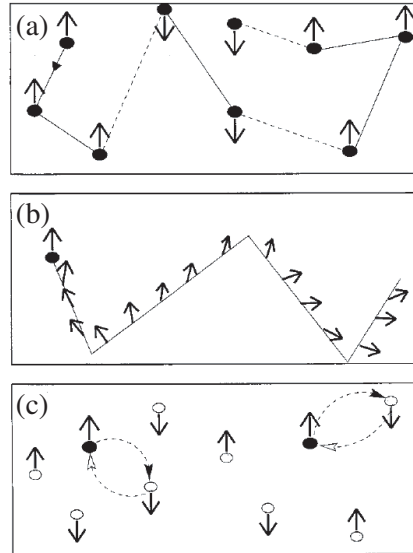


**Figure 12:** (a) Elliott-Yafet mechanism. (b) D'yakonov-Perel' mechanism. (c) Bir-Aronov-Pikus mechanism.

laxation is essential in the time-resolved Kerr rotation experiments and the analysis of their results. Hence, in the following a brief overview of spin relaxation is given, and the most important mechanisms for (001)-grown zinc-blende structure based QWs are explained [6, 66].

Figure 12 illustrates the three main mechanisms contributing to the spin relaxation of conduction electrons after Ref. [67]: The Bir-Aronov-Pikus mechanism [68] describes the spin relaxation due to scattering by holes. Here the spin-flip occurs as a result of the electron-hole exchange interaction. This mechanism is important in  $p$ -doped samples and therefore not explained here (in this work only  $n$ -type structures are investigated). Another possibility is the D'yakonov-Perel' mechanism [69], where the spin precesses about the effective magnetic field between two collisions. It will be mainly discussed in this section, since in most of the investigated samples this is the dominating relaxation mechanism. Furthermore, this mechanism can be easily suppressed by appropriate strengths of BIA and SIA, as explained in the next Chapter. Additionally, the Elliott-Yafet mechanism [70, 71] will be explained. In this case, the electron loses its spin orientation during a collision with an impurity.

### 2.3.1 D'yakonov-Perel' mechanism

Spin relaxation can be described as precession of a spin around a varying magnetic field. In the D'yakonov-Perel' mechanism the effective magnetic field, e.g. due to the Rashba and Dresselhaus terms, leads to the spin relaxation. The zero-field spin splitting in non-centrosymmetric semiconductors for  $\mathbf{k} \neq 0$ , leads to an effective magnetic field  $\mathbf{B}_{\text{eff}}(\mathbf{k})$ , whose direction and amplitude usually depend on  $\mathbf{k}$ :

$$\boldsymbol{\Omega}(\mathbf{k}) = \frac{2}{\hbar} \mathbf{B}_{\text{eff}}(\mathbf{k}). \quad (34)$$

Here  $\boldsymbol{\Omega}$  is a vector about which the spin precesses with the rotation frequency  $|\boldsymbol{\Omega}| = \omega$ . After the momentum relaxation time  $\tau_p$ , the electron is scattered and its  $\mathbf{k}$  alters. Therefore, also  $\boldsymbol{\Omega}(\mathbf{k})$  changes randomly and the spin now precesses about another axis. Usually we consider the collision dominated limit  $\omega\tau_p \ll 1$ , in which the spin rotates very slowly compared to the momentum relaxation time. Many of these small rotations around different  $\boldsymbol{\Omega}$  finally lead to the loss

of the initial spin orientation. Therefore, the spin relaxation time  $\tau_s$  decreases for longer  $\tau_p$ , as then the spin rotates by a larger angle during two successive collisions, or larger rotation frequency  $\omega$ :

$$\frac{1}{\tau_s} \propto \langle \Omega^2 \tau_p \rangle. \quad (35)$$

Here the brackets refer to the average over the electron energy distribution. If in Eq. (35)  $\tau_p$  is replaced by a temperature dependent parameter  $\tau^*$ , then a temperature dependent spin relaxation time is obtained:

$$\frac{1}{\tau_s} = \omega_L^2 \tau^*. \quad (36)$$

With the effective Larmor frequency  $\omega_L$  at the Fermi energy at  $T = 0$  K.

In very clean materials, where the momentum relaxation time  $\tau_p$  is very long and the electrons are rarely scattered, we can obtain the case  $\omega\tau_p \gg 1$ . Now, the precession frequency is high compared to  $\tau_p$  and the spin performs a complete or even more rotations. In this case, a spin component perpendicular to  $\mathbf{B}_{\text{eff}}$  relaxes quickly, in contrast a parallel component remains for  $t < \tau_p$ . After a change of the magnetic field direction, the spin loses its orientation completely. Hence, for this process the spin relaxation time is proportional to the momentum relaxation time:  $\tau_s \propto \tau_p$ .

The D'yakonov-Perel' mechanism is mainly responsible for the spin relaxation at high temperatures. Furthermore, it is strongly enhanced in 2D structures compared to bulk materials, thus, this mechanism dominates the relaxation in  $n$ -doped QWs [49, 72].

### 2.3.2 Elliott-Yafet mechanism

Besides the dominating D'yakonov-Perel' mechanism also another process, the Elliott-Yafet mechanism, may contribute to the spin relaxation in  $n$ -type QWs. In this mechanism, the spin loses its orientation due to electron spin-flip scattering, caused by the  $\mathbf{k}$ -dependent admixture of valence-band states to the conduction band wave function. This admixture of VB states, with opposite spin orientation, to the CB states results from the SOI. Owing to that, the

Bloch states are no more spin eigenstates. Thus, scattering of electrons by impurities or phonons also has a certain probability for spin-flip transitions. This spin-flip scattering occurs via a virtual valence band state. In QW structures the spin relaxation time based on the Elliott-Yafet mechanism is given by:

$$\frac{1}{\tau_s(E_e)} \approx \left( \frac{\Delta_{\text{SO}}}{E_g + \Delta_{\text{SO}}} \right)^2 \left( \frac{E_{e1} E_e}{E_g^2} \right) \frac{1}{\tau_p(E_e)}, \quad (37)$$

where  $E_e$  is the electron kinetic energy and the ratio  $E_e/E_g$  reflects the admixture of the valence and conduction band wavefunctions. Equation (37) shows that the Elliott-Yafet mechanism depends on the quantum-confinement energy  $E_{e1}$  [49]. This effect increases with the strength of the SOI, hence the Elliott-Yafet mechanism is important in narrow band gap semiconductors, as e.g. InSb.

## 2.4 Weak localization and weak antilocalization

As previously discussed, the Rashba/Dresselhaus-ratio is accessible via photocurrent measurements. Beyond that, the relative strengths of these terms become manifest in magneto-transport measurements, as well. Here, the transition from weak antilocalization (WAL) to weak localization (WL) and back

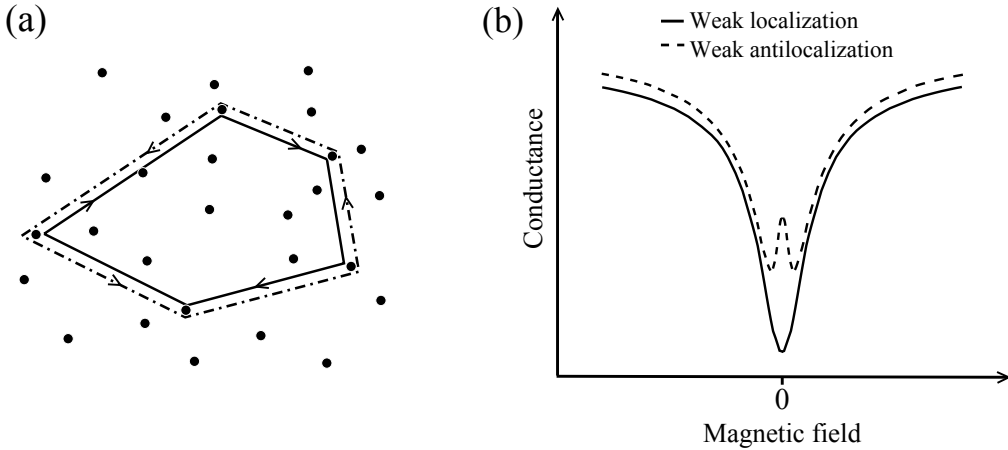


**Figure 13:** (a) Time-reversed trajectories of two electron waves, scattered at the same centers (defects or impurities). (b) Characteristic dependence of the conductance on  $\mathbf{B}$  for WL and WAL.

to WAL can be observed under the variation of a gate voltage. Thereby, the occurrence of the WL indicates equal strengths of Rashba and Dresselhaus terms. In contrast to the photocurrents, the magneto-transport is sensitive to both, first and third order harmonics of  $\Omega_{\mathbf{k}}$  (see Eqs. (18)). In this section, the theoretical basics, leading to the transition WAL-WL-WAL, will be briefly considered [73–76].

At low temperatures weak localization (WL) occurs in metals and semiconductors, hereby the conductance drops below the classical value given by the Drude formula. This deviation can be explained by a quantum interference correction resulting in an increased backscattering of the electrons. The WL arises due to the positive interference of two time reversal symmetric electron waves, propagating in opposite directions along a closed path (see Fig. 13(a)). This positive interference causes the decreased conductance (increased resistance) in the magneto-transport measurements. The WL can be suppressed by an external magnetic field applied perpendicularly to the 2DEG that destroys the time reversal symmetry. Hereby, the electrons experience a  $\mathbf{B}$ -proportional phase shift, while traversing the closed trajectory, and thus interfere no longer constructively. Fig. 13(b) shows the typical WL behavior in the magnetic field dependence of the conductance, exhibiting a minimum at  $\mathbf{B} = 0$ .

The weak antilocalization (WAL) can be understood, if we also consider the electron's spin and the Rashba or Dresselhaus spin orbit interaction (SOI). The WAL leads to an increase in the zero  $\mathbf{B}$ -field conductivity and suppresses the WL. Since  $\mathbf{B}_{\text{eff}}$  and thus, the spin relaxation usually depends on  $\mathbf{k}$ , the SOI leads to distinct spin precessions of both electrons, while they are moving along different directions along the closed trajectory. This finally leads to different spin orientations of the electrons after the trajectory and thus, modifies the interference. Now, also a destructive interference is possible, leading to the increase in conductivity (decrease of resistance), which is characteristic for the WAL (see Fig. 13(b)). A special case emerges, if the persistent spin helix condition is fulfilled: When the  $\mathbf{k}$ -linear Rashba and Dresselhaus terms are of equal strength,  $\mathbf{B}_{\text{eff}}$  points for each  $\mathbf{k}$  along the  $[1\bar{1}0]$  direction (see Sect. 4.2). Now, both spins precess along the same axis (or the spin relaxation is suppressed, depending on the orientation of the spin), which yields equal spin

orientations of the electrons after passing the closed trajectory. This results in positive interference and WL in the magneto-conductance.

### 3 Experimental methods

In the previous chapter it was discussed how the relative strengths of Rashba and Dresselhaus spin splittings can be deduced from the amplitudes of different photocurrents. This chapter will be focused on the experimental setup and methods that allow the observation and investigation of these THz laser radiation induced photocurrents. Therefore, the system that generates the THz laser pulses will be introduced as well as wave plates, which allow the variation of the polarization state, and the complete experimental setup, containing the electric devices for signal processing. Furthermore the investigated samples, GaAs and InGaAs quantum well structures, are presented. Additionally to the photocurrents, three more effects were investigated: Photoluminescence (PL), time resolved Kerr rotation (TRKR) and magneto transport. They are briefly addressed at the end of this chapter.

#### 3.1 THz laser source

The investigated photocurrents originate in our samples mostly due to Drude absorption of intense THz laser pulses. There are some devices generating such laser radiation, e.g. the free electron laser [77]. For this work, we used a more convenient one: A molecular gas laser that is optically pumped by a transversely excited atmospheric pressure (TEA) CO<sub>2</sub> laser [32, 78, 79]. This type of lasers was established by Chang and Bridges in 1969 [80] for continuous wave (cw) operation, de Temple introduced the pulsed mode in 1974 [81]. Subsequently the used ammonia gas laser, which is not so commonly known but effectively generates intensive monochromatic THz radiation, will be explained briefly.

The NH<sub>3</sub> laser converts the mid-infrared (MIR) pump radiation of the CO<sub>2</sub> laser into far-infrared (FIR) radiation of different wavelengths. Thereby the MIR radiation excites vibrational modes ( $\nu_2$ ) of the ammonia molecule and a population inversion between upper and lower rotational levels ( $J$ ) results in both vibrational states. The following transitions between rotational modes of NH<sub>3</sub> yield laser radiation in the THz frequency range, see Fig. 14(a). Required therefor is the permanent electric dipole moment of the ammonia molecule.

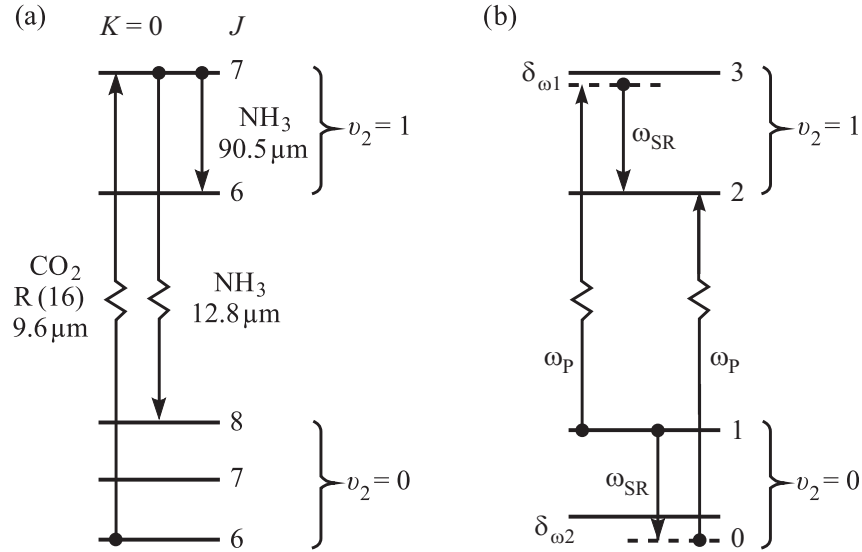


**Figure 14:** (a) Excitation of  $\text{NH}_3$  vibrational modes  $\nu_2$  via  $\text{CO}_2$  laser radiation and following rotational transitions.  $K$  is the projection of the angular momentum  $J$  on the molecule's symmetry axis. (b) Principle of Raman transitions.

The  $\text{NH}_3$  laser belongs to the group of Raman lasers, here, due to the high pump intensities of the TEA  $\text{CO}_2$  laser, the THz laser radiation originates predominantly from stimulated Raman transitions [81]. This allows laser emission even for a relative high frequency mismatch up to some GHz [82]. Figure 14(b) demonstrates Raman scattering in a four-level system after pumping at a frequency  $\omega_p$ . In this process, the frequency of the emitted photon  $\omega_{\text{SR}}$  differs from the resonance frequency either by  $\delta_{\omega_1}$  in the intermediate or by  $\delta_{\omega_2}$  in the initial state [83]. If  $\omega_{\text{SR}}$  is smaller than the resonance frequency, it is called Stokes line, else anti-Stokes line. With this kind of laser the whole THz range can be covered by strong discrete laser lines, depending on the pump wavelength and the used active media (besides ammonia several other media are possible, as e.g.  $\text{D}_2\text{O}$ ,  $\text{CH}_3\text{F}$  or  $\text{CH}_3\text{OH}$ ) [84].

Figure 15 illustrates schematically the experimental implementation of an ammonia laser. Here, MIR pump radiation is coupled into the  $\text{NH}_3$  filled glass resonator via a  $\text{BaF}_2$  lens through a  $\text{NaCl}$  window, which is placed outside of the focus due to the there prevailing high intensities. Two gold coated

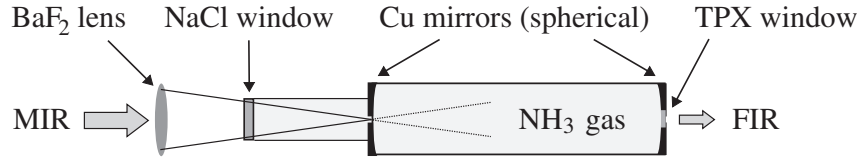


**Figure 15:** Pulsed  $\text{NH}_3$  laser with optical components.

spherical copper mirrors, adjusted to the optical axis of the pump laser and the ammonia resonator, assure the maximal absorption and conversion of the MIR into THz radiation. The mirrors are semitransparent due to holes of different diameters in their centers. The resonator is enclosed by a TPX (4-Methylpenthen-1) window on the output side, which acts as filter and absorbs leftovers of the MIR pump radiation but not the emitted THz radiation. All optical components are also transparent in the visible spectral range and thus allow the alignment of the setup and the samples by a red HeNe laser. The generated monochromatic laser pulses exhibit a Gaussian beam profile, peak powers  $P_p$  of several tens of kW depending on the wavelength and a pulse duration  $t_p$  of about 100 ns, repeating the temporal shape and repetition rate of the  $\text{CO}_2$  pump laser (about 1 Hz).

### 3.2 Variation of the laser radiations's polarization state

The above discussed  $\text{NH}_3$  laser emits linearly polarized THz radiation. For the experiments in this work it is on the one hand important to vary the polarization state, and direction and on the other hand to irradiate the samples with unpolarized light. The polarization state of light can be completely described by the Stokes parameters, altered by retardation wave plates and destroyed by a metal cone. For the THz frequency range  $\lambda/2$ - and  $\lambda/4$ -plates are manufactured for each wavelength from birefringent  $x$ -cut crystalline quartz.

There are four Stokes parameters  $s_0$ ,  $s_1$ ,  $s_2$  and  $s_3$  [85–87]. They provide information about the position of the electric field  $\mathbf{E}$  in the  $xy$  plane of a

fully polarized monochromatic wave propagating along  $-z$  (sample coordinate system):

$$s_0 = |E_x|^2 + |E_y|^2 = |E|^2 = I, \quad (38)$$

$$s_1 = |E_x|^2 - |E_y|^2, \quad (39)$$

$$s_2 = E_x E_y^* + E_y E_x^*, \quad (40)$$

$$s_3 = i(E_x E_y^* - E_y E_x^*) = -P_{\text{circ}} I. \quad (41)$$

Here,  $s_0$  characterizes the radiation's intensity but gives no information about the polarization state, this coefficient is the only remaining for unpolarized light. The parameters  $s_1$  and  $s_2$  describe the linear polarization within the axes  $x$  and  $y$  and within the system rotated by  $45^\circ$ , respectively. The helicity, or circular polarization, of light is given by  $s_3$ . It reaches  $+1$  for right-handed,  $-1$  for left-handed circularly polarized radiation and vanishes for linear polarization. To describe elliptically polarized light, all four Stokes parameters are necessary.

The polarization state of light and thus the Stokes coefficients can be altered by passing the radiation through a wave plate. Thereby, due to birefringence, the beam is splitted into two partial light beams, the ordinary (o) and the extraordinary (eo) one, exhibiting orthogonal polarizations [88]. The ordinary beam is polarized perpendicularly  $E_\perp$  to the optical axis  $c$  of the wave plate and experiences the refractive index  $n_o$ . The extraordinary beam is in contrast polarized parallel to  $c$ ,  $E_\parallel$ , and feels a different refractive index  $n_{eo}$  [32, 89, 90]. Out of these two unequal optical densities, diverging propagation velocities and hence, an optical retardation  $\Delta l$  results, which is correlated to a phase shift  $\Delta\phi$  of these two beams:

$$\Delta l = d (n_{eo} - n_o), \quad (42)$$

$$\Delta\phi = \frac{2\pi d}{\lambda} (n_{eo} - n_o). \quad (43)$$

Equation (43) allows to estimate the adequate thickness  $d$  of the wave plate for a certain wavelength  $\lambda$ . In the following, two important cases are examined more closely: The  $\lambda/2$ -plate, which is used to rotate the  $\mathbf{E}$ -field vector

of linearly polarized light and the  $\lambda/4$ -plate that provides elliptically and in particular circularly polarized radiation.

A  $\lambda/2$ -plate permits to control the parameters  $s_1$  and  $s_2$ , therefore an appropriate thickness  $d$  has to be selected to obtain a phase shift of  $\Delta\phi = (2m + 1)180^\circ$  in the order  $m$  for a certain wavelength  $\lambda_0$ . In zero order, the following plate thickness  $d$  results for a given difference between the refractive indices  $\Delta n$ :

$$d = \frac{\lambda_0}{2} \frac{1}{\Delta n}. \quad (44)$$

For higher orders of  $m$  wave plates are also possible, but then their thickness increases, which leads to an enhanced absorption of the transmitted radiation. Figure 16 illustrates the operating mode of a  $\lambda/2$ -plate. The electric field vector of the transmitted light  $\mathbf{E}_t$  is rotated by the azimuth angle  $\alpha$  with respect to the initial polarization  $\mathbf{E}_i$  of a normally incident beam. The resulting phase shift of  $180^\circ$  can be regarded as sign change between  $E_\perp$  and  $E_\parallel$  that leads e. g. to the reflection of  $E_\perp$  in the  $c$  axis. The angle  $\alpha$  equals  $2\beta$  and  $\beta$  indicates the rotation angle of the wave plate. With  $\beta$  running from  $0^\circ$  to  $90^\circ$  one can cover all possible angles of  $\mathbf{E}_t$  within the  $xy$  plane.

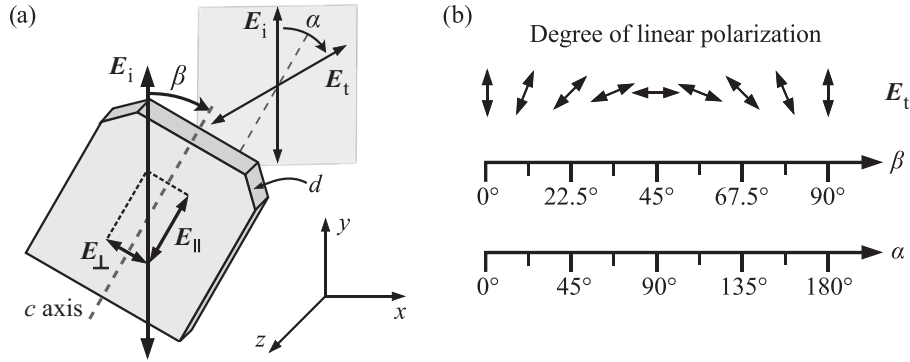


**Figure 16:** (a) Sketch of a  $\lambda/2$ -plate with initial and final polarizations of the radiation, (b) degree of linear polarization.

The  $\lambda/4$ -plate enables a variation of the helicity of light, which is characterized by the last Stokes parameter  $s_3$ . By this means, linear polarization can be transformed into circular. Therefore, a phase shift between ordinary and

extraordinary beam of  $\Delta\phi = (2m + 1)90^\circ$  is necessary, which corresponds to a plate thickness of:

$$d = \frac{\lambda_0}{4} \frac{1}{\Delta n}. \quad (45)$$

Figure 17 illustrates the operating mode of a  $\lambda/4$ -plate. Here the angle  $\varphi$  lies between the initial polarization and the  $c$  axis of the plate. For  $\varphi = 45^\circ$  (or  $225^\circ$ ) right-handed circularly polarized radiation ( $\sigma^+$ ) results, for  $\varphi = 135^\circ$  (or  $315^\circ$ ) left-handed circularly polarized light ( $\sigma^-$ ) is generated. In case  $\mathbf{E}_i$  is parallel or perpendicular to  $c$  only one component exists and the transmitted light remains linearly polarized ( $\mathbf{E}_i = \mathbf{E}_t$ ). Any other rotation angle  $\varphi$  yields elliptically polarized light.

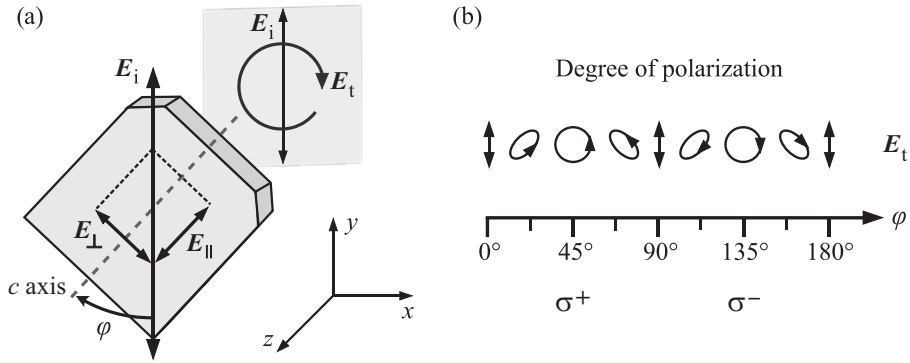


**Figure 17:** (a) Sketch of a  $\lambda/4$ -plate with initial and final polarizations of the radiation, (b) degree of polarization.

Since retardation plates change the polarization state of light, the Stokes parameters can also be denoted in terms of the rotation angles  $\alpha$  and  $\beta$  for  $\lambda/2$ - and  $\lambda/4$ -plate, respectively. The equations (46)-(48) present  $s_1$ ,  $s_2$  and  $s_3$  normalized to the intensity  $s_0$ .

$$\frac{s_1}{s_0} = \frac{|E_x|^2 - |E_y|^2}{|E|^2} = -\cos 2\alpha = -\frac{1 + \cos 4\varphi}{2}, \quad (46)$$

$$\frac{s_2}{s_0} = \frac{E_x E_y^* + E_y E_x^*}{|E|^2} = \sin 2\alpha = \frac{\sin 4\varphi}{2}, \quad (47)$$

$$\frac{s_3}{s_0} = \frac{i(E_x E_y^* - E_y E_x^*)}{|E|^2} = -P_{\text{circ}} = -\sin 2\varphi. \quad (48)$$

One part of the experiments in this work was carried out under illumination with unpolarized FIR laser radiation [7]. To destroy the linear polarization of the laser beam, a brass cone is utilized. While the beam traverses the cone, multi reflections on its inner surface appear, which unpolarize the laser radiation. Figure 18 depicts the longitudinal section through the used metal cone.

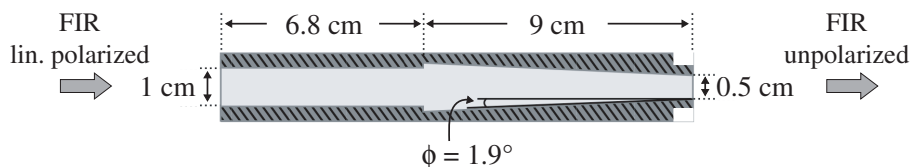


**Figure 18:** Draft of the used brass cone generating unpolarized light.

It consists of two parts, the first one is a tube of 6.8 cm length, the second one is the 9 cm long real cone. Its aperture angle of about  $4^\circ$  results from twice  $\phi$ . The that way created unpolarized laser pulses are strongly diverging, thus adjacent optical components or the sample have to be placed very closely behind the cone's outlet port. The in Fig. 18 illustrated combination of cone and tube has turned out to give the best results for radiation with a wavelength of  $280 \mu\text{m}$ . This was proved by a grating, acting as polarizer, and a detector placed directly after the cone. Figure 19(a) shows the dependence of the detected radiation intensity on the rotation angle  $\gamma$  of the grating about

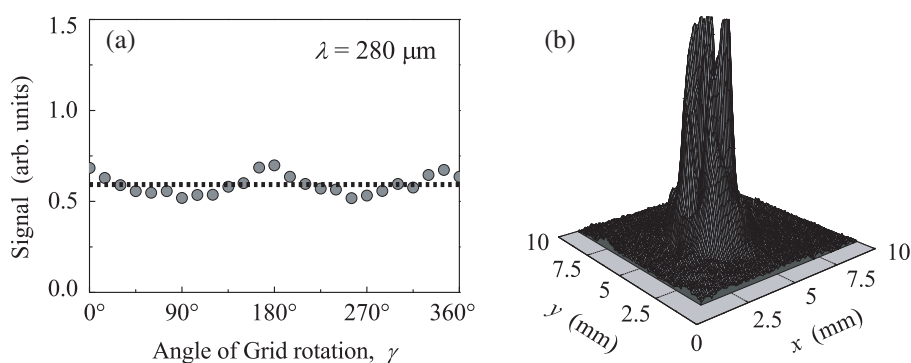


**Figure 19:** Characteristics of the unpolarized THz pulses at a wavelength of  $\lambda = 280 \mu\text{m}$ . (a) Beam intensity as function of the rotation angle  $\gamma$  of the grid, measured by a photon drag detector “PD5F”. (b) Spatial beam shape, measured by a pyroelectric camera “Spiricon”.

the optical axis. This signal is almost constant evidencing unpolarized radiation. For linearly polarized light, such a measurement would exhibit a strong dependence of the radiation intensity and even a vanishing signal for certain values of  $\gamma$ . Figure 19(b) depicts the spatial beam profile of an unpolarized pulse, measured directly behind the cone by a pyroelectric camera. It exhibits an almost Gaussian shape with its spot size determined by the cone's outlet port.

### 3.3 Experimental setup and calibration

Following to the introduction of the THz laser source and the most important optical components, in this paragraph the entire experimental setup, the electronic devices and its interplay will be explained. Figure 20 illustrates that all individual components interact via the General Purpose Interface Bus (GPIB).

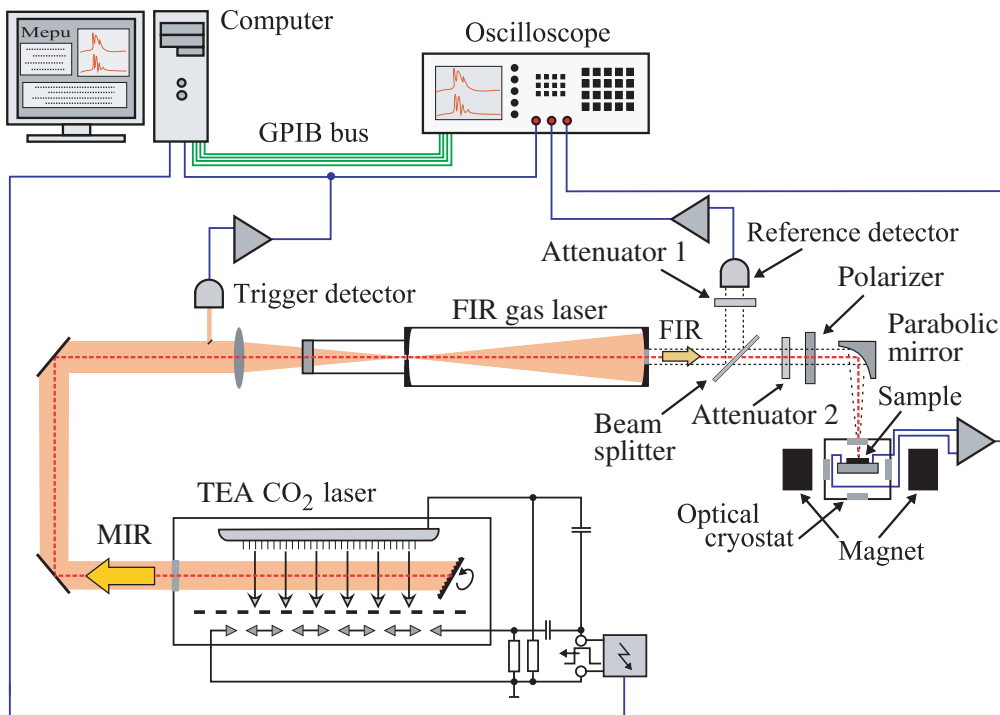


**Figure 20:** Experimental setup containing pulsed high power THz laser, TEA CO<sub>2</sub> pump laser, optical components and measuring electronics.

or the parallel printer port and are regulated by a program developed with the software LabView. For instance, the laser system, electro magnet and step motor, which rotates the wave plates or grid polarizer, are actuated via the measuring program on the PC. This program also allows a continuously read-out of all parameters, as magnetic field strength, rotation angle, temperature, voltage from the reference detector or signal from the sample and stores them in a file. The THz radiation induced signals are detected via the voltage drop over a  $50 \Omega$  load resistance, increased by very fast amplifiers and digitalized by a 1 GHz digital storage oscilloscope. These high frequency electronics are required to resolve the temporal shape of our 100 ns long laser pulses that equates to a frequency of 10 MHz. For magnetic field dependent measurements a water cooled magnet, which can reach field strengths up to  $B \leq 0.6$  T without concentrators and  $B \leq 1$  T with concentrators, is used. For temperature dependent experiments, the samples can be mounted into a direct flow optical cryostat system that also fits into the magnet ( $B \leq 0.6$  T).

The investigations with unpolarized light need small changes in the setup, here very small distances between the individual optical components are of great importance to increase the signal to noise ratio. Moreover, no focusing parabola mirror is necessary here. Figure 21 sketches the modifications in the setup used for unpolarized radiation.

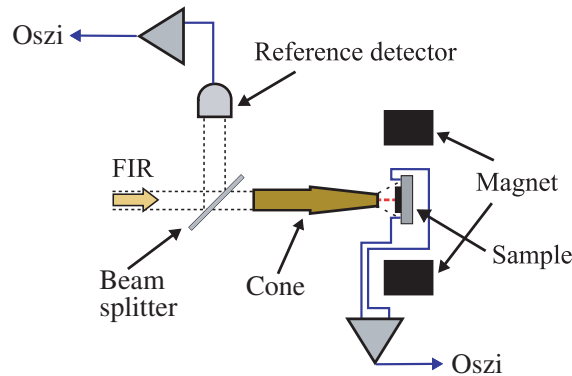


**Figure 21:** Experimental setup, modified for unpolarized THz pulses.

To check the beam quality in the THz region, a Michelson interferometer can be utilized to estimate the exact wavelength, mode structure and beam size

can be tested by a pyroelectric camera (see Fig. 19). This camera visualizes the intensity distribution via a square sized detector area of half an inch side length. Its resolution amounts to 0.1 mm (128 rows times 128 columns of small pyroelectric sensors) and photon energies in a wide range from the microwave up to the ultraviolet (UV) region can be detected. Not only the beam quality, but also the exact radiation power for each pulse incident on the sample is of great importance for the data analysis. Therefore, for each photocurrent measurement a calibration of the setup is necessary. This is done by replacing the sample by a second “PD5F” detector and estimating the ratio of the intensities at the reference detector and the second one. This ratio depends on the wavelength, since the mylar beam splitter’s transmission and reflection spectra also depend on it. Moreover, all optical components as retardation wave plates, cones, grid polarizers, filters or attenuators have different absorption and reflection characteristics, which influence the estimated ratio of intensities. The signal of the reference detector therefore allows to calculate the intensity on the sample for each individual pulse during the measurement.

### 3.4 Description and preparation of the studied samples

In this section the investigated samples are characterized more closely. All heterostructures are grown by molecular-beam epitaxy (MBE) on (001)-oriented substrates and  $n$ -type modulation doped with silicon. All structures based on GaAs were grown in Regensburg (D. Schuh), the InGaAs based in Sendai (J. Nitta). Each sample is square shaped with edges of 5 mm length (besides two structures, where the contacts are placed on a circle of 8 mm diameter) oriented along the  $[1\bar{1}0]$  and  $[110]$  crystallographic axes. For photocurrent mea-

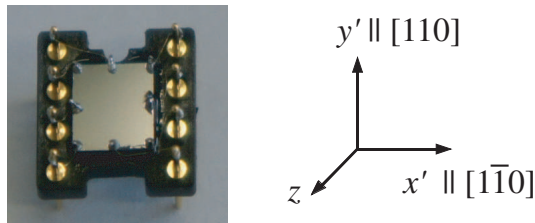


**Figure 22:** Sample with eight Indium contacts.

measurements ohmic Indium contacts were alloyed on the sample corners and in the middle of each sample side allowing to probe the photocurrent along different directions (see Fig. 22). The in this work analyzed quantum well (QW) structures differ in their material composition, well width, doping position and concentration. These samples can be divided into three groups. Within each sample set, the structures are differing in only a few selected parameters to determine their influence.

### 3.4.1 Set I: GaAs QWs differing in the doping position

Set I comprises Si- $\delta$ -doped GaAs/Al<sub>0.3</sub>Ga<sub>0.7</sub>As multiple QWs (fifteen in series) and was fabricated at typical temperatures in excess of 600°C (asides from sample 5LT). With sample set I the influence of the doping profile was analyzed, thus structures essentially differing in the position of the  $\delta$ -doping layers were grown, thereby the QW width of all samples was kept constant at 15 nm and the distance between two adjacent doping layers always amounts to 185 nm. With sample 5LT the influence of the temperature during the growth of  $\delta$ -doping and subsequent layers was investigated. Figure 23 sketches the conduction band edge of two different QWs together with the corresponding  $\delta$ -doping positions. In all structures apart from sample 4 and 5LT, the doping layers are asymmetrically shifted off the barrier center either to the left or to the right. The impurities' Coulomb field yields an asymmetric potential profile inside the QWs. In order to describe the degree of asymmetry we introduce

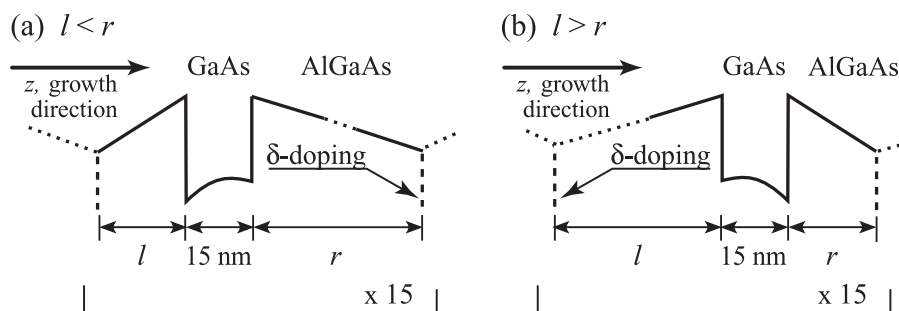


**Figure 23:** Set I: Conduction band profiles for two different samples with (a) negative  $\chi$  and (b) positive  $\chi$  and corresponding doping positions.

Sample	Spacer $l$ (nm)	Spacer $r$ (nm)	$\chi = \frac{l-r}{l+r}$	$n_s$ (RT) $10^{11}(\frac{1}{\text{cm}^2})$	$\mu$ (RT) $10^3(\frac{\text{cm}^2}{\text{Vs}})$	$T_\delta$ (°C)
1	20	165	-0.78	1.2	7.2	615
2	45	140	-0.51	1.6	7.7	631
3	70	115	-0.24	1.4	8.0	631
4	92.5	92.5	0	1.4	7.7	631
5LT	92.5	92.5	0	1.0	7.9	490
6	106.5	78.5	0.15	1.4	8.1	626
7	111	74	0.20	1.4	8.1	632
8	125	60	0.35	1.4	7.7	629
9	140	45	0.51	1.4	7.9	630
10	165	20	0.78	1.5	8.0	625

**Table 1:** Set I: Sample parameters. Carrier densities  $n_s$  (per QW-layer) and mobilities  $\mu$  are room temperature values.

the parameter  $\chi = (l - r)/(l + r)$ , where  $l$  and  $r$  are the spacer layer thicknesses between the well and the  $\delta$ -layers. For  $\chi < 0$  the doping layers on the substrate side are closer to the well, for  $\chi > 0$  the Si-doping on the surface side is located closer. Thus, for increasing  $\chi$  the well is shifted towards the surface, within two adjacent doping layers. Temperatures  $T_\delta$  during the growth of the  $\delta$ -doping and subsequent layers, which determine the segregation, mobilities  $\mu$  and carrier densities  $n_s$ , measured at room temperature are given in Table 1.

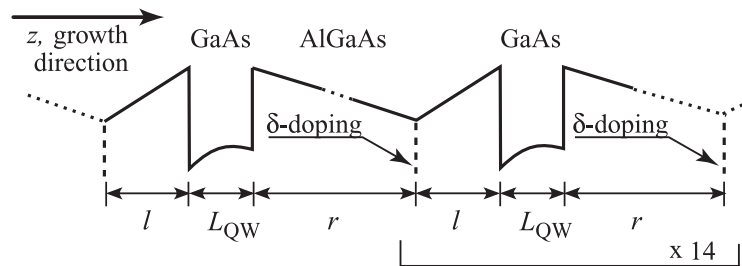


**Figure 24:** Set II: Conduction band structure.

### 3.4.2 Set II: GaAs QWs differing in the well width

Also the second set consists of Si- $\delta$ -doped GaAs/Al<sub>0.3</sub>Ga<sub>0.7</sub>As structures grown at typical temperatures in excess of 600°C. With this set of samples the influence of the well width  $L_{\text{QW}}$  was investigated, thus structures with  $L_{\text{QW}}$  varying from 4 to 30 nm and equal doping profile were grown. Figure 24 sketches the conduction band edge of the multiple QW structures together with the corresponding  $\delta$ -doping positions, and Table 2 gives the sample (Sa.) parameters. Necessary data, obtained applying photoluminescence and time resolved Kerr rotation measurements (see section 3.5 for details), are also listed. Fifteen multiple QWs in a row were grown to increase the signals. The doping layers are asymmetrically shifted by two different spacer (Sp.) layer thicknesses,  $l$  and  $r$ , with respect to the QW. In addition, in all samples, except A, the sum ( $l + r + L_{\text{QW}}$ ) was kept constant. The impurities' Coulomb field yields an asymmetric potential profile inside the QWs causing SIA. This asymmetry is given by the parameter  $\chi$ , which is in all samples, besides A, similar.

Sa.	$L_{\text{QW}}$ (nm)	Sp. $l$ (nm)	Sp. $r$ (nm)	$\chi =$ $\frac{l-r}{l+r}$	$n_s$ $10^{11}(\frac{1}{\text{cm}^2})$	$\mu$ $10^5(\frac{\text{cm}^2}{\text{Vs}})$	$\tau_p$ (ps)	$g^*$	$\Delta E$ (meV)	$n_s$ (RT) $10^{11}(\frac{1}{\text{cm}^2})$	$\mu$ (RT) $10^3(\frac{\text{cm}^2}{\text{Vs}})$
A	4	45	140	-0.51	1.17	0.509	1.9	0.13	-	1.4	4.8
B	6	74.5	119.5	-0.23	0.874	0.925	3.5	0.106	-	1.3	5.5
C	8.2	73.4	118.4	-0.23	1.11	1.23	4.7	-0.06	-	1.3	6.6
D	10	72.5	117.5	-0.24	1.09	4.95	18.8	-0.157	116	1.3	7.4
E	15	70	115	-0.24	1.26	3.47	13.2	-0.29	59	1.4	8.0
F	20	67.5	112.5	-0.25	1.19	0.642	2.4	-0.337	47	1.2	8.0
G	30	62.5	107.5	-0.26	1.17	12.6	47.9	-0.394	48	1.2	8.2

**Table 2:** Set II: Sample Parameters. Carrier density  $n_s$  (per QW-layer), mobility  $\mu$ , momentum scattering time  $\tau_p$  calculated from the mobility, measured  $g^*$  factor and energy difference  $\Delta E$  between the transitions (e2hh2)-(e1hh1) are given for  $T = 4.2$  K. Also listed: Carrier density  $n_s(\text{RT})$  (per QW-layer) and mobility  $\mu(\text{RT})$  measured at room temperature.

### 3.4.3 Set III: InGaAs QWs differing in the well width

The third set of samples contains Si- $\delta$ -doped  $\text{In}_{0.53}\text{Ga}_{0.47}\text{As}/\text{In}_{0.52}\text{Al}_{0.48}\text{As}$  single QWs. This material is interesting due to its strong spin orbit interaction (SOI). With these samples, a QW fulfilling the persistent spin helix condition should be obtained. Therefore, structures that are doped in the same way but have different well widths were grown. Since in an InGaAs 2DEG [91] the Dresselhaus SOI is usually much smaller than the Rashba SOI, BIA has to be enhanced and SIA reduced to achieve a persistent spin helix. Hence, narrow QWs with  $L_{\text{QW}} = 4$  nm and  $L_{\text{QW}} = 7$  nm, which are symmetrically doped, were designed. In both samples, left and right spacer thicknesses are 6 nm ( $\chi = 0$ ), the substrate sided  $\delta$ -doping layer has a charge carrier density of  $n_{\text{d}} = 1.2 \times 10^{18}\text{cm}^{-3}$  the surface sided amounts to  $n_{\text{d}} = 3.2 \times 10^{18}\text{cm}^{-3}$ . Figure 25(a) and (b) show the schematic cross section as well as the conduction band structure and wave function distribution for the 4 and 7 nm broad InGaAs QWs. To probe the photocurrent along several different directions

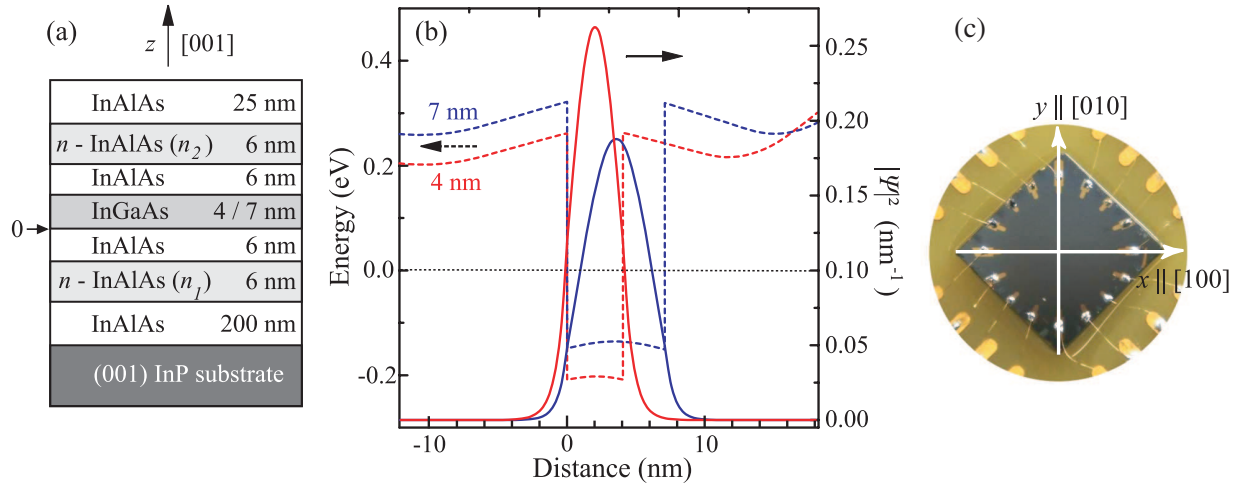


**Figure 25:** Set III: (a) Schematic cross section of the studied structures. (b) Conduction band profile with the Fermi energy at  $E_{\text{F}} = 0$  and normalized electron probability density  $|\psi|^2$  for both QWs, calculated via a Poisson-Schrödinger solver by J. Nitta's group. (c) Sample with 16 contact pads equally separated and adjusted to a circle of 8 mm diameter.

Sample	Number of Contacts	$L_{\text{QW}}$ (nm)	Spacer $l$ (nm)	Spacer $r$ (nm)	$\chi =$ $\frac{l-r}{l+r}$	$n_s$ $10^{12}(\frac{1}{\text{cm}^2})$	$\mu$ $10^4(\frac{\text{cm}^2}{\text{Vs}})$
(i)	8	4	6	6	0	4.26	2.82
(ii)	16	4	6	6	0	4.26	2.82
(iii)	8	7	6	6	0	3.47	2.46

**Table 3:** Set III: Sample parameters. Carrier densities  $n_s$  and mobilities  $\mu$  measured at 4.2 K.

and map its distribution in the QW plane, additionally another geometry was designed. Figure 25(c) depicts this sample geometry, chosen for sample (ii), it has eight pairs of ohmic gold contacts that are equally separated and adjusted to a circle of 8 mm diameter. These contacts are again arranged in such a way that the current can be measured exactly along the cubic axes  $x \parallel [100]$  and  $y \parallel [010]$ . The only difference between sample (i) and (ii) is the geometry, both were fabricated from the same wafer. Table 3 gives the charge carrier densities  $n_s$  and mobilities  $\mu$ .

#### 3.4.4 Sample preparation

To determine the Rashba-Dresselhaus-ratio properly, square shaped samples are required. They permit to measure photocurrents exactly along the cubic axes ( $[100]$  and  $[010]$ ) and avoid parasitic projections on the crystallographic ones ( $[1\bar{1}0]$  and  $[110]$ ). This can be achieved by scratching the wafer parts into squares with a PC controlled, step motor driven, scraper and breaking them into peaces afterwards. This device allows to measure distances with an accuracy of 5  $\mu\text{m}$ . For optical measurements it is additionally important to remove the Ga layer from the substrate's backside. Therefor fuming hydrochloric acid (37 %) is used, while the frontside is protected by synthetic resin (Hot Mounting Wax Clear) during this 15 minutes long procedure. The resin can subsequently be removed by hot acetone and isopropanol (for flushing). Ohmic contacts are fabricated on the sample's surface with pure indium after slightly scratching the surface. The indium soldering point has to diffuse into the 2DEG, thus an annealing oven with protective atmosphere (90 % ni-

trogen and 10 % hydrogen, 900 mbar) is utilized. The GaAs QWs are heated up during 300 s to 460 °C, then the temperature remains at 460 °C for further 300 s. The InGaAs QWs, in contrast, are heated up during 60 s to 280 °C and then the temperature remains at 280 °C for further 360 s. This procedure avoids rectifying effects, this means the resistance of one contact pair remains the same for both current directions. The resulting contact consists of a thin, for electrons easy to tunnel, Schottky barrier within a highly doped surface layer of the semiconductor [92]. These contacts are afterwards connected with thin goldwires.

### 3.5 Time-resolved Kerr rotation and Photoluminescence measurements

In this work time-resolved Kerr rotation (TRKR) and photoluminescence (PL) techniques were used to study Landé factors and spin dynamics [21] on sample set II, therefore a pulsed Ti-sapphire laser system was applied. These measurements were carried out by C. Schüller's group in Regensburg and are addressed here only briefly. The Ti-sapphire laser generates pulses with a spectral linewidth of about 3 to 4 meV and a duration of about 600 fs. Its central wavelength is tuned to excite electron-hole pairs at the Fermi energy of the 2DEG in the samples. With TRKR measurements spin relaxation and spin

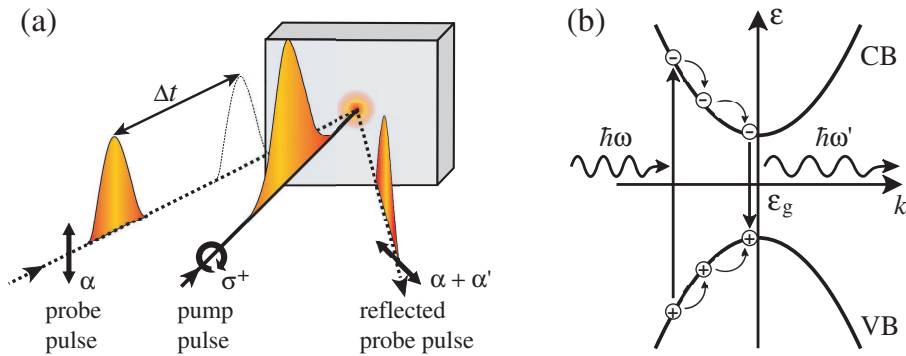


**Figure 26:** (a) Schematic of the time-resolved Kerr rotation. (b) Photoluminescence ( $\hbar\omega' < \hbar\omega$ ) caused by recombination of electron hole pairs.

dephasing times of the conduction band electrons can be estimated, and the damped Larmor precession of the optically oriented electron spin polarization allows the estimation of the  $g^*$ -factors. The laser pulse train is split into the pump beam, which is circularly polarized ( $\sigma^+$ ) and the weaker, linearly polarized ( $\alpha$ ) probe beam. The probe pulse is delayed with respect to the pump beam via a mechanical delay line. Both beams are focused onto the sample surface at near-normal incidence by an achromat, and the Kerr rotation angle of the reflected probe beam is measured using an optical bridge detector (see Fig. 26(a)). Hereby, the magneto-optic Kerr effect leads, in the presence of a spin polarization normal to the sample plane, to a small tilting angle  $\alpha'$  of the linear polarization in the reflected pulse. This angle  $\alpha'$  is proportional to the spin polarization in the sample. The typical power density used in the experiments was about  $40 \text{ W/cm}^2$  for the pump beam and  $4 \text{ W/cm}^2$  for the probe beam. A lock-in scheme is used to increase the sensitivity of the experiment. The samples were mounted in an optical cryostat and cooled by  $^3\text{He}$  gas to nominal temperatures of 4.5 K. Magnetic fields of up to 10 T were applied in the sample plane during the TRKR measurements.

To determine the electron confinement energies in the QWs, combined photoluminescence and photoluminescence excitation (PLE) measurements were performed. For PL measurements, the Ti-sapphire laser operated in cw mode and was tuned to higher energies to excite the samples nonresonantly. The excitation density for PL measurements was about  $4 \text{ W/cm}^2$ . Hereby, electron-hole pairs were created within the QWs, which thermalize and recombine afterwards, see Fig. 26(b). The PL emitted from the samples was collected using a grating spectrometer and a charge-coupled device (CCD) sensor. All PL measurements were performed without applied magnetic fields at nominal sample temperatures of 4.5 K. For PLE measurements, a tunable cw Ti-sapphire laser system was used. The PL intensity of the low-energy flank of the sample was recorded using the spectrometer and the CCD sensor as a function of the laser energy of the Ti-sapphire laser. The PL spectrum allows to detect the ( $e1-hh1$ ) transition in the QW, while the PLE spectrum reflects the ( $e2-hh2$ ) transition and the Fermi energy of the 2DEG in the QW.

### 3.6 Magneto transport measurements

Additionally to the previously introduced methods also magneto transport experiments were carried out on sample set III. These measurements were performed by J. Nitta's group in Sendai and will also be described shortly here. Therefor  $20\ \mu\text{m} \times 80\ \mu\text{m}$  gate-fitted Hall bar structures with an  $\text{Al}_2\text{O}_3$  gate insulator and a chrome-gold top gate electrode were processed from samples (i) and (ii) and investigated. Thus, an external magnetic field  $\mathbf{B}$  was applied perpendicularly to the QW plane and the magneto-conductance was measured for different gate bias voltages at  $T = 1.4\ \text{K}$ . Here, the gate voltage permits to tune SIA and hence, allows the gate control of the PSH state. In the experiment, with varying gate voltage, transitions from WAL to WL and back to WAL can be observed, visualizing the enhancement of the spin relaxation length around the WL region and consequently the realization of the PSH condition.

## 4 Influence of the $\delta$ -doping position on BIA and SIA

The two different material properties BIA and SIA (bulk and structure inversion asymmetry), emerging in zinc-blende based gyrotropic QW structures, and their accurate tailoring are of great importance in the growing field of spintronics. These asymmetries are the microscopic origins of the Dresselhaus and Rashba terms in the Hamiltonian,  $H_{\text{SO}} = \sum \beta_{lm} \sigma_l k_m$ . This Hamiltonian, in turn, originates from the spin-orbit interaction [4–6] and describes the spin-splitting in III-V semiconductor-based QWs (for details see Section 2.1). The resulting removal of spin degeneracy of the energy bands provides a versatile tool to achieve the following major goals of spintronics: the generation, manipulation and detection of spin polarized electrons in low dimensional semiconductors, see e.g. Refs. [4–6]. Hereby, the spin-splitting depends on the relative strengths of Dresselhaus and Rashba terms and permits the control of the spin polarization by an electric field, determines the spin relaxation rate and can be utilized for all-electric spin injection. The Dresselhaus term results from BIA and, thus, can be controlled by the QW width, temperature, and electron density. In contrast the Rashba term originates from SIA, which depends on the inversion asymmetry of the confining potential. One well known method to control SIA, uses the application of a gate voltage. It has been shown previously that photogalvanic effects are possible tools to analyze BIA and SIA in gyrotropic QW structures [52, 53]. Recently, it was demonstrated that SIA can be accurately tuned in (110)-grown GaAs QWs by a proper choice of the  $\delta$ -doping layer position [12].

In this work both SIA and BIA are investigated in modulation-doped (001)-grown GaAs/AlGaAs quantum wells employing the linear MPGE [7]. Studying sample set I, it is demonstrated that also in this structures, SIA can be precisely tailored by the  $\delta$ -doping layer position. Furthermore, it turns out that in (001)-oriented QWs, SIA is substantially affected by the segregation during the growth process of the structure. This is in contrast to (110)-grown QWs, where the segregation of doping atoms is suppressed [12]. The here performed experiments explore the segregation's role and reveal a substantial SIA

in symmetrically-doped (001)-structures, due to impurity segregation during the growth. With this results, it was possible to specify the growth conditions and obtain structures with a predetermined SIA. Moreover, SIA was tuned via the  $\delta$ -doping position, which permits the preparation of samples with almost equal degrees of structure and bulk inversion asymmetry and consequently with almost equal Rashba and Dresselhaus spin-splittings. Such structures enable the development of a non-ballistic spin-field effect transistor [15], as well as the creation of a persistent spin helix [16], furthermore they exhibit a drastic increase in spin relaxation time [35].

As already discussed in Section 2.2.1, the MPGE current is generated by the absorption of THz radiation in QWs under the presence of a magnetic field. More details, concerning the microscopic origin of the MPGE, can be found in the Refs. [6, 32, 51, 54]. In this chapter, the interplay between SIA and BIA is analyzed, using the previously mentioned approach, based on the symmetry equivalence of the tensors describing spin-splitting and photogalvanic effects (see Sect. 2.2). This approach can also be extended to the MPGE, which was demonstrated for (110)-grown QWs in Ref. [12]. In the following, it is shown that this method can be transferred to (001)-oriented structures, as well. After Ref. [51] and Section 2.2.1 the linear MPGE is given by the phenomenological equation:

$$j_\alpha = \sum_{\beta\mu\nu} \phi_{\alpha\beta\mu\nu} B_\beta (E_\mu E_\nu^* + E_\nu E_\mu^*)/2. \quad (49)$$

Under the excitation of (001)-grown QWs with unpolarized radiation at normal incidence Eq. (49) reduces to:

$$j_l = \sum_m \gamma_{lm} B_m |\mathbf{E}|^2. \quad (50)$$

Here,  $\gamma$  is a second rank pseudo tensor and  $|\mathbf{E}|^2 = I$  gives the radiation's intensity. Equation (50) can be rewritten as:

$$\mathbf{j}_{\text{MPGE}} = a \begin{pmatrix} \beta & -\alpha \\ \alpha & -\beta \end{pmatrix} \mathbf{B} |\mathbf{E}|^2, \quad (51)$$

where the constant  $a$  depends on the microscopic details of the MPGE. This provides a straight forward method to obtain the relative strengths and signs

of SIA and BIA. The MPGE due to unpolarized excitation as well as the spin-splitting exhibit the same anisotropy in space, since both are described by equivalent second rank pseudo tensors  $\boldsymbol{\gamma}$  and  $\boldsymbol{\beta}$ , whose irreducible components differ only by a scalar factor. Equation (51) shows clearly that, similarly to the band spin-splitting, also the MPGE current can be separated into contributions, which originate solely from SIA *or* BIA. Applying the in-plane magnetic field along a cubic axis, e.g. the  $y$ -direction, the following longitudinal ( $j_y \parallel [010]$ ) and transverse photocurrents ( $j_x \parallel [100]$ ) can be measured:

$$j_x = \gamma^{\text{SIA}} B_y |\mathbf{E}|^2, \quad j_y = \gamma^{\text{BIA}} B_y |\mathbf{E}|^2. \quad (52)$$

Here  $\gamma^{\text{SIA}}$  and  $\gamma^{\text{BIA}}$  are components of the tensor  $\boldsymbol{\gamma}$  due to SIA and BIA, respectively. In the ratio  $j_x/j_y$  all scalar factors, containing the microscopic details, are canceled, thus, the ratio of SIA to BIA is directly accessible. Furthermore, the analysis of each individual photocurrent, given in Eq. (52), reveals changes in strength and sign of SIA and BIA upon the variation of external parameters. In the following, the hereby obtained experimental results are introduced and discussed.

## 4.1 Experimental results

This experiment was carried out on sample set I, containing (001)-oriented Si- $\delta$ -doped  $n$ -type GaAs/Al<sub>0.3</sub>Ga<sub>0.7</sub>As structures grown by molecular-beam epitaxy. All of these QW structures have the same width of 15 nm but differ essentially in their doping profile, details are given in Table 1. The experiments were performed at room temperature, hereby all samples were irradiated under normal incidence of unpolarized terahertz (THz) laser radiation at a wavelength of 280  $\mu\text{m}$ . Using this photon energy, assures that only free carrier absorption results. The pulsed radiation ( $P \approx 5$  kW) is provided by an optically pumped NH<sub>3</sub> molecular laser [32]. Since unpolarized light is essential for the measurements, the in Sect. 3.2 described brass cone, which depolarizes the laser radiation via multiple reflections, was assembled directly in front of the samples. Additionally, an external in-plane magnetic field  $B = \pm 1$  T was applied along either  $x \parallel [100]$  or  $y \parallel [010]$ . The resulting MPGE currents  $J_x$  and

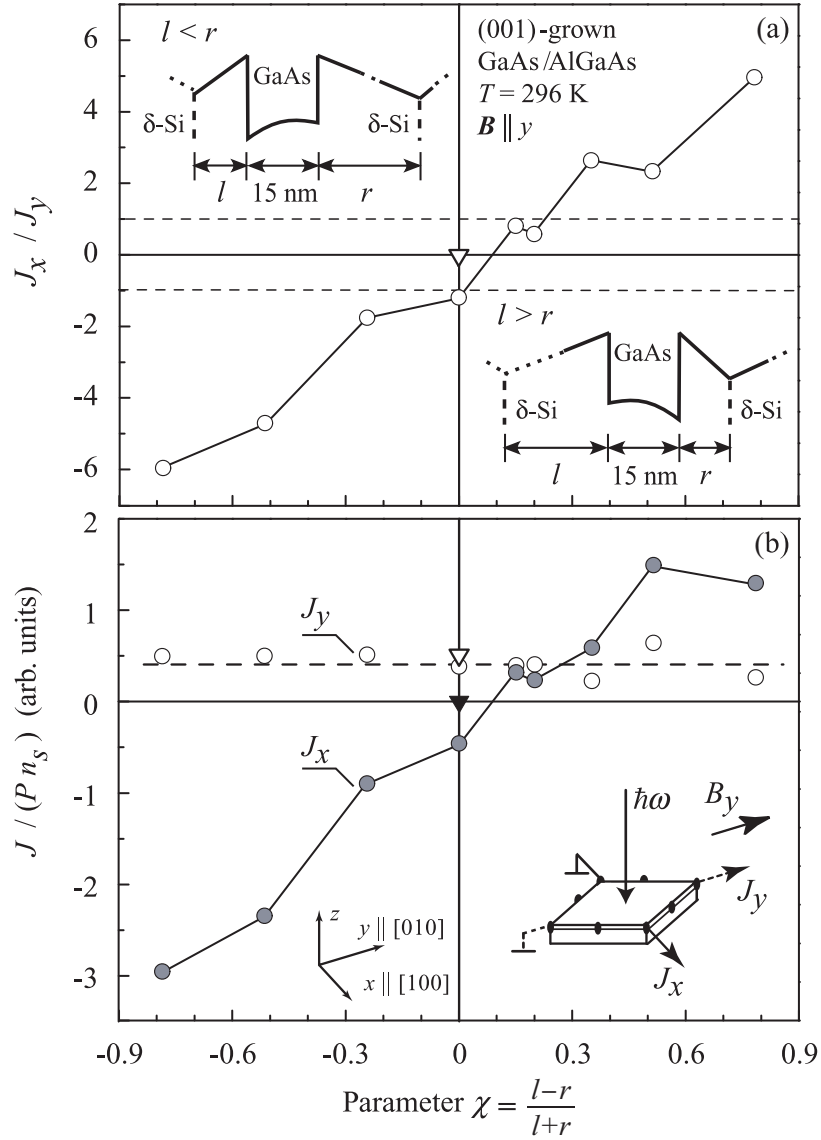


**Figure 27:** (a) Ratio of the SIA- and BIA-induced contributions to the MPGE,  $J_x/J_y$ , as a function of  $\chi$ . The triangle shows the result for sample 5LT, grown at  $T_\delta = 490^\circ\text{C}$ , the circles demonstrate the data for all other samples grown at  $T_\delta \approx 630^\circ\text{C}$ . Insets: QW profile and doping positions for  $l < r$ ,  $l > r$ . (b) Dependence of  $J/Pn_s$  on the parameter  $\chi$ . The photocurrents are measured along and normal to  $\mathbf{B} \parallel y$ . Full and open symbols show  $J_x$  and  $J_y$ , respectively (triangles are the data for sample 5LT). Inset: experimental geometry.

$J_y$  were measured either parallel or perpendicularly to  $\mathbf{B}$ , as sketched in the inset of Fig. 27(b), via the voltage drop across a  $50 \Omega$  load resistor [7].

Under THz irradiation a photocurrent signal was observed, which rises linearly with increasing magnetic field strength and changes its sign upon the inversion of the magnetic field direction from  $B_+ > 0$  to  $B_- < 0$ . Furthermore, the signal's temporal behavior follows the shape of the exciting laser pulse, ensuring the involvement of fast relaxation processes in the current formation. These two features demonstrate the typical MPGE behavior. For convenience in the discussion below, the data are evaluated calculating:

$$J = \frac{J(B_+) - J(B_-)}{2}, \quad (53)$$

which yields solely the MPGE contribution and eliminates parasitic currents.

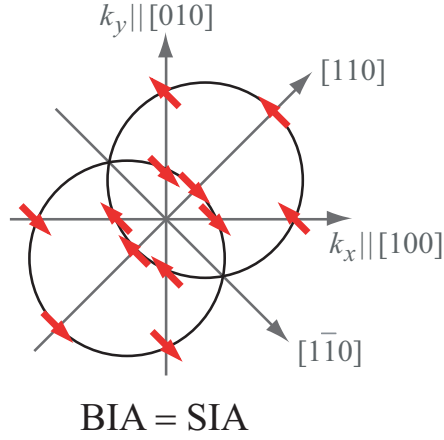
In Figure 27(a) the ratio of the photocurrents  $J_x$  and  $J_y$  is plotted as a function of the parameter  $\chi$ , hereby the magnetic field ( $B = \pm 1$  T) was applied along the  $y$ -direction. As earlier addressed, this quotient yields a direct access to the relative strengths of SIA and BIA. Important results, illustrated in Fig. 27(a), are the strong dependence of the SIA/BIA-ratio on the doping position and its change in sign at  $\chi \approx 0.1$ .

Figure 27(b) depicts the dependence of each individual current  $J_x$  and  $J_y$  on the parameter  $\chi$ . Here, the data are normalized on the free carrier concentration  $n_s$  to enable the comparison of BIA and SIA in different samples. This is reasonable, since the MPGE current is proportional to  $n_s$  but independent of the electron mobility for the Boltzmann distribution of carriers at room temperature [51]. It is clearly visible in Fig. 27(b) that the longitudinal current  $J_y$  is almost independent of  $\chi$ , while the transverse current  $J_x$  strongly depends on this parameter. These results are in full agreement with Eqs. (52), which indicate for this experimental geometry that the longitudinal current originates solely from BIA, whereas the transverse current is just SIA-induced. In additional experiments, the  $\mathbf{B}$ -field was applied along the  $x$ -axis. As a result, the longitudinal photocurrent inverted its sign in all samples, while the data on the transverse current remained the same. This observation also accords with Eq. (49), which yields for  $\mathbf{B} \parallel x$  that the photocurrent is given by  $j_x = -\gamma^{\text{BIA}} B_x |\mathbf{E}|^2$  and  $j_y = \gamma^{\text{SIA}} B_x |\mathbf{E}|^2$ .

## 4.2 Discussion

The behavior of the longitudinal current, which for both experimental geometries does not depend on  $\chi$ , is typical for BIA-induced effects, since they are evidently not influenced by the magnitude and sign of  $\chi$ . By contrast, the transverse current results from SIA and, thus, strongly relies on the impurity potential. Through a variation of  $\chi$ , the degree of asymmetry is controlled and even the sign of the SIA-induced transverse photocurrent gets inverted at  $\chi \approx 0.1$ . The obtained results [7] depict that the asymmetry is dominated for  $\chi < 0.1$  by the potential of impurities placed on the QW's substrate (left) side. Figure 27(b) shows that (001)-oriented samples must be asymmetrically doped, so that the  $\delta$ -doping layer on the substrate side is placed at a larger distance than that to the right side of the QW ( $l > r$ ), to exhibit a vanishing SIA. This result emerges due to the segregation of Si-impurities during the molecular beam epitaxial growth. By contrast, SIA is absent in symmetrically doped (110)-grown QWs [12]. This essential difference is a consequence of the growth conditions. Actually, the typical growth temperatures of high-quality (001)-oriented QWs lie above 600°C, whereas (110)-structures are grown at 480°C [93]. The high growth temperatures lead to a substantial dopant migration along  $z$  during the growth process (segregation), which affects mostly the substrate side of a QW and yields SIA in symmetrically doped (001)-oriented QWs. To suppress the segregation a symmetrically doped sample was produced, where the temperature during the growth of the  $\delta$ -doping and subsequent layers was reduced to  $T_\delta = 490^\circ\text{C}$  (sample 5LT). In this case, for the solely SIA-induced MPGE current perpendicular to  $\mathbf{B}$ , an almost vanishing signal was measured. By contrast, the MPGE due to BIA is not influenced. This result convincingly demonstrates that due to the reduced growth temperature the segregation is suppressed and the additional structure inversion asymmetry is no longer introduced.

A further important observation is the following: Figure 27(a) shows for  $\chi = 0$  (sample 4) and  $\chi \approx 0.17$  (samples 6 and 7) that  $|J_x/J_y| \approx 1$ , which indicates equal strengths of SIA and BIA. Here, the  $\mathbf{k}$ -linear Rashba and Dresselhaus terms are of equal strengths:  $|\alpha| = |\beta|$ . If this condition is fulfilled, the spin is a good quantum number and a special case of spin splitting results. Under



**Figure 28:** Distribution of spin orientations for the 2D Fermi energy, indicating the spin helix condition (equal strength of BIA- and SIA-induced  $\mathbf{k}$ -linear terms), in a structure with  $C_{2v}$  symmetry.

these circumstances, both effective magnetic fields caused by the Rashba and Dresselhaus SOI get aligned along one common axis. This leads to some very interesting features: A strong anisotropy in spin-splitting arises, where the splitting in the  $\mathbf{k}$ -space vanishes along the  $[1\bar{1}0]$  direction and gets maximal for the  $[110]$  direction, or vice versa depending on the relative signs of  $\alpha$  and  $\beta$  [33, 35]. Additionally all spins are oriented parallel to the  $\mathbf{k}$ -direction with zero spin-splitting. Thus, for a spin aligned in this direction, the D'yakonov-Perel spin relaxation (see Section 2.3) is suppressed [14, 60], yielding very long spin relaxation times. Therefore, such a material is a very promising candidate for spintronic devices as for instance a spin transistor [94]. Furthermore, if the spin has an arbitrary orientation, it precesses only around one specific crystal axis for each possible electron momentum  $\mathbf{k}$  and spatially periodic modes emerge. This results in the formation of a persistent spin helix [16, 95, 96], which is robust against all forms of spin-independent scattering. Hence, the persistent spin helix condition is fulfilled, if the strengths of the  $\mathbf{k}$ -linear Rashba and Dresselhaus terms are equal. Figure 28 demonstrates the spin orientation as it appears in the persistent spin helix state. Here the anisotropy in spin splitting is obvious: in the  $[1\bar{1}0]$  direction it vanishes, while the  $[110]$  direction is characterized by a maximum splitting. Moreover, all spins are oriented along

the  $[1\bar{1}0]$  direction, this can be described with an effective magnetic field, which for each wavevector  $\mathbf{k}$  points along  $[1\bar{1}0]$ .

The large spin-splitting anisotropy is also visible in the photocurrent measured perpendicularly to a  $\mathbf{B}$ -field applied along one of the axes  $\langle 110 \rangle$ . For this current the phenomenological theory yields  $j_{\perp} = (\gamma^{\text{SIA}} \pm \gamma^{\text{BIA}})B|\mathbf{E}|^2$ , where the two signs correspond to the two magnetic field orientations. Especially for  $\gamma^{\text{SIA}} \approx \gamma^{\text{BIA}}$  substantial differences in the transverse photocurrents, for  $\mathbf{B}$  applied along the  $[1\bar{1}0]$  or  $[110]$  direction, are expected. Indeed, results proving this anisotropy were obtained for instance in sample 4, which is characterized by very similar strengths of SIA and BIA. Here, the transverse signal changes its magnitude by a factor of six under the rotation of an in-plane magnetic field  $\mathbf{B}$  by 90 degrees.

### 4.3 Summary

In this chapter, it was demonstrated that the MPGE due to unpolarized radiation is an appropriate tool, to study SIA and BIA in (001)-oriented Si- $\delta$ -doped GaAs/AlGaAs QWs at room temperature. Utilizing the MPGE, a set of samples was investigated, where the individual samples differ essentially in the doping profile but have the same QW width. The doping profile was varied by choosing different  $\delta$ -doping positions, indicated by  $\chi$ , for each sample. In the experiment, the MPGE current, resulting from unpolarized radiation and a  $\mathbf{B}$ -field applied along a cubic axis ( $[001]$  or  $[010]$ ), was analyzed. The signals, measured along the in-plane magnetic field, reflect BIA, while a current, picked up perpendicularly to  $\mathbf{B}$ , is SIA-induced. Using this, the SIA/BIA-ratio could be estimated, as well as its behavior on a variation of  $\chi$  investigated. Hereby, a strong, almost linear, dependence of this ratio on the shift of the doping position was observed. This demonstrates that the impurity position plays an important role for SIA. Furthermore, the behavior of both individual currents, SIA- and BIA-induced, on  $\chi$  was examined. At that, we obtained that BIA is not influenced by the doping position, whereas SIA strongly depends on it. Additionally, the zero point of the SIA-related current is shifted to  $\chi \approx 0.1$ , which is caused by the segregation of dopant atoms. Thus, we verified that the high growth temperatures of high-quality (001)-oriented GaAs QWs lead

to segregation, adding an additional contribution to SIA. This is in contrast to (110)-oriented structures, which are grown at much lower temperatures. To further explore the role of the segregation, a symmetrically doped (001)-oriented sample was prepared, where the temperature during the growth of the  $\delta$ -doping layer,  $T_\delta$ , was substantially reduced (from above 600 to 490°C). Here, the MPGE current based on SIA vanishes, while the BIA-related current remained the same. This proves that the segregation is suppressed by the lower temperature  $T_\delta$ . Another important fact is, that the here presented method, to study SIA and BIA via the MPGE, works even at room temperature, where many other methods fail. With this work [7], we obtained QWs with a vanishing SIA (through suppression or compensation of the segregation) as well as QW structures, exhibiting almost equal strengths of  $\mathbf{k}$ -linear Rashba and Dresselhaus spin-splittings, and consequently equal SIA and BIA. These QWs should allow the formation of a persistent spin helix and exhibit extraordinarily long spin relaxation times. In the next chapter, photogalvanic effects are used to investigate bulk and structure inversion asymmetry in InGaAs QWs, which are characterized by a strong SOI.

## 5 Study of BIA and SIA in InGaAs quantum wells

As explained previously in the introduction of Chapter 4, SIA and BIA are key material properties regarding spintronic devices, since they lead to the Rashba and Dresselhaus terms, respectively. The magnitude  $\alpha$  of the  $\mathbf{k}$ -linear Rashba term can be easily controlled by an external gate voltage, applied along the growth direction. The Dresselhaus term leads to a band spin splitting, described by terms linear and cubic in the momentum  $\mathbf{k}$ . Its strength  $\beta = \gamma \langle k_z^2 \rangle$  (where  $\gamma$  is a material parameter) can hardly be changed, since the Dresselhaus terms originate from crystal fields. These spin-orbit terms are, as already discussed in Chapter 2.1.3, described by the Hamiltonian  $H_{\text{SO}} = H_{\text{R}} + H_{\text{D}}$ , with following Rashba and Dresselhaus terms [1, 13]:

$$H_{\text{R}} = \alpha(k_y\sigma_x - k_x\sigma_y), \quad (54)$$

$$H_{\text{D}} = \beta(k_x\sigma_x - k_y\sigma_y) + \gamma(-\sigma_x k_x k_y^2 + \sigma_y k_y k_x^2). \quad (55)$$

The capability, to control the spin-splitting and, thus, spin states all electrically in gated semiconductor heterostructures [8, 9], is a basic requirement for future spintronic devices. A major challenge regarding such elements, consists in the suppression of the spin relaxation in materials possessing a strong, tunable SOI. One possible approach, to solve this problem, lies in a proper choice of the strengths of  $\alpha$  and  $\beta$ . Hereby, a special situation results, if the  $\mathbf{k}$ -cubic terms can be neglected and BIA and SIA exhibit equal strengths: Then,  $\alpha = \pm\beta$  holds and the spin relaxation is suppressed [14, 15]. In this unique symmetry, a collinear alignment of Dresselhaus and Rashba effective magnetic fields emerges (see Section 4.2). Thus, all spins precess around one fixed axis, which yields spatially periodic modes [15], called persistent spin helix (PSH) [16]. The PSH is robust against all forms of spin-independent scattering. This leads to an advantageous situation: On the one hand, the spin relaxation is suppressed, while, on the other hand, the spin degree of freedom can still be controlled by a gate voltage. Hereby, diverse theoretical proposals for future spintronic applications arise [15, 17, 18], which use the tuneability of  $\alpha$  via a gate voltage, to reach  $\alpha = \beta$ .

The existence of a persistent spin helix was experimentally detected in ungated GaAs/AlGaAs QWs, employing spin-grating spectroscopy [96]. In these GaAs heterostructures, just a weak cubic SOI exists that barely affects the PSH formation. Hence, the important question arises, if a PSH type state remains in materials with a strong SOI, where  $\mathbf{k}$ -cubic terms contribute stronger, as e.g. InGaAs QWs. Furthermore, much less is known theoretically [75,95,97,98], concerning the robustness of the PSH in this general case.

Therefore, in this chapter, SIA and BIA will be investigated in sample set III containing InGaAs/InAlAs QW structures. The QW width of 4 nm was chosen, since here  $\alpha = \beta$  was predicted. Additionally, a sample with  $L_{\text{QW}} = 7$  nm was investigated. To get independent information on the  $\alpha/\beta$ -ratios, two complementary measurements were performed on the same samples. First, the two photogalvanic effects, CPGE and SGE, are used to estimate the  $\alpha/\beta$ -ratio [52, 53] in strain-free ungated samples. These photocurrents are insensitive to  $\mathbf{k}$ -cubic spin-orbit terms and therefore can be used to detect the PSH state, where the strengths of the  $\mathbf{k}$ -linear terms  $\alpha$  and  $\beta$  are equal. Second, complementary magneto-transport measurements are performed on gated samples. Here, quantum corrections to the magneto-conductance are considered to detect a PSH type state [75, 99–101]: Generally, the presence of Rashba and Dresselhaus terms leads to spin randomization and thereby, to weak antilocalization (WAL). In the special case of a persistent spin helix, the spins are not rotated along closed backscattered trajectories and therefore, weak localization (WL) should result. Whereas WAL is reflected in an increased conductance, WL results in a decrease of conductivity, due to interference. In the experiment, the magneto-conductance was measured, while the Rashba SOI strength was tuned by an electrical gate. Hereby, a crossover from weak antilocalization to weak localization and back is monitored. The emergence of the WL reflects a PSH type state, even in the presence of the  $\mathbf{k}$ -cubic SOI. In the discussion, the experiments are compared and information on the role of the  $\mathbf{k}$ -cubic terms is extracted. A corresponding theoretical and numerical analysis illustrates that a PSH type state prevails in the 4 nm broad InGaAs QW. However, no longer at  $\alpha = \beta$ , even if  $\beta$  is renormalized by the  $\mathbf{k}$ -cubic terms. Finally, a summary follows.

## 5.1 Photocurrent measurements

### 5.1.1 Experimental results

The opto-electronic experiments are carried out on sample set III, consisting of ungated, strain-free (001)-grown  $\text{In}_{0.53}\text{Ga}_{0.47}\text{As}/\text{In}_{0.52}\text{Al}_{0.48}\text{As}$  QWs with well widths of 4 and 7 nm. Hereby, the photocurrent is measured in all samples at room and liquid helium temperature under excitation with terahertz (THz) laser radiation. As radiation source, an optically pumped  $\text{NH}_3$  molecular laser [32, 102] was used. It was tuned to different wavelengths: 90, 148 and  $280\ \mu\text{m}$  to cause indirect transitions within the lowest conduction subband. The corresponding photon energies are 13.8, 8.4 and 4.4 meV, respectively, much smaller than the energy gap and subband separation. The  $\text{NH}_3$  laser provided single pulses exhibiting a pulse duration of about 100 ns and a peak power  $P$  of about 6 to 12 kW. To obtain elliptically and in particular circularly polarized radiation, a  $\lambda/4$  plate is used. The angle  $\varphi$  denotes the rotation angle of the wave plate, indicating the helicity of light (for details see Section 3.2). The resulting photocurrents are measured in all samples, via the voltage drop across a load resistor.

*5.1.1.1 Circular photogalvanic effect:* In the measurements concerning the CPGE [63] (see Section 2.2.3) oblique incidence of radiation along the  $x$  axis is required, as illustrated in the inset of Fig. 29. Here, sample (i) is illuminated at an angle of incidence of  $\phi_0 = 30^\circ$  and the resulting currents are measured parallel and perpendicularly to  $\hat{e}_x$ . In Figure 29 the helicity dependences of these photocurrents  $J_x$  and  $J_y$  are illustrated, resulting from the rotation of a  $\lambda/4$  plate. It clearly demonstrates the fingerprint of the CPGE, which is the current's sign inversion upon switching the radiation's helicity  $P_{\text{circ}}$  from  $+1$  to  $-1$  at  $\varphi = 45^\circ$  ( $\sigma^+$ ) and  $\varphi = 135^\circ$  ( $\sigma^-$ ), respectively. Additionally, it was verified that the current vanishes for normal incidence of radiation and reverses its sign upon an inversion of the angle of incidence. These features prove that the current results from the CPGE. The whole polarization dependence results from the interplay between CPGE and linear photogalvanic effect (LPGE). Using the Stokes parameters, it can be well fitted by  $J(\varphi) = AP_{\text{circ}} + B \cos^2 2\varphi +$

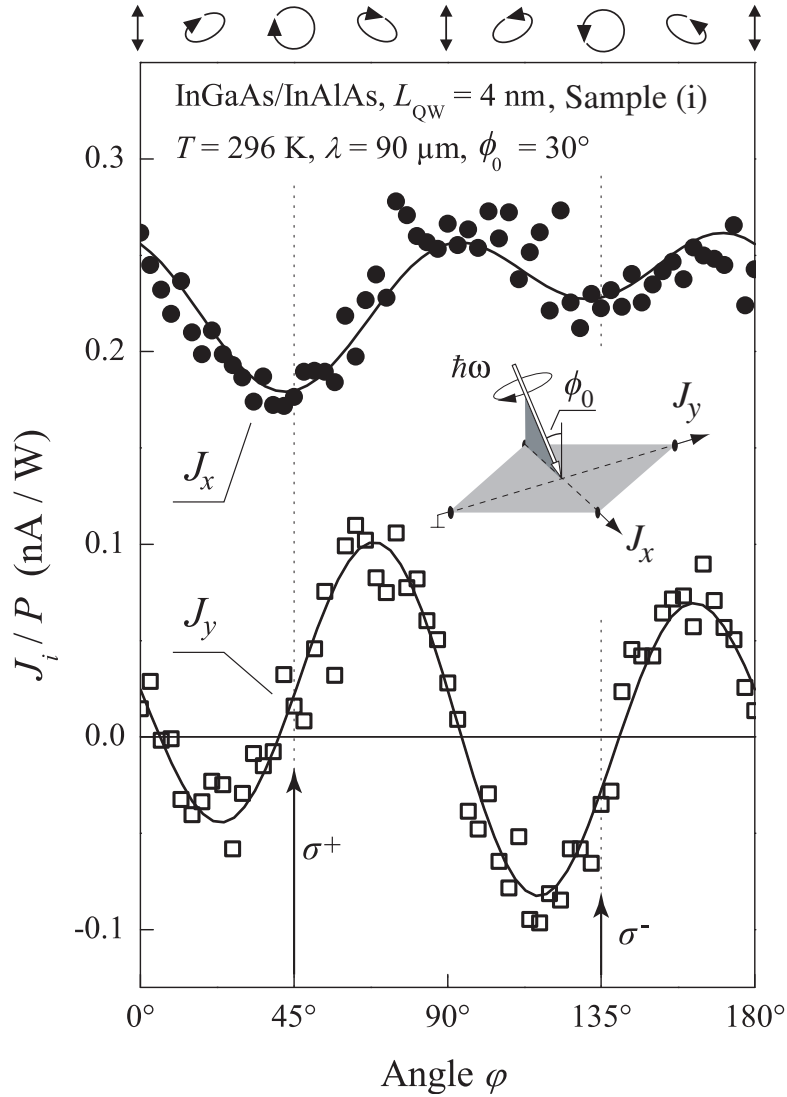


**Figure 29:** Helicity dependences of the longitudinal ( $J_x$ ) and transverse ( $J_y$ ) photocurrents obtained for sample (i) at room temperature,  $\phi_0 = 30^\circ$  and a photon energy of  $\hbar\omega = 13.8 \text{ meV}$ . The ellipses on top illustrate the polarization states for various angles of the  $\lambda/4$  plate,  $\varphi$ . Inset: Experimental geometry for the CPGE.

$C \sin 4\varphi + D$ . Here the first term, which is proportional to the helicity and contains the parameter  $A$ , originates from the CPGE. The other three terms, including the coefficients  $B$ ,  $C$  and  $D$ , are caused by the linear photogalvanic effect (LPGE) and insensitive to the helicity. For the further data analysis, the

pure CPGE was extracted from the helicity dependence of the total current, herewith, any spurious currents are avoided as well. In the separation, the CPGE's sign inversion under the transition from  $\sigma^+$  to  $\sigma^-$  polarized light was used and the circular photocurrent results after:

$$J^{\text{CPGE}} = [J(\sigma^+) - J(\sigma^-)]/2, \quad (56)$$

where  $J(\sigma^+)$  and  $J(\sigma^-)$  are photocurrents measured at  $\sigma^+$ - and  $\sigma^-$ -polarized excitation.

In Section 2.2 it was already demonstrated that the Rashba and Dresselhaus spin-splittings can be estimated via photocurrent measurements. With the above described setup, the splitting strengths  $\alpha$  and  $\tilde{\beta}$  can be obtained via the CPGE currents  $J_y^{\text{CPGE}}$  and  $J_x^{\text{CPGE}}$ . Here, the Dresselhaus coefficient  $\tilde{\beta}$  indicates that the photocurrent measurements are sensitive to the renormalized Dresselhaus terms, i.e. to the first angular harmonics. After Eq. (31), for  $\hat{e} \parallel x$ , the ratio  $\alpha/\tilde{\beta}$  is given by:

$$\left| \frac{\alpha}{\tilde{\beta}} \right| = \left| \frac{J_y^{\text{CPGE}}}{J_x^{\text{CPGE}}} \right|. \quad (57)$$

With Eq. (57), from Fig. 29 results a  $\alpha/\tilde{\beta}$ -ratio of  $1.03 \pm 0.08$  for sample (i) at room temperature. This experiment was also carried out at 5 K, yielding a slightly increased value of  $\alpha/\tilde{\beta} = 1.16 \pm 0.09$ .

To improve the accuracy, the CPGE was additionally analyzed using the larger sample geometry with 8 contact pairs, which are equally arranged on a circle of 8 mm diameter. It allows to probe the photocurrents along several different directions in addition to  $x$  and  $y$ . Sample (ii) ( $L_{\text{QW}} = 4$  nm) was as well illuminated along the  $x$  direction under oblique incidence ( $\phi_0 = 25^\circ$ ). The helicity dependences were measured one-by-one from opposite contact pairs and show the same features as Fig. 29, discussed above. From these dependences, the pure CPGE contributions were extracted, using Eq. (56). The resulting currents  $J^{\text{CPGE}}(\theta)$  are plotted in polar coordinates in Figure 30, where the angle  $\theta$  defines the current's direction and lies between  $x \parallel [100]$  and  $J$ . The current component,  $J_{\text{R}}$ , perpendicular to  $\hat{e}_x$  is driven by the Rashba spin splitting,

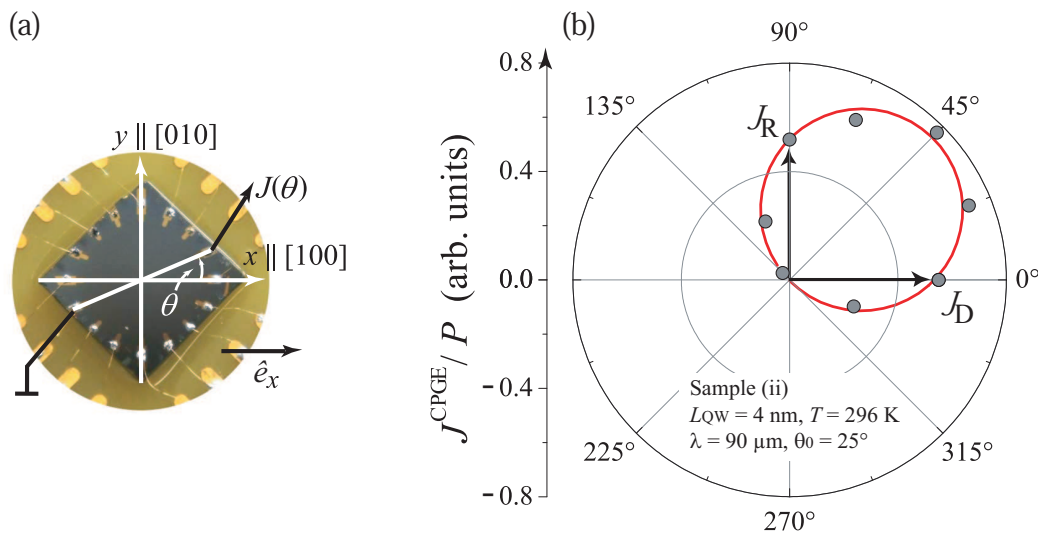


**Figure 30:** (a) Illustration of the larger sample with 16 contacts and definition of the azimuthal angle  $\theta$ . (b) Polar plot of the pure CPGE current  $J^{\text{CPGE}}(\theta)$ , which is extracted from helicity dependences measured in sample (ii). The solid line represents the fit after Eq. (58) with an Rashba/Dresselhaus ratio of  $J_R/J_D = 0.94 \pm 0.08$ .

whereas the parallel component,  $J_D$ , is caused by the Dresselhaus SOI. The data presented in Fig. 30(b) can be well fitted by:

$$J^{\text{CPGE}}(\theta) = J_D^{\text{CPGE}} \cos\theta + J_R^{\text{CPGE}} \sin\theta, \quad (58)$$

with  $J_R^{\text{CPGE}}/J_D^{\text{CPGE}} = 0.94 \pm 0.08$ . This ratio is related to the Rashba/Dresselhaus-ratio,  $\alpha/\tilde{\beta} = J_R^{\text{CPGE}}/J_D^{\text{CPGE}}$ . According to this fit, the measured current for an arbitrary angle  $\theta$  can be described as a linear combination of Rashba-induced *and* Dresselhaus-induced components. The only exceptions are at  $\theta = 0^\circ$  and  $\theta = 90^\circ$ , here, the currents reflect the pure Dresselhaus and pure Rashba term, respectively. Hence, the current emerging at  $\theta = 45^\circ$  reflects  $\alpha + \tilde{\beta}$  (where both coefficients are assumed to have the same sign), while for  $\theta = 135^\circ$ , it is proportional to  $\alpha - \tilde{\beta}$ . The circular fit, with the maximum current amplitude at about  $45^\circ$  proves the equal strengths of Rashba and Dresselhaus spin splittings in the 4 nm broad QW.

*5.1.1.2 Spin-galvanic effect:* Additionally to the CPGE, also the SGE [59] (see Section 2.2.2) was used to study the InGaAs/InAlAs heterostructures. In these measurements, normal incidence of radiation and an external in-plane magnetic field of up to  $\mathbf{B} = \pm 1$  T, applied along the  $x$  axis, are required, as illustrated in the inset of Fig. 31. Using this setup, the SGE current was measured on sample (i) under irradiation at a wavelength of 148  $\mu\text{m}$ . The resulting currents were measured along ( $J_x$ ) and perpendicularly ( $J_y$ ) to the magnetic field. These currents  $J_x$  and  $J_y$  depend linearly on  $B$ , which is, for the weak magnetic field strengths used here, a typical feature of the SGE. Furthermore, the signals vanish at  $\mathbf{B} = 0$ . To avoid any spurious magnetic field independent contributions, the signals are again treated after Eq. (53).

In Figure 31 the helicity dependences of the photocurrents  $J_x$  and  $J_y$ , treated after Eq. (53), are illustrated. The whole polarization dependence results from the interplay between SGE and MPGE. After the phenomenological theory [58] the photocurrents can be well fitted by:

$$J(\varphi) = J^{\text{SGE}} \sin 2\varphi + J^{\text{d}} \sin 4\varphi - J^{\text{e}} \cos^2 2\varphi + J^{\text{f}}, \quad (59)$$

This polarization dependence, described by the Stokes parameters, as well as the linear coupling of all individual contributions to the magnetic field  $\mathbf{B}$  prove that the signals are due to the magnetic field induced photogalvanic effects [58]. Here the first term, which is proportional to the helicity and contains the parameter  $J^{\text{SGE}}$ , originates from the SGE. The other three terms, including the coefficients  $J^{\text{d}}$ ,  $J^{\text{e}}$  and  $J^{\text{f}}$ , are caused by the linear MPGE and therefore insensitive to the helicity.

Analogous to the previously discussed examination of the CPGE, the pure SGE was extracted from the helicity dependence of the total current. Herewith, any spurious currents are avoided as well. In the separation, the SGE's sign inversion under the transition from  $\sigma^+$  to  $\sigma^-$  polarized light was used and the circular photocurrent results after:

$$J^{\text{SGE}} = \frac{J(\sigma^+) - J(\sigma^-)}{2}. \quad (60)$$

In Section 2.2 it was already demonstrated that the Rashba and Dresselhaus spin-splittings can be estimated via photocurrent measurements. With the

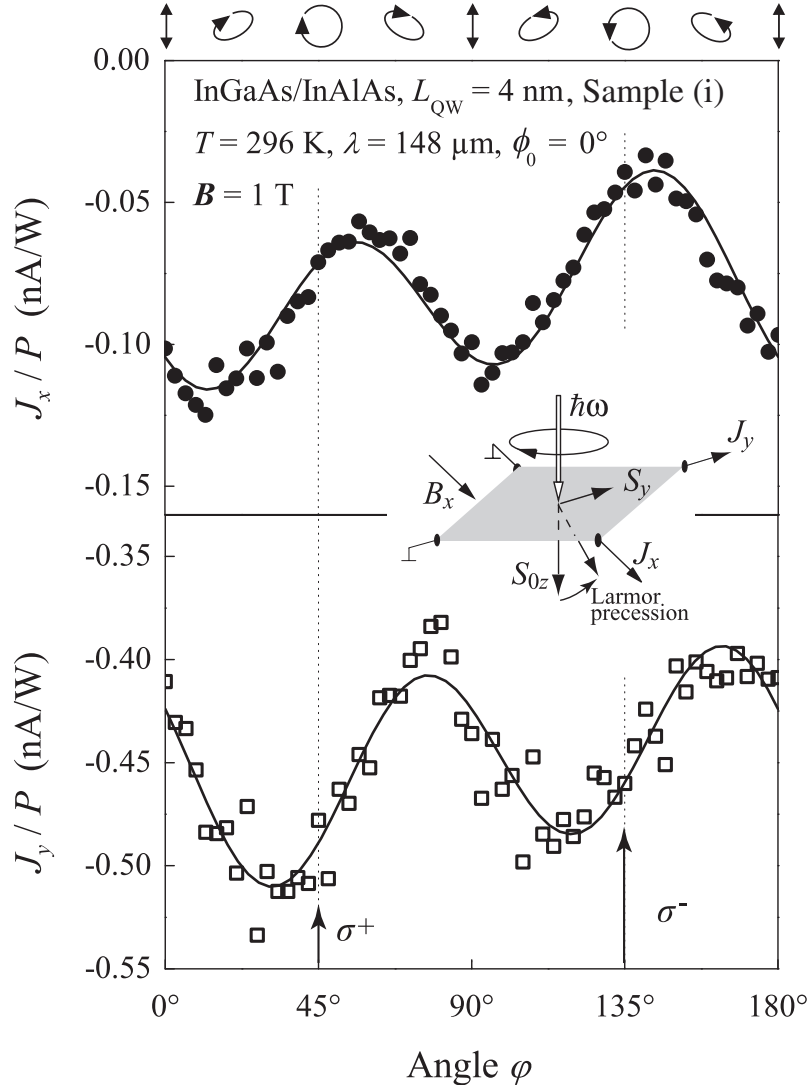


**Figure 31:** Helicity dependences of the magnetic field induced photocurrents  $J_x$  and  $J_y$  obtained for sample (i) at room temperature,  $B_x = \pm 1$  T and a photon energy of  $\hbar\omega = 8.4$  meV. The ellipses on top illustrate the polarization states for various angles  $\varphi$  of the  $\lambda/4$  plate. Inset: Experimental geometry for the SGE.

above described setup, the splitting strengths  $\alpha$  and  $\tilde{\beta}$  can also be obtained via the SGE currents  $J_x^{\text{SGE}}$  and  $J_y^{\text{SGE}}$ . After Eq. (27), for  $\mathbf{B} \parallel x$  and consequently  $\mathbf{S} \parallel y$ , the Rashba/Dresselhaus-ratio is given by:

$$\left| \frac{\alpha}{\tilde{\beta}} \right| = \left| \frac{J_x^{\text{SGE}}}{J_y^{\text{SGE}}} \right|. \quad (61)$$

With Eq. (61), from Fig. 31 results a  $\alpha/\tilde{\beta}$ -ratio of  $0.99 \pm 0.08$  for sample (i) at room temperature. This experiment was also carried out at 5 K, yielding a slightly increased value of  $\alpha/\tilde{\beta} = 1.08 \pm 0.09$ . Note that the direction of the average non-equilibrium spin  $\mathbf{S}$  plays an important role for the estimation of the  $\alpha/\tilde{\beta}$ -ratio. In the experimental geometry used here, the Larmor precession generally should create spins oriented perpendicularly to the magnetic field  $\mathbf{B}$ . Nevertheless, a possible anisotropy of the spin relaxation due to the D'yakonov-Perel spin relaxation mechanism may affect the relative direction of  $\mathbf{B}$  and  $\mathbf{S}$  [52]. However, the fact that  $J_x^{\text{SGE}} \approx J_y^{\text{SGE}}$  indicates that the spin relaxation anisotropy is negligible in this structure and that  $\alpha/\tilde{\beta} = J_x^{\text{SGE}}/J_y^{\text{SGE}}$  is justified. In sample (iii) ( $L_{\text{QW}} = 7$  nm) the relative strengths of Rashba and Dresselhaus splittings were estimated with the same method. From the helicity dependences of the longitudinal and transverse photocurrents, measured at room temperature, the ratio was estimated to:  $\alpha/\tilde{\beta} = J_x^{\text{SGE}}/J_y^{\text{SGE}} = 3.97 \pm 0.20$ . At 5 K, a ratio of  $\alpha/\tilde{\beta} = J_x^{\text{SGE}}/J_y^{\text{SGE}} = 4.00 \pm 0.20$  results.

Analog to the earlier discussed CPGE, also the SGE was additionally analyzed using sample (ii) with 16 contacts, to improve the accuracy [13]. The magnetic field was again oriented along the  $x$  axis ( $\mathbf{B} \parallel x$ ). The helicity dependences were measured one-by-one from opposite contact pairs and show the same features as Fig. 31, discussed above. From these dependences, the pure SGE contributions were extracted, using Eq. (60). In Figure 32 the resulting currents  $J^{\text{SGE}}(\theta)$  are plotted in polar coordinates. Here the angle  $\theta$  defines the current's direction and lies between  $x \parallel [100]$  and  $J$ . The current component,  $J_{\text{D}}$ , perpendicular to the magnetic field is driven by the Dresselhaus spin splitting, whereas the parallel component,  $J_{\text{R}}$ , is caused by the Rashba SOI. The data presented in Fig. 32(b) can be well fitted by:

$$J^{\text{SGE}}(\theta) = J_{\text{R}}^{\text{SGE}} \cos\theta + J_{\text{D}}^{\text{SGE}} \sin\theta, \quad (62)$$

with  $J_{\text{R}}^{\text{SGE}}/J_{\text{D}}^{\text{SGE}} = 0.98 \pm 0.08$ . This ratio is related to the Rashba/Dresselhaus-ratio,  $\alpha/\tilde{\beta} = J_{\text{R}}^{\text{SGE}}/J_{\text{D}}^{\text{SGE}}$ . This polar plot, which is well described by the

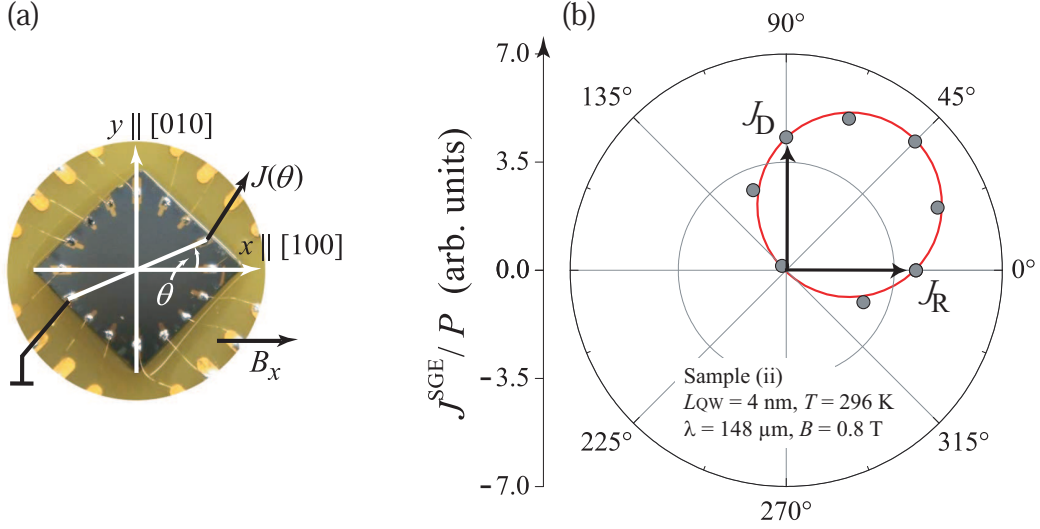


**Figure 32:** (a) Illustration of the larger sample with 16 contacts and definition of the azimuthal angle  $\theta$ . (b) Polar plot of the pure SGE current  $J^{\text{SGE}}(\theta)$ , which is extracted from helicity dependences measured in sample (ii). The solid line represents the fit after Eq. (62) with an Rashba/Dresselhaus ratio of  $J_R/J_D = 0.98 \pm 0.08$  [13].

circular fit with the maximum current amplitude at about  $45^\circ$ , is a further proof for the equal strengths of bulk and structure inversion asymmetry in the 4 nm broad QW.

### 5.1.2 Discussion

The obtained experimental results demonstrate that it is possible, to investigate BIA and SIA in InGaAs/InAlAs QWs by means of different photogalvanic effects. Since the photocurrents are just sensitive to the first angular harmonics in the Fourier expansion of the nonequilibrium electron distribution function, this method allows to investigate only the Rashba SOI and the renormalized linear in  $\mathbf{k}$  Dresselhaus SOI. The strength of the renormalized Dresselhaus contribution is given by  $\tilde{\beta}$ . This coefficient emerges, when the Dresselhaus Hamiltonian from Eq. (55) is separated into first,  $\Omega_1^{\text{D}}$ , and third order harmonics,  $\Omega_3^{\text{D}}$  (compare Section 2.1.3 and Ref. [13, 103]):

$$H_{\text{D}} = \hbar (\Omega_1^{\text{D}} + \Omega_3^{\text{D}}) \sigma, \quad (63)$$

containing renormalized linear and cubic terms:

$$\hbar\Omega_1^D = \tilde{\beta}(k_x\hat{\mathbf{x}} - k_y\hat{\mathbf{y}}); \quad \tilde{\beta} = \beta - \frac{\gamma}{4}\langle k^2 \rangle, \quad (64)$$

$$\hbar\Omega_3^D = -\frac{\gamma}{4}k^3(\hat{\mathbf{x}}\cos 3\varphi + \hat{\mathbf{y}}\sin 3\varphi). \quad (65)$$

Here,  $k_x = k\cos\varphi$ ,  $k_y = k\sin\varphi$  and  $\hat{\mathbf{x}}$ ,  $\hat{\mathbf{y}}$  are unit vectors.

In the experiments, the renormalized Rashba/Dresselhaus-ratio was estimated for liquid helium as well as room temperature in three different samples. An overview on the derived  $\mathbf{k}$ -linear  $\alpha/\tilde{\beta}$ -ratios for both QW widths is given in Table 4. It shows that all photocurrent measurements are in a good agreement. The results for the 4 nm broad QW (samples (i) and (ii)) reveal renormalized  $\mathbf{k}$ -linear Rashba and Dresselhaus spin-splittings of equal strengths ( $\alpha/\tilde{\beta} \approx 1$ ), and consequently equal magnitudes of SIA and BIA. These findings validate the provisory theoretical prediction concerning the 4 nm sample, where SIA and BIA were stated to be similar. Under these circumstances,  $\alpha = \pm\beta$  holds and both effective magnetic fields caused by the Rashba and Dresselhaus SOI get aligned along one common axis. This leads to some very interesting features: A strong anisotropy in spin-splitting arises, where the splitting in the  $\mathbf{k}$ -space vanishes along the  $[1\bar{1}0]$  direction and gets maximal for the  $[110]$  direction, or

Sample	$L_{\text{QW}}$ (nm)	Technique	$T$ (K)	$\alpha/\tilde{\beta}$
(ii)	4	CPGE	296	$0.94 \pm 0.08$
(i)			296	$1.03 \pm 0.08$
(i)			5	$1.16 \pm 0.09$
(ii)	4	SGE	296	$0.98 \pm 0.08$
(i)			296	$0.99 \pm 0.08$
(i)			5	$1.08 \pm 0.09$
(iii)	7	SGE	296	$3.97 \pm 0.20$
(iii)			5	$4.00 \pm 0.20$

**Table 4:** Obtained values for the Rashba/Dresselhaus ratio in the 4 and 7 nm broad InGaAs/InAlAs QWs. The measurements, utilizing both CPGE and SGE, were carried out for low temperature as well as for room temperature.

vice versa depending on the relative signs of  $\alpha$  and  $\beta$ . Additionally all spins are oriented parallel to the  $\mathbf{k}$  direction with zero spin-splitting. Thus, for a spin aligned in this direction, the D'yakonov-Perel spin relaxation is suppressed, yielding very long spin relaxation times. Furthermore, if a spin has another orientation, it precesses only around one specific crystal axis for each possible electron momentum  $\mathbf{k}$  and spatially periodic modes emerge. This results in the formation of a persistent spin helix, which is robust against all forms of spin-independent scattering.

Usually the Dresselhaus SOI in an InGaAs QW is much smaller than the Rashba SOI. Hence, to obtain structures that fulfill the PSH condition, the growth process has to be influenced in a way that the bulk inversion asymmetry is enhanced, while the structure inversion asymmetry is reduced. For this purpose, the following dependence of the linear Dresselhaus SOI on the QW width was used:  $\beta \sim \langle k_z^2 \rangle \sim 1/L_{\text{QW}}^2$  (see Sect. 2.1.3). Thus, the Dresselhaus SOI was increased by fabricating narrow quantum wells and the built-in Rashba SOI was reduced by symmetrical doping of the QW structure. The experimental finding, arising in the 7 nm broad QW (sample (iii)), that  $\alpha/\tilde{\beta} \approx 4$  agrees with the above consideration, since  $\beta$  decreases quadratically with increasing  $L_{\text{QW}}$  and  $\alpha$  remains unchanged, due to the same doping profiles of samples (i) and (iii). In the 7 nm broad QW the confinement gets weaker and the PSH condition breaks up.

In order to compare the photocurrent measurements with other data, the carrier densities and mobilities of the ungated InGaAs/InAlAs samples were measured as well. Therefore, the hall resistance and Shubnikov-de-Haas oscillations were investigated at 4.2 K using magnetic fields up to  $\mathbf{B} = 7$  T. The corresponding values are given in Table 3.

Moreover, in Table 4 a very weak temperature dependence of the  $\alpha/\tilde{\beta}$ -ratio is obvious: at 5 K all values, estimated using the CPGE as well as the SGE, are slightly larger than at 296 K. This very weak dependence of the SOI parameters in the investigated material is expected theoretically and can be explained: The combination of the small electron effective mass (around  $0.04 m_0$  for  $\text{In}_{0.5}\text{Ga}_{0.5}\text{As}$ ) with a high electron density ( $n_s = 4.26 \times 10^{12} \text{ cm}^{-2}$  for sample (i)) yields a Fermi energy of about 200 meV. This means that the 2D electron

gas is degenerated even at room temperature. The temperature-dependent corrections of the Rashba and Dresselhaus constants lie in the order of the ratio between thermal energy and Fermi energy. This ratio amounts to about 13 % at room temperature, which is in good agreement with the results presented in Table 4.

## 5.2 Magneto-transport measurements

### 5.2.1 Experimental results

In this section, the results obtained from the magneto-transport measurements, which were carried out in J. Nitta's group (Tohoku University, Sendai, Japan), are presented [13]. These complementary experiments provide a different approach to investigate Rashba and Dresselhaus terms in InGaAs based QWs. To ensure the comparability of these results with the ones obtained in the photocurrent experiments, pieces from the same wafers, of which samples (i), (ii) and (iii) were made, are investigated. For the transport measurements  $20\ \mu\text{m} \times 80\ \mu\text{m}$  sized Hall bar structures with an  $\text{Al}_2\text{O}_3$  gate insulator and a Cr/Au top gate were processed (see Fig. 33). In the experiments an external  $\mathbf{B}$ -field was applied perpendicularly to the QW plane and the sample was cooled to a temperature of  $T = 1.4\ \text{K}$ . Using this setup, the magneto-conductance was

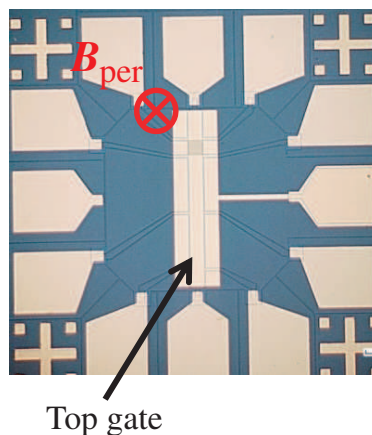


**Figure 33:** Top gate-fitted Hall bar structure ( $20\ \mu\text{m} \times 80\ \mu\text{m}$ ) and orientation of the external magnetic field.

measured at different gate voltages  $V_g$ , respectively carrier densities. Hereby,  $n_s$  was extracted from the sheet resistivity and the periodicity of the Shubnikov-de Haas oscillations, yielding  $n_s = 4.12 \times 10^{12} \text{ cm}^{-2}$  and  $n_s = 3.48 \times 10^{12} \text{ cm}^{-2}$  for the 4 nm broad and 7 nm broad QW structure, respectively, at  $V_g = 0 \text{ V}$  and  $T = 1.7 \text{ K}$ . By varying the gate voltage SIA can be tuned and thus, the Rashba/Dresselhaus-ratio. In the experiment, this ratio is accessible via the crossover from weak antilocalization to weak localization and back, which was already explained in Sect. 2.4.

Figure 34 illustrates the results from the transport measurements for both QW structures [13]. Here, the quantum correction to the magneto-transport

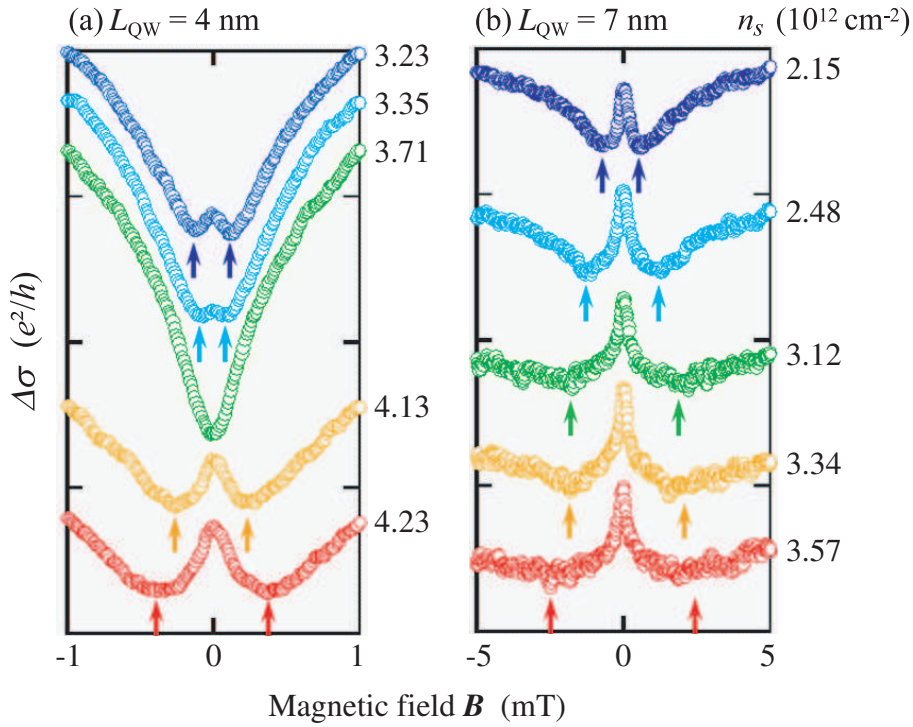


**Figure 34:** Results of the magneto-transport measurements carried out at  $T = 1.4 \text{ K}$  on both InGaAs/InAlAs samples for (a)  $L_{QW} = 4 \text{ nm}$  and (b)  $L_{QW} = 7 \text{ nm}$ . The conductance, given in units of  $e^2/h$ , is displayed as a function of the external  $B$ -field. Different curves correspond to different gate voltages, respectively, carrier densities. The arrows indicate the conductance minima of the WAL curves.

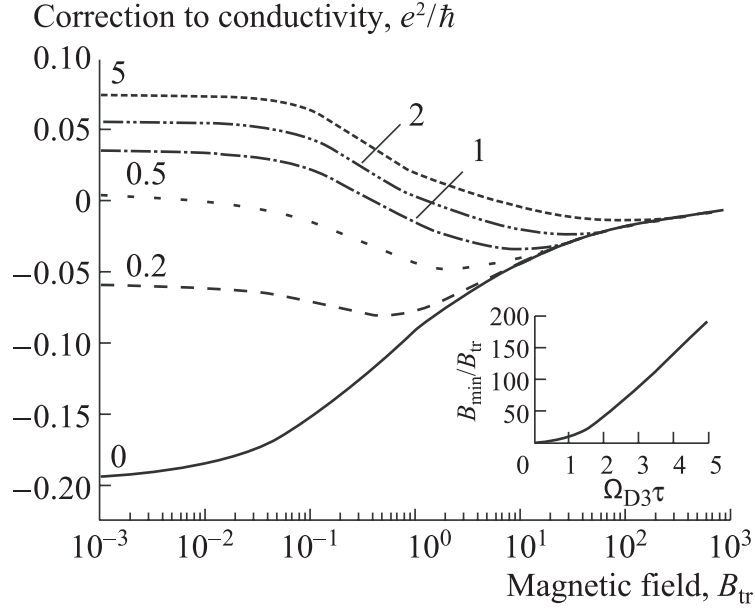
was investigated under the variation of the gate voltage from  $-15.0$  V up to  $+6.5$  V, which corresponds to charge carrier densities between  $n_s = 2.15 \times 10^{12} \text{ cm}^{-2}$  and  $n_s = 4.23 \times 10^{12} \text{ cm}^{-2}$ . In both plots the arrows indicate the conductance minima in the WAL curves. For the 4 nm broad QW, see Figure 34(a), the magneto-conductance near the zero magnetic field changes from WAL to WL characteristics and back again to WAL upon increasing  $n_s$ . Such a WAL-WL-WAL transition reflects suppressed spin relaxation for the WL regime, emerging at  $n_s = 3.71 \times 10^{12} \text{ cm}^{-2}$  ( $\mu = 1.4 \times 10^4 \text{ cm}^2/(\text{Vs})$ ). This clearly indicates that - even in the presence of a strong  $\mathbf{k}$ -cubic SOI - a PSH condition is fulfilled in the WL region. By contrast, for the 7 nm broad QW, see Figure 34(b), only the WAL characteristics is observed, which gets enhanced with increasing  $n_s$ . Thus, in the 7 nm sample the difference between Rashba and Dresselhaus terms is too large, to achieve a PSH condition by gate tuning.

### 5.2.2 Discussion

For a better understanding, all results obtained by the three described independent methods (CPGE, SGE and magneto-transport experiments) will be compared and discussed. Utilizing all these methods, the Rashba/Dresselhaus-ratio was deduced by studying the anisotropies of both photocurrents as well as of the weak anti-localization. While these approaches are based on diverse phenomena, they all give the investigated ratio at almost Fermi level. This is obvious for transport measurements, but also valid for photocurrent measurements applying THz radiation with photon energies of several meV, which are much smaller than the Fermi energy. The results obtained by these three independent methods are in a good agreement. For the 7 nm broad QW all methods reveal that the Rashba and Dresselhaus terms, and consequently SIA and BIA, are not equal, which is attributed to the inverse quadratic influence of  $L_{\text{QW}}$  on  $\beta$ . Here  $\beta$  is smaller than  $\alpha$ , due to the weaker confinement, and the PSH condition is not fulfilled.

For the 4 nm broad QW, all different methods show that Rashba and Dresselhaus terms, and consequently SIA and BIA, are of equal strengths. Although, the photocurrent experiments reveal a ratio of  $\alpha/\tilde{\beta} \approx 1$ , in the ungated sample

for a wide range of temperatures, the magneto-transport measurements yield a WL for an applied gate voltage of  $V_g = -7$  V. This gate voltage corresponds to a charge carrier density of  $n_s = 3.71 \times 10^{12} \text{ cm}^{-2}$  at 1.7 K. By contrast the carrier density in the ungated sample amounts to  $n_s = 4.26 \times 10^{12} \text{ cm}^{-2}$  at 4.2 K. This small difference in  $n_s$  can be explained in the following way: The photogalvanic effects are just sensitive to the first angular harmonics ( $\propto \sin\varphi$  and  $\cos\varphi$ ) in the Fourier expansion of the nonequilibrium electron distribution function, thus, to renormalized  $\mathbf{k}$ -linear terms  $\Omega_1$ . Herewith, the strengths of the  $\mathbf{k}$ -linear Rashba term,  $\alpha$ , and the renormalized Dresselhaus constant,  $\tilde{\beta}$ , are accessible. In contrast, the transport measurements reflect first and third ( $\propto \sin 3\varphi$  and  $\cos 3\varphi$ ) angular harmonics, thus also  $\mathbf{k}$ -cubic terms. Hence, the different  $n_s$ , of the PSH type states, indicated by the photocurrent measurements and the magneto-transport experiments, can be attributed to the influence of the  $\mathbf{k}$ -cubic Dresselhaus terms on the magneto-conductance. Even

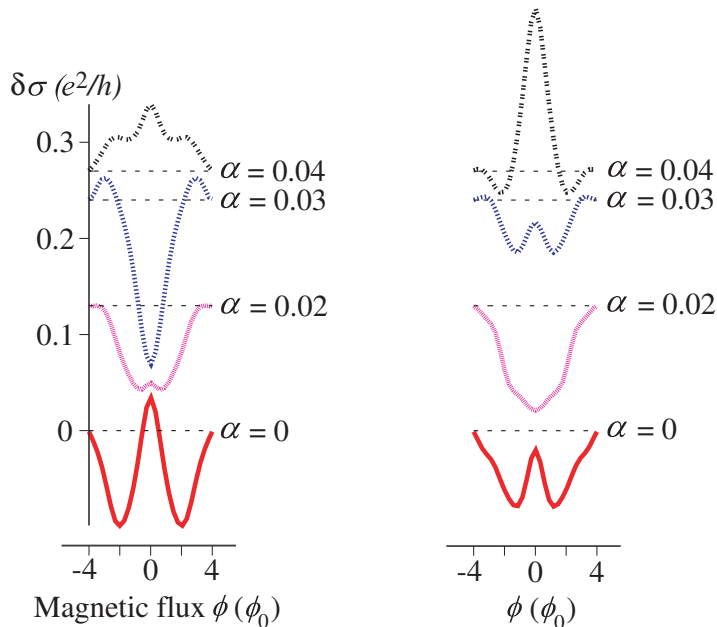


**Figure 35:** Correction to the conductivity in dependence on the magnetic field, according to Ref. [75]. The magneto-resistance is calculated for different magnitudes of the Dresselhaus component's third harmonics,  $\Omega_{D3}\tau$  (indicated by numbers near the curves). The inset gives the position of the minimum depending on  $\Omega_{D3}\tau$ .

though these  $\mathbf{k}$ -cubic terms are usually neglected, they may play an important role in the spin-relaxation and hamper the PSH formation. Especially the third harmonics may hasten the spin relaxation and, actually, prevent the PSH formation. Strictly speaking, the realization of a PSH as well as the considerable increase of the spin relaxation time and, consequently, a WAL-WL-WAL transition, can only be obtained for negligible small  $\mathbf{k}$ -cubic terms. This circumstance was already addressed 2006 by Glazov and Golub in Ref. [75]: Figure 35 shows the dependence of the magneto-resistance on  $\mathbf{B}$  for different magnitudes of the Dresselhaus component's third harmonics  $\Omega_{D3}$ . Here, for  $|\alpha| = |\beta|$  and  $\Omega_{D3} = 0$  (solid curve) a WL emerges. In contrast, due to "switching on"  $\Omega_{D3} \sim 1/\tau$  the magnetic field dependence of the conductivity is modified and now shows a WAL characteristic. Consequently, a small but non-zero contribution of the third angular harmonics causes a minimal WAL instead of a WL curve.

The influence of the  $\mathbf{k}$ -cubic Dresselhaus terms on the magneto-conductance behavior has recently been investigated in the group of K. Richter (University of Regensburg), as well [13]. Their calculations validate the results of Glazov and Golub and should also answer the remaining question: What is the general condition for the appearance of a PSH state, respectively WL, which replaces the one for the linear case (vanishing  $\mathbf{k}$ -cubic SOI),  $\alpha = \beta$ ? To answer this question, they studied the numerically computed crossover, from WAL to WL and back, in the magneto-conductance of disordered conductors under a variation of the quantities  $\alpha$ ,  $\beta$  and  $\gamma$ . In the used model, these parameters were chosen to match with the experiment and assumed to be independent, though, in a realistic system with fixed  $L_{QW}$ ,  $\beta$  and  $\gamma$  are connected. The implemented tight-binding calculations are based on an efficient recursive Green function algorithm [104] within the Landauer formalism. Hereby, a diffusive, 2D phase-coherent mesoscopic conductor with periodic boundary conditions perpendicular to the transport direction was considered. Furthermore, the full SOI Hamiltonian (Eqs. (54) and (55)) and an external perpendicular  $\mathbf{B}$ -field were employed.

Figure 36 illustrates the calculated conductance corrections  $\delta\sigma$ , depending on the magnetic flux in one unit cell  $\phi$ , for a fixed linear Dresselhaus parameter

(a)  $\beta = 0.03, \gamma = 0$       (b)  $\beta = 0.03, \gamma = 0.05$ 

**Figure 36:** Conductance corrections  $\delta\sigma$  as a function of the magnetic flux  $\phi$ , after K. Richter's group. The magneto-conductances are calculated for a fixed linear Dresselhaus parameter,  $\beta = 0.03$ , and various Rashba parameters  $\alpha$ . For (a) the  $\mathbf{k}$ -cubic Dresselhaus term  $\gamma$  is zero, in (b) a finite cubic Dresselhaus parameter of  $\gamma = 0.05$  is assumed. The different curves for  $\alpha \neq 0$  are shifted by arbitrary values for reasons of clarity.

$\beta$  and varying strengths of the Rashba SOI  $\alpha$ . In the left panel (a), the cubic Dresselhaus parameter  $\gamma$  was set to zero. As expected for the linear case, a WAL-WL-WAL crossover emerges with a pronounced WL at  $\alpha = \beta = 0.03$ , where the PSH is reflected. The conductance curves in the right panel (b) demonstrate the influence of a finite cubic Dresselhaus parameter ( $\gamma = 0.05$ ): The crossover prevails, although with less pronounced WL dip. Furthermore, the WL-like curve is shifted away from  $\alpha = \beta$ , even beyond  $\alpha = \tilde{\beta}$ . Thus, the numerical analysis indicates that the condition for the formation of a PSH, deviates from the common assumption  $\alpha = \tilde{\beta}$  [13].

For the experimental results, this means that Fig. 34(b) shows the complete crossover, from WAL to WL-like and back to WAL, upon increasing  $\alpha$ . Furthermore, the WL-like curve does *not* reflect  $\alpha = \tilde{\beta}$ . Considering this, the small difference of the carrier densities between WL-like behavior and  $\alpha = \tilde{\beta}$  in the photocurrent measurements may be caused by a weak modification of the magneto-transport results, owing to the influence of the  $\mathbf{k}$ -cubic terms.

### 5.3 Summary

In this Chapter, BIA and SIA were analyzed in Si-doped, (001)-oriented, strain-free grown InGaAs/InAlAs QWs at liquid helium and room temperature. This material was chosen, since it exhibits a strong spin-orbit interaction and, consequently, allows to investigate the influence of  $\mathbf{k}$ -cubic terms on the formation of a PSH [13]. Hereby, QW structures with two different well widths of  $L_{\text{QW}} = 4$  and 7 nm were investigated, using three independent methods based on the study of the anisotropies of CPGE, SGE and WAL. First, the two photogalvanic effects CPGE and SGE were applied, to estimate the ratio of the Rashba and renormalized  $\mathbf{k}$ -linear Dresselhaus terms,  $\alpha/\tilde{\beta}$ , in a wide range of temperatures from 5 up to 296 K. At this, the CPGE and SGE revealed for the ungated 4 nm broad QW a ratio of  $\alpha/\tilde{\beta} \approx 1$  and for the ungated 7 nm wide well a ratio of  $\alpha/\tilde{\beta} \approx 4$ . These values depend just slightly on the temperature, which agrees with the theory. Furthermore, the increased ratio of the 7 nm broad well corresponds with the  $1/L_{\text{QW}}^2$ -dependence of  $\beta$ . Thus, BIA and SIA are equal in the 4 nm sample and long spin relaxation times are expected. Second, complementary magneto-transport measurements were performed on gated samples at liquid helium temperatures. Here, quantum corrections to the magneto-conductance are investigated and the complete crossover, from WAL to WL-like and back to WAL characteristics, upon gate tuning was detected in the 4 nm broad QW. For the 7 nm sample just WAL curves were observed. Hence, it was shown that the Rashba SOI can be fine tuned by an external gate voltage. Moreover, the PSH-like state was confirmed in the 4 nm sample, while for the 7 nm sample the gate voltage was too small to reach equal Rashba and Dresselhaus terms. These results are in a good agreement with the ones obtained in the CPGE and SGE experiments. In contrast to the pho-

to currents, the magneto-transport experiments are sensitive to both first and third order harmonics in the Fourier expansion of the nonequilibrium electron distribution function. Thus, the small difference between the charge carrier densities of WL-like behavior and  $\alpha = \tilde{\beta}$  in the photocurrent measurements may be caused by a weak modification of the magneto-transport results, owing to the influence of the  $\mathbf{k}$ -cubic terms. Additionally, the influence of the third order harmonics on the PSH formation in materials with a strong SOI was considered theoretically. Moreover, via numerical simulations, the remaining question about the general condition for the formation of a PSH state was investigated. Hereby, calculations of Glazov and Golub [75] as well as evaluations of Richter's group confirm independently that the third harmonics affect the WAL-WL-WAL transition in the magneto-conductance and alter the PSH condition. Instead of a WL, a WL-like curve results in structures with a strong  $\mathbf{k}$ -cubic SOI. This WL type characteristic still reflects the PSH and reveals its robustness. The PSH even arises in structures with a substantial  $\mathbf{k}$ -cubic SOI contribution. Furthermore, the condition for the PSH formation deviates from the common assumption. It is shifted and the PSH emerges at  $\alpha \neq \pm\tilde{\beta}$ , where  $\tilde{\beta}$  gives the renormalized Dresselhaus constant [13].

## 6 Spin and orbital mechanisms of the MPGE

In the previously presented and discussed experimental results, always the photocurrents' phenomenological equations and their similarity to the  $\mathbf{k}$ -linear spin-splitting were in the focus. In this chapter, also the microscopic origins of the linear as well as the circular MPGE in GaAs/AlGaAs QWs are closer investigated. Especially the question, if a further orbital mechanism contributes in the current formation, additionally to the well known spin-based one, will be considered [21].

In diverse physical phenomena, spin and orbital mechanisms are present at the same time and result in two competitive contributions in the observable effects. Textbook examples, therefore, are the Pauli paramagnetism and the Landau diamagnetism, which cause two comparable contributions to the magnetic susceptibility of an electron gas [105]. Another bright manifestation is the fine structure of exciton lines in a magnetic field [106]. In all these phenomena, the electron systems are influenced by an external magnetic field in two different ways: via Zeeman splitting of spin sublevels and by cyclotron twisting of electron trajectories. Also in the two different roots of the magnetogyrotropic photogalvanic effect, the linear and the circular MPGE, spin and orbital mechanisms are expected in the current formation. The spin-related origins of both MPGEs have already been widely discussed and are based on the spin-dependent relaxation of a non-equilibrium electron gas in gyrotropic QW structures (for reviews see Refs. [4,5,26,32,49,54]). The microscopic mechanisms of the spin-based MPGEs are predicated on the SOI in 2DEGs with SIA and BIA. In the case of the linear MPGE, the photocurrent occurs due to electron gas heating via absorption of linearly or unpolarized radiation. The spin-dependent energy relaxation of these heated electrons leads to two oppositely directed electron flows of equal strength in the spin-up and spin-down subbands, resulting in a pure spin current [12,26,51,54,55,107]. An in-plane magnetic field induces Zeeman splitting between the spin up and spin down subbands and thus, converts the spin flow into a measurable spin-polarized electric current. The circular MPGE emerges under illumination with circularly polarized radiation and yields a helicity proportional photocurrent. It is generated by the spin-galvanic effect [59,108] (SGE), here the electric current

results due to spin-flip relaxations of a spin-polarized non-equilibrium electron gas [26, 33, 54]. The in-plane spin component, being necessary for the SGE in (001)-grown QWs is provided by an in-plane magnetic field: It rotates the optically induced spin polarization, due to the Larmor precession, into the 2DEG plane. Additionally to these intensively discussed spin-based origins of the linear and circular MPGE, orbital mechanisms in the current formation were predicted most recently [19, 20]. They are caused by a magnetic-field-induced scattering asymmetry and may contribute substantially in the current formation. This contribution may complicate the analysis of the spin currents, which are meaningful for the investigation of spin generation and spin-related transport in 2DES. These issues, in turn, are major and still growing fields in solid-state research [3, 5, 109, 110]. Furthermore, the MPGE was employed to investigate BIA and SIA [12, 52], which is in the focus of the current research and studied by various optical and transport methods [53, 73, 111–118].

In this Chapter, sample set II (GaAs/AlGaAs QWs of different width) is used to investigate the underlying mechanisms in the formation of the MPGE currents. Thus, for the first time a method is developed, which shows the orbital contribution in both, linear and circular, MPGE currents. This method is based on the different behaviors of the spin and orbital mechanism on the variation of the  $g^*$  factor: A current resulting from spin-related roots is proportional to the Zeeman splitting and hence to  $g^*$ , by contrast a current based on orbital mechanisms does not depend on  $g^*$ . Thereby, the dependence of strength and sign of the Landé factor  $g^*$  on the QW width  $L_{\text{QW}}$  in GaAs/AlGaAs structures is used. Our experiments show that, for most QW widths, both MPGEs are mainly driven by spin-related mechanisms, which results in a photocurrent proportional to the  $g^*$  factor. In structures with a vanishingly small  $g^*$  factor, however, linear and circular MPGE are also detected, proving the existence of orbital mechanisms [21]. The obtained experimental results are supported by theoretical calculations and a microscopic model for the orbital mechanism, which were developed parallel to the experimental work. Time-resolved Kerr rotation (TRKR) measurements were additionally applied to estimate the  $g^*$  factors of all samples. First, the sample characterization by photoluminescence (PL) and TRKR techniques is covered, subsequently, the analysis and discussion of the experimental results obtained by measurements of the linear and

circular MPGE will be explained and in the end of this section, a summary is given.

## 6.1 Sample characterization by PL and TRKR techniques

In this section, the experimental results concerning the sample characterization, which were obtained in the group of Ch. Schüller [21], will be introduced. Hereby the electron confinement energies in the QWs were determined by combined PL and PLE measurements; time-resolved Kerr rotation and photoluminescence techniques were used to study Landé factors and spin dynamics. Figure 37(a) shows PL and PLE spectra measured on sample E (15 nm wide

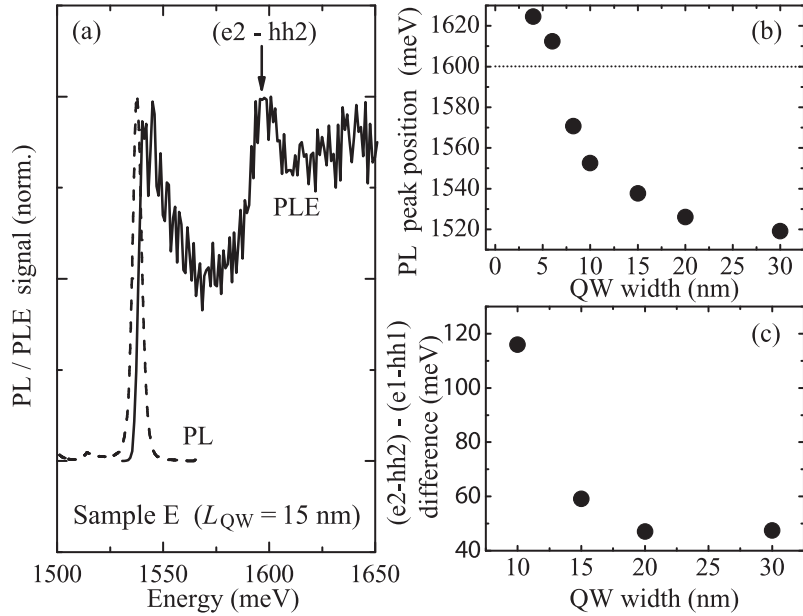


**Figure 37:** (a) PL (dashed line) and PLE (solid line) spectra of sample E (15 nm wide QW). The arrow indicates the transition energy of the  $(e2-hh2)$  transition observed in the PLE spectrum. (b) PL peak energy as a function of the QW width. The dotted line indicates the transition energy for which the electron  $g^*$  factor changes its sign [119]. (c) Energy difference between  $(e1-hh1)$  and  $(e2-hh2)$  transitions as a function of the QW width.

QW). The PL spectrum shows a single peak corresponding to the ( $e1 - hh1$ ) transition in the QW. In the PLE spectrum, the onset of absorption at the Fermi energy of the two-dimensional electron system in the QW is clearly visible slightly above this PL peak. The pronounced maximum in the PLE spectrum, indicated by the arrow, corresponds to the ( $e2 - hh2$ ) transition. Due to the increasing confinement in the narrower QWs, the PL peak position shifts to higher energies, as Fig. 37(b) demonstrates. The energy difference between ( $e1 - hh1$ ) and ( $e2 - hh2$ ) transitions as a function of the QW width, shown in Fig. 37(c), and listed in Table 2, is extracted from the PL and PLE measurements. It also increases as the QW width is reduced. For QWs, which are thinner than 10 nm, the ( $e2 - hh2$ ) transition lies outside of the tuning range of the Ti-Sapphire laser.

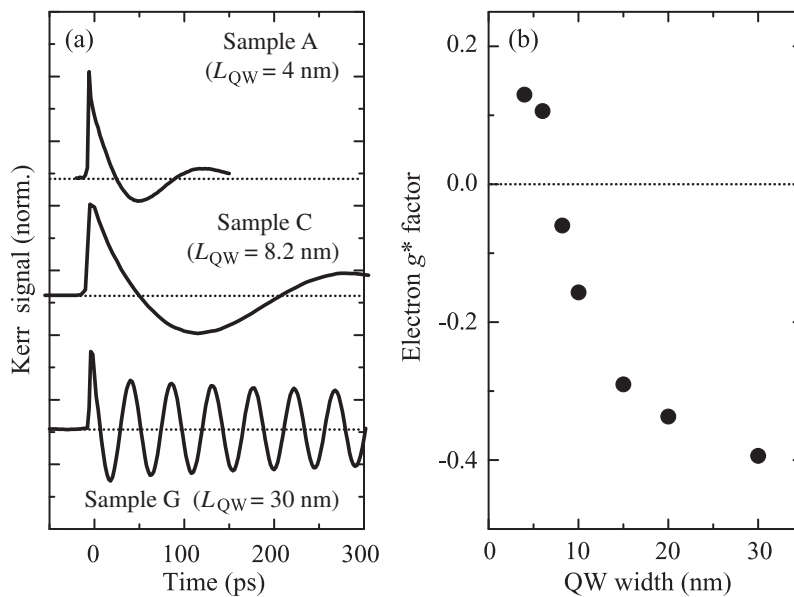


**Figure 38:** (a) TRKR traces measured on 3 different samples ( $L_{QW} = 4, 8$  and 30 nm) with an applied in-plane magnetic field of 4 Tesla. (b) Electron  $g^*$  factor as a function of the QW width extracted from the TRKR data. The sign of the  $g^*$  factor, which cannot be directly extracted from the TRKR traces, has been inferred from the PL transition energies.

It is well-established [120, 121] that in GaAs/AlGaAs QWs the electron  $g^*$  factor depends on the QW width, and even changes its sign with increasing  $L_{\text{QW}}$ . Since in narrow QWs the electron wave function has a sizeable amplitude within the AlGaAs barriers, this leads to an effective admixture of the (positive)  $g^*$  factor in the barrier material to that (negative) of the electron confined in the GaAs QW. Figure 38(a) depicts the TRKR measurements, where this width dependence is clearly observed. The TRKR traces show the damped Larmor precession of the optically oriented electron spin polarization around the applied magnetic field. The precession frequencies are markedly different: For the widest sample, the precession frequency is high, it decreases for narrower QWs, then increases again for the most narrow sample. Figure 38(b) gives the QW width dependence of the  $g^*$  factors in sample set II. The sign of the  $g^*$  factor is inferred from the PL transition energies. Hereby the zero crossing of the  $g^*$  factor is assumed, after Yugova et al. [119], for a fundamental transition energy ( $e1 - hh1$ ) of 1600 meV (indicated by the dotted line in Fig. 37(b)). In sample C, the PL peak is observed at 1572 meV, in the thinner sample B the PL peak is at 1616 meV. Hence, negative  $g^*$  factor values are assigned to the samples with nominal QW widths between 30 nm and 8.2 nm, and positive  $g^*$  factors to the two thinnest samples.

The TRKR measurements also allow the estimation of the spin dephasing time (SDT),  $T_2^*$ . Figure 39(a) shows TRKR traces measured on sample set II without applied magnetic fields. No simple correlation between the QW width and the SDT is apparent, as evidenced in Fig. 39(b) (note the logarithmic scale for the SDT). The dominant spin dephasing mechanism at low temperatures is for all samples the D'yakonov-Perel mechanism [69], thus the SDT is given by (motional narrowing regime):

$$\frac{1}{T_2^*} = \Omega^2 \tau_p, \quad (66)$$

where  $\tau_p$  is the momentum relaxation time, and  $\Omega$  the precession frequency due to the effective spin-orbit fields. With decreasing  $L_{\text{QW}}$ , the Dresselhaus field increases due to the momentum quantization along  $z$ . After Ref. [122], also the Rashba field increases monotonously with diminishing  $L_{\text{QW}}$ , in the thickness range investigated here. According to Eq. (66), the two rising spin-orbit

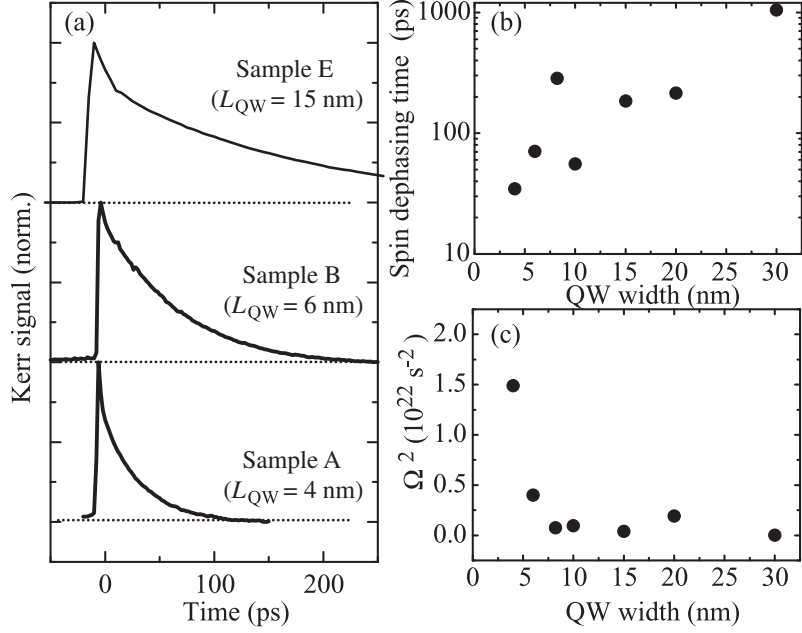


**Figure 39:** (a) Zero-field TRKR traces measured on three different samples with  $L_{\text{QW}} = 4, 6$  and  $15$  nm. (b) Zero-field SDT as a function of the QW width (log. scale). (c)  $\Omega^2$  as a function of the QW width.

fields lead to a more rapid dephasing in thinner QWs. The non monotonous dependence of the SDT on the QW width can be explained by taking into account the different momentum relaxation times in our samples. The values for  $\tau_p$  were calculated from the mobilities at 4.2 K and are listed in Table 2. They allow together with Eq. (66) to calculate  $\Omega^2$ . Figure 39(c) illustrates the results, demonstrating a near-monotonous increase of  $\Omega^2$  with decreasing  $L_{\text{QW}}$ , as expected from the QW width dependence of the effective spin-orbit fields.

## 6.2 Linear MPGE

### 6.2.1 Experimental results

The experiments concerning the linear MPGE were carried out on sample set II, which consists of GaAs/AlGaAs QWs with varying well width [21]. Hereby, the photocurrent is measured in all samples at room temperature under excitation with linearly polarized terahertz (THz) laser radiation at

normal incidence. As radiation source, an optically pumped  $\text{NH}_3$  molecular laser [32,102] was used. It was tuned to a wavelength of  $280 \mu\text{m}$  (corresponding photon energy:  $4.4 \text{ meV}$ ) to cause only free carrier absorption. The  $\text{NH}_3$  laser provided single pulses exhibiting a pulse duration of about  $100 \text{ ns}$  and a peak power  $P$  of about  $6 \text{ kW}$ . As illustrated in the inset of Figure 40, in the experiments linearly polarized radiation, with the radiation field  $\mathbf{E} \parallel x$ , and an external in-plane magnetic field  $B_y$  of  $\pm 1 \text{ T}$  were applied. The resulting linear MPGE  $J_x$  was measured along the  $x$ -direction, normally to the external in-plane magnetic field  $B_y$ . This experimental geometry ( $J_x \perp B_y$ ,  $J_x \parallel E_x$ ) is chosen to probe a current solely caused by SIA [7,52]. Thus, the influence of the QW width on the degree of asymmetry is reduced, since, for any other configuration we would also obtain a BIA-induced MPGE, which complicates the data analysis, because BIA itself strongly depends on  $L_{\text{QW}}$  [72].

Under THz irradiation a photocurrent signal  $J_x$  was observed, which increases linearly with the magnetic field strength  $B_y$  and changes its sign upon the inversion of  $\mathbf{B}$  (from  $B_+ > 0$  to  $B_- < 0$ ). This signal shows the previously described characteristics of the MPGE and was treated according Eq. (53), to eliminate spurious background processes (see Sect. 4.1).

Figure 40 displays the corresponding photocurrent  $J^{\text{LMPGE}}$  as a function of  $L_{\text{QW}}$ . Additionally, the effective Landé factor  $g^*$ , which was estimated using the TRKR experiments, is plotted for each sample (for details see Sec. 6.1). The measured  $g^*$  factors agree well with calculations obtained by Ivchenko et al. [121] given by the dashed line. It is clearly visible in Fig. 40 that the SIA-induced photocurrent  $J_x$ , similarly to the  $g^*$  factor, changes its sign upon the variation of  $L_{\text{QW}}$ . Note, that for sample A ( $L_{\text{QW}} = 4 \text{ nm}$ ),  $\chi$  is twice as large as for the other samples, therefore SIA and consequently the SIA-induced current is enhanced compared to the samples with larger  $L_{\text{QW}}$ . However, a shift between the zero points is obvious: While the  $g^*$  factor vanishes for  $L_{\text{QW}} \sim 6.5 \text{ nm}$ , the current's inversion point lies at  $L_{\text{QW}} \sim 10 \text{ nm}$ . In the discussion [21], it will be shown that this difference in the zero points as well as the linear MPGE's sign inversion can be well described by the interplay of spin and orbital mechanisms in the current formation.

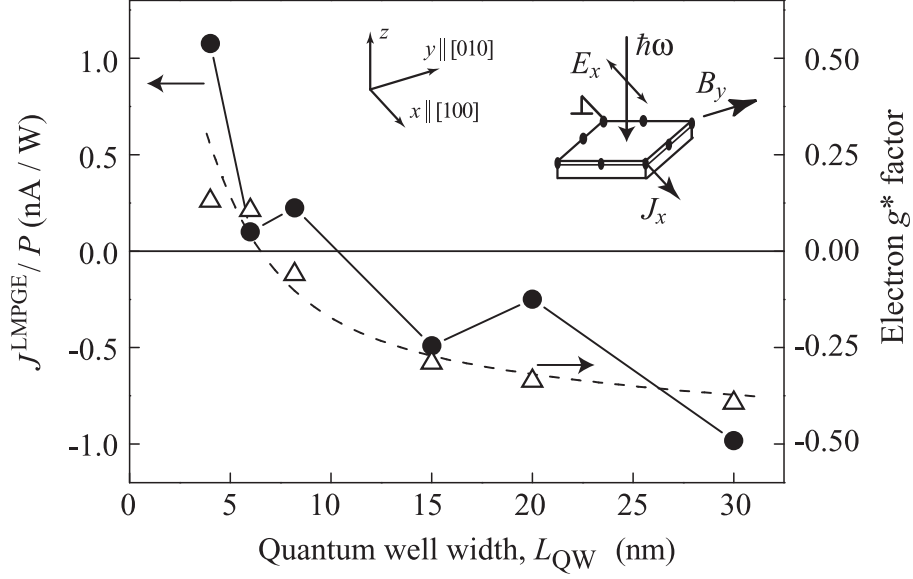


**Figure 40:** Dependence of the linear MPGE (circles) on  $L_{QW}$ . Results were obtained at room temperature,  $B_y = \pm 1$  T and  $\hbar\omega = 4.4$  meV. The corresponding  $g^*$  factors (triangles, by TRKR) are also given for all samples. Inset: Experimental geometry for the linear MPGE.

### 6.2.2 Discussion

For a qualitative explanation of the experimental results, obtained by the investigation of the linear MPGE, the basic physics of both possible mechanisms are described. First the spin based microscopic model of the MPGE, which was already explained in detail in section 2.2.1, is taken up again. Here, a spin-polarized current results due to the asymmetric phonon assisted energy relaxation of a non-equilibrium electron gas, heated by e.g. THz or microwave radiation [51, 123]. Important at that is the external magnetic field, leading to Zeeman splitted spin subbands  $s_y = \pm 1/2$ , as Figure 41 sketches. The asymmetric spin-dependent scattering probability stems from the spin-orbit interaction in gyrotropic media [51] and can be estimated from the scattering matrix element given in Eq. (25):

$$W_{\mathbf{k}'\mathbf{k}} = W_0 \{1 + \xi [\boldsymbol{\sigma} \times (\mathbf{k} + \mathbf{k}')]\}_z, \quad (67)$$

where  $W_0$  is the symmetric part of the scattering probability, determining the mobility (we consider SIA only). Here  $\mathbf{k}$  and  $\mathbf{k}'$  are the initial and scattered

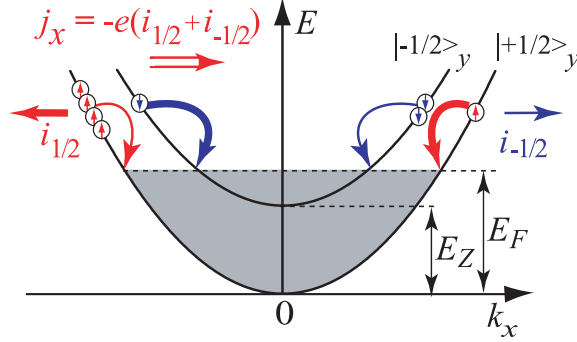


**Figure 41:** Spin based model for the linear MPGE. Different scattering probabilities are indicated by the thicknesses of the arrows.

electron wave vectors and  $\sigma$  is the vector composed of the Pauli matrices. The in-plane magnetic field induces an imbalance between the oppositely directed electron fluxes of equal strength  $i_{\pm 1/2} \propto \xi$ , yielding a net electric current. Obviously, this spin-polarized current, classified as linear MPGE, is proportional to the Zeeman spin splitting induced by the magnetic field. Its QW width dependence is described by the product  $g^* \xi$ .

To estimate this SIA-induced parameter  $\xi$ , remote impurities are taken into account. They create an electric field  $\mathcal{E}$  along the growth direction, which leads to the asymmetry of the QW. Hence, in this structure the eigenstates are superpositions of the states of the rectangular QW. Consequently, the envelope wave functions in the first and second size quantized subband  $\phi_{1,2}(z)$  are denoted by:

$$\begin{aligned}\phi_1(z) &= \varphi_1(z) + \frac{e\mathcal{E}z_{21}}{E_{21}} \varphi_2(z), \\ \phi_2(z) &= \varphi_2(z) - \frac{e\mathcal{E}z_{21}}{E_{21}} \varphi_1(z).\end{aligned}\tag{68}$$

Here,  $z$  is the growth direction,  $\varphi_{1,2}(z)$  are the functions of size quantization in the ground and the first excited subbands of the rectangular QW of width  $L_{\text{QW}}$ ,  $E_{21}$  is the energy separation between these subbands, and  $z_{21}$  is the coordinate matrix element calculated between these states. This leads to

$\xi(L_{\text{QW}}) \sim z_{21}/E_{21}$ , and a spin-based contribution to the linear MPGE current that shows the following dependence:

$$\mathbf{j}_{\text{spin}}^{\text{L}}(L_{\text{QW}}) \sim g^*(L_{\text{QW}}) \frac{z_{21}}{E_{21}}. \quad (69)$$

Here a weak dependence of the scattering probability on the QW width is disregarded.

In the here investigated sample set II, where all samples have a similar structure inversion asymmetry that is controlled by the asymmetric doping, the linear MPGE should, after Eq. (69), vanish for a sample with zero  $g^*$  factor and change its sign upon the variation of the QW width. Thus, this spin-related mechanism describes the current's sign inversion very well. However, it can not explain the difference in QW width of about 4 nm between the inversion points of photocurrent and  $g^*$  factor<sup>1</sup>. To explain this difference, an additional spin-independent orbital contribution to the linear MPGE, which was recently addressed by S. Tarasenko [19], is required.

A process resulting in the orbital contribution to the linear MPGE is illustrated in Fig. 42. Now, the in-plane motion of carriers is analyzed, which are exposed to both, a high-frequency electric field (e.g. THz radiation) applied along the  $x$  direction and an in-plane magnetic field pointing in the  $y$  direction. Linearly polarized radiation forces the electrons, due to the oscillating electric field  $\mathbf{E}(t)$ , into a see-saw motion with the velocity  $\mathbf{v}(t)$ . This is shown in Fig. 42 for different times  $t_1$  and  $t_2$ . Disregarding the magnetic field, the asymmetrical doping leads to a localization of the electron's wave function closer to one interface. Thus, the momentum relaxation rate  $1/\tau_p$  is also controlled by scattering on this interface. The orbital contribution to the linear MPGE is based on the combined action of the applied electric and magnetic fields, as explained subsequently. At a certain time  $t_1$ ,  $\mathbf{E}(t)$  accelerates the electron, due to the in-plane  $ac$  electric field, in the negative  $x$  direction. Simultaneously, the magnetic field  $B_y$  acts on the electron moving with velocity  $v_x(t_1)$ . Therefore,

---

<sup>1</sup>Note, that in the comparison of the MPGE data (obtained at room temperature) with the  $g^*$ -factor behavior (measured at low temperatures) the weak temperature dependence of the  $g^*$ -factor is not considered. This dependence [124, 125] may result in a small shift of the  $g^*$ -factor's zero crossing.

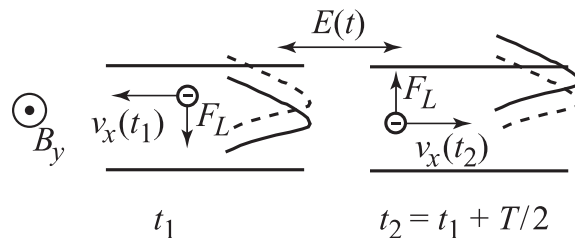


**Figure 42:** Orbital model for the linear MPGE. Solid and dashed lines show the electron wavefunction with and without radiation, respectively.

the Lorentz force  $\mathbf{F}_L = e(\mathbf{v}(t_1) \times \mathbf{B})$  results, which shifts the wave function to the center of the quantum well and thus, decreases the scattering probability (see Fig. 42). At  $t_2 = t_1 + T/2$ , half a period later, the direction of the electron's velocity inverts. Hence, the direction of the Lorentz force reverses as well. Consequently at  $t_2$ , the electron wave function is pushed closer to the interface, leading to a larger scattering rate and slower momentum relaxation. The resulting difference between the relaxation times for positive and negative  $v_x$ , causes a net electric current proportional to the magnetic field strength. Apparently, a photocurrent resulting from this mechanism does not change its direction upon the variation of the QW width. The microscopic origin, of the orbital contribution in the linear MPGE current  $\mathbf{j}_{\text{orb}}^L$ , lies in the influence of a magnetic field on scattering. Due to an in-plane  $\mathbf{B}$ -field, a  $\mathbf{k}$ -dependent mixing of the eigenstates  $\phi_1$  and  $\phi_2$  arises, and the envelope in the ground subband becomes  $k_\alpha B_\beta$ -dependent [19]:

$$\psi_{1\mathbf{k}}(z) = \phi_1(z) + (\mathbf{k} \times \mathbf{B})_z \frac{e\hbar}{m} \frac{z_{21}}{E_{21}} \phi_2(z). \quad (70)$$

Thus, the following contribution in the scattering probability emerges:

$$W_{\mathbf{k}'\mathbf{k}} = W_0 \{1 + \zeta [\mathbf{B} \times (\mathbf{k} + \mathbf{k}') ]_z \}, \quad (71)$$

where the parameter  $\zeta$  is caused by SIA. The dependence of  $\mathbf{j}_{\text{orb}}^L$  on the quantum well width is determined by  $\zeta(L_{\text{QW}})$  and can be denoted as:

$$\mathbf{j}_{\text{orb}}^L(L_{\text{QW}}) \sim \left( \frac{z_{21}}{E_{21}} \right)^2. \quad (72)$$

The quadratic dependence on the parameter  $z_{21}/E_{21}$  results, because the electric field of the impurities as well as the magnetic field yield a mixing of the ground and first excited levels (see Eqs. (68) and (70)). For Eq. (72), as for Eq. (69), additional factors originating from the scattering asymmetry are assumed to depend weakly on  $L_{\text{QW}}$  as well. The Equations (69) and (72) reveal that spin and orbital contributions do not depend equally on a variation of the well width. The ratio of these two contributions,  $j_{\text{spin}}^{\text{L}}/j_{\text{orb}}^{\text{L}}$ , alters as  $g^* E_{21}/z_{21}$ , which is a strong function of  $L_{\text{QW}}$ .

Both spin and orbital mechanisms are described by the same phenomenological equations and contribute to the total current:

$$\mathbf{j}^{\text{L}} = \mathbf{j}_{\text{spin}}^{\text{L}} + \mathbf{j}_{\text{orb}}^{\text{L}}. \quad (73)$$

Due to the phenomenological analogy, the decomposition of these two terms is obstructed: Both contributions, the spin-related  $\mathbf{j}_{\text{spin}}^{\text{L}}$  as well as the orbital one  $\mathbf{j}_{\text{orb}}^{\text{L}}$  depend equally on a variation of the radiation's polarization state or of the magnetic field direction relative to the crystallographic axes. The above analysis shows, however, that the dependence of the photocurrent on the QW width enables the distinction between these two basically different mechanisms. The observed change of sign and especially the similarity in the dependences, of total current and  $g^*$  factor on  $L_{\text{QW}}$ , prove that in most samples the spin-related mechanism is dominant. The difference in sign of the MPGE current and the  $g^*$  factor in the sample with  $L_{\text{QW}} = 8.2$  nm, resulting from the shift between the MPGE's (to larger  $L_{\text{QW}}$ ) and the  $g^*$  factor's inversion point, is attributed to the orbital contribution in the current. This result, furthermore, demonstrates that both, orbital and spin mechanisms, contribute in the MPGE formation, however, mostly the spin mechanism dominates. For  $L_{\text{QW}} \approx 6.5$  nm the  $g^*$  factor is equal to zero. Thus, in this case, the MPGE is solely caused by the orbital mechanism.

Figure. 43 shows the dependence of  $\mathbf{j}_{\text{orb}}^{\text{L}}$  on the quantum well width, calculated after Eq. (72). It visualizes the increase of the current with rising  $L_{\text{QW}}$ , due to the proportionality of the mixing parameter  $z_{21}/E_{21}$  and  $L_{\text{QW}}$ , and that this current always has the same sign. These properties are based on the following facts: In narrow QWs the energy separation  $E_{21}$  becomes large and thus,

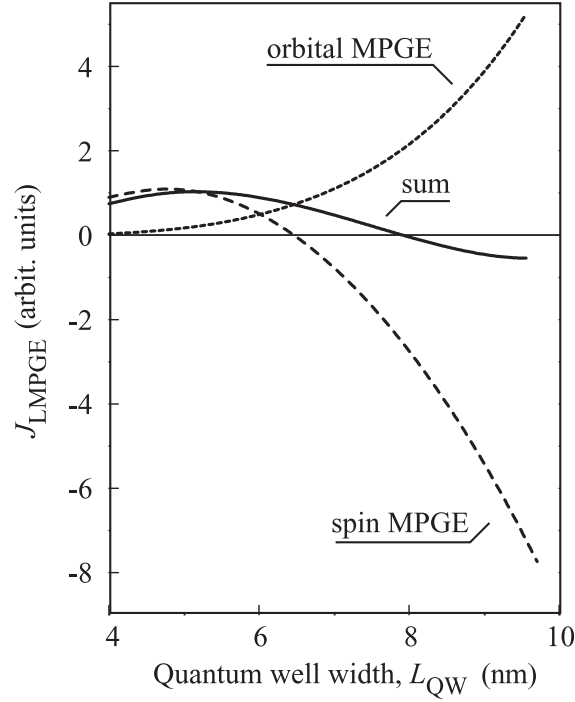


**Figure 43:**  $L_{QW}$ -dependence of spin-dependent and orbital contribution to the linear MPGE.

electric and magnetic fields can no longer mix size-quantized states efficiently. In wider QWs the confinement gets weaker, resulting in an increasing photocurrent. This strong dependence holds for not too wide QWs, where only the ground subband is occupied. If the QWs get very broad, the photocurrent first reaches a maximum and then tends to zero, since in bulk GaAs photogalvanic effects are absent.

In Figure 43 also the interplay of both contributions is illustrated. This curve was obtained by normalizing both contributions so that the total current vanishes at a QW width, where the photocurrent's sign inversion has been detected. It is visible that the total photocurrent vanishes at a larger  $L_{QW}$  than the  $g^*$  factor, which is due to the influence of the orbital contribution.

## 6.3 Circular MPGE

### 6.3.1 Experimental results

Also the experiments concerning the circular MPGE were carried out at room temperature on sample set II [21]. Hereby, the same laser source and experimental setup were used as in the measurements of the linear MPGE, see the insets of Figs. 44 and 45. The only differences are that now the in-plane magnetic field is applied along the  $x$  axis and that circularly polarized radiation is required, which was generated using a  $\lambda/4$  plate. The angle  $\varphi$  denotes the rotation angle of the wave plate, indicating the helicity of light (for details see Section 3.2). The resulting photocurrent was measured in all samples, via the voltage drop across a load resistor, parallel to the  $\mathbf{B}$ -field along the  $x$ -direction. This current direction was chosen to obtain again a purely SIA-induced MPGE, analog to the linear MPGE. The SIA-induced circular MPGE provides experimental results that are very similar to the ones obtained in the investigation of the linear MPGE: Also the circular MPGE changes its sign upon a variation of the QW width. These results will be presented and analyzed in detail in this section.

In Figure 44 the helicity dependence of the photocurrent  $J_x$  is illustrated, as it results under rotation of the  $\lambda/4$  plate. It clearly demonstrates the fingerprint of the circular MPGE, which is the current's sign inversion upon switching the radiation's helicity  $P_{\text{circ}}$  from  $+1$  to  $-1$  at  $\varphi = 45^\circ$  ( $\sigma^+$ ) and  $\varphi = 135^\circ$  ( $\sigma^-$ ), respectively. The whole polarization dependence results from the interplay between circular and linear MPGE. After the phenomenological theory [58] the photocurrent can be well fitted by  $J_x = AP_{\text{circ}} + B(1 + \cos 4\varphi) + C \sin 4\varphi$ . Here the first term, which is proportional to the helicity and contains parameter  $A$ , originates from the circular MPGE. The second and third term, including the coefficients  $B$  and  $C$ , are caused by the linear MPGE discussed above and disappear for purely circularly polarized radiation. For the further data analysis, the pure circular MPGE was extracted from the helicity dependence of the total current, herewith, any spurious currents are avoided as well. In

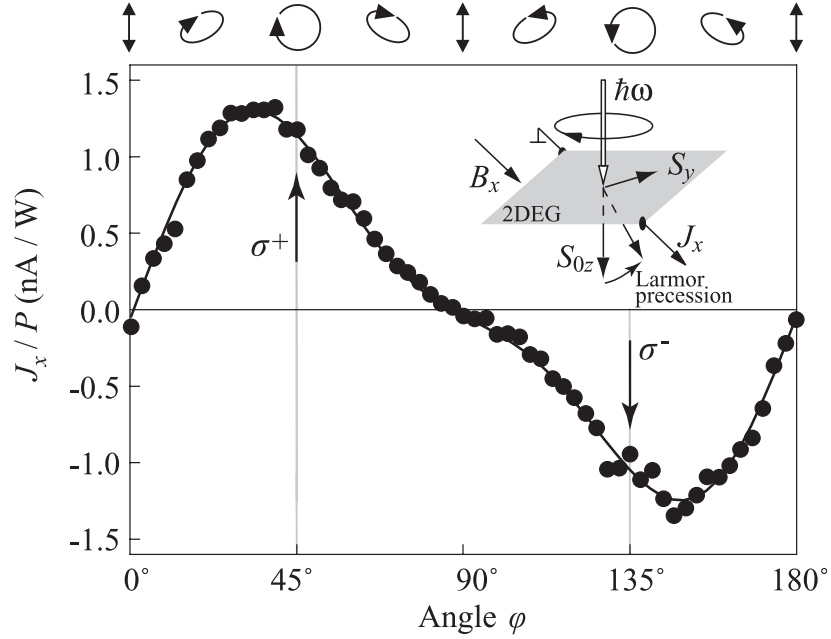


**Figure 44:** Helicity dependence of the MPGE obtained for sample A at room temperature,  $|\mathbf{B}| = 1$  T and a photon energy of  $\hbar\omega = 4.4$  meV. The ellipses on top illustrate the polarization states for various angles of the  $\lambda/4$  plate,  $\varphi$ . Inset: Spin-galvanic effect.

the separation, the circular MPGE's sign inversion under the transition from  $\sigma^+$  to  $\sigma^-$  polarized light was used and the circular photocurrent results after:

$$J_x^{\text{CMPGE}} = [J_x(\sigma^+) - J_x(\sigma^-)]/2. \quad (74)$$

Here  $J_x(\sigma^+)$  and  $J_x(\sigma^-)$  are the photocurrents measured at  $\sigma^+$ - and  $\sigma^-$ -polarized excitation. Since the circular MPGE changes its sign as well upon reversing the polarity of the magnetic field, the current after Eq. (74) is further treated, similarly to the linear MPGE, according to Eq. (53).

The QW width dependence of the that way obtained pure circular MPGE current is displayed in Figure 45: This circular photocurrent also reverses its sign at a certain QW width<sup>2</sup>. Analogues to the linear MPGE, the sign inversion of the photocurrent in Fig. 45 emerges at another QW width as the one of the

<sup>2</sup>Note, that, as for the linear MPGE, the current in the 4 nm broad QW is enhanced due to the larger parameter  $\chi$  compared to the other samples.

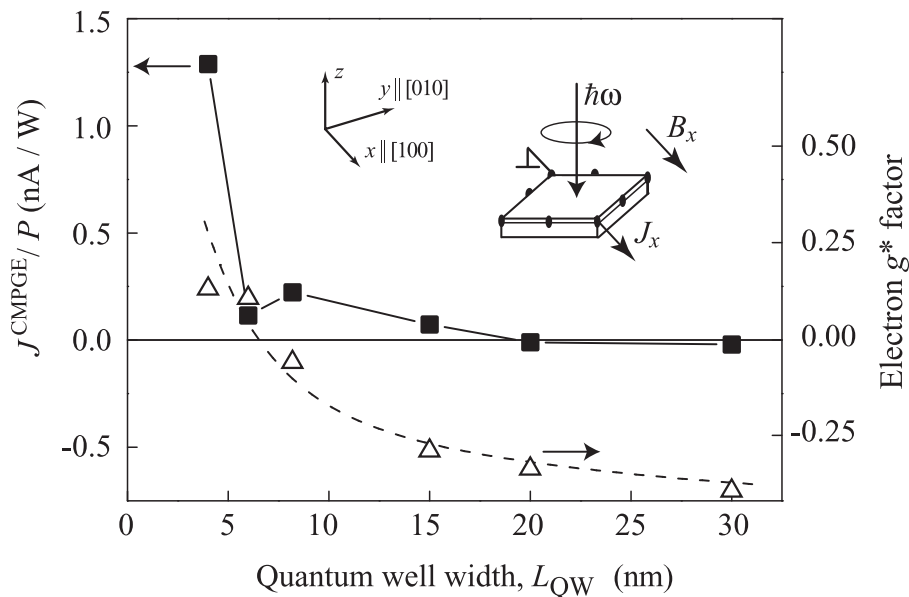


**Figure 45:** Dependence of the circular MPGE (squares) on  $L_{QW}$  obtained at room temperature,  $|\mathbf{B}| = 1$  T and a photon energy of  $\hbar\omega = 4.4$  meV and corresponding  $g^*$  factors (triangles, by TRKR). Inset: Experimental geometry for the circular MPGE.

Landé factor, namely at  $L_{QW} \sim 18$  nm. Now, even two samples exist, which exhibit a difference in sign between circular photocurrent and  $g^*$  factor. In the discussion [21] it is shown that, similarly to the earlier considered linear MPGE, these facts indicate the interplay of spin and orbital mechanisms in the circular MPGE.

### 6.3.2 Discussion

The microscopic model for the spin-related contribution to the circular MPGE is rested on the spin-galvanic effect [59]. This effect describes the current generation via asymmetric spin relaxation of a non-equilibrium spin polarization (for details see Section 2.2.2). The spin-galvanic current is connected with the average non-equilibrium spin  $\mathbf{S}$  by a second rank pseudotensor, whose components are proportional to the parameters of the spin-orbit splitting:

$$j_{\text{spin},\alpha}^{\text{CMPGE}} = \sum_{\gamma} Q_{\alpha\gamma} S_{\gamma}. \quad (75)$$

In (001)-grown zinc-blende structure based QWs of  $C_{2v}$ -symmetry, the spin-galvanic effect (SGE) is only allowed, for a non-zero in-plane spin component. Using the coordinate system  $x \parallel [100]$ ,  $y \parallel [010]$ , Eq. (75) reduces to  $j_x^{\text{SIA}} = Q_{xy}S_y$  and  $j_y^{\text{BIA}} = Q_{yy}S_y$ , with  $j_x^{\text{SIA}}$  and  $j_y^{\text{BIA}}$  being proportional to the Rashba and the Dresselhaus constants, respectively [52]. The spin polarization, required for the SGE, can, besides optical excitation, also be achieved by non-optical methods, as e.g. electrical spin injection.

The spin-related contribution in the circular MPGE  $\mathbf{j}_{\text{spin}}^{\text{CMPGE}}$  is caused by the asymmetry in the spin relaxation. This asymmetry is linear in the in-plane wave vector  $\mathbf{k}$  and originates from the Rashba spin-orbit splitting of the electronic ground subband:

$$E_{1\uparrow} - E_{1\downarrow} = \hbar\Omega. \quad (76)$$

Here, the  $\mathbf{k}$ -linear SIA-induced spin-orbit splitting  $\hbar\Omega$  is estimated via TRKR measurements (see Sec. 6.1).

An optical method, delivering a non-equal population of an uniform distribution in both spin subbands, was suggested in Ref. [59] and is outlined in the inset of Fig. 44. This method uses optical excitation with circularly polarized light to reach a steady-state spin orientation  $S_{0z}$  along the growth direction. Subsequently, the optically oriented spins are rotated, due to the Larmor precession caused by the in-plane magnetic field, into the plane of the 2DEG. For  $\mathbf{B} \parallel x$ , a non-equilibrium spin polarization  $S_y$  results, which reads after time averaging [59]:

$$S_y = -\frac{\omega_L \tau_{s\perp}}{1 + (\omega_L \tau_s)^2} S_{0z}. \quad (77)$$

Here  $\tau_s = \sqrt{\tau_{s\parallel} \tau_{s\perp}}$  and  $\tau_{s\parallel}, \tau_{s\perp}$  are the longitudinal and transverse electron spin relaxation times, the Larmor frequency is given by  $\omega_L = g^* \mu_B B_x / \hbar$ ,  $\mu_B$  is the Bohr magneton, and  $S_{0z} = \tau_{s\parallel} \dot{S}_z$  is the steady state electron spin polarization without magnetic field. After Eq. (75) the in-plane spin polarization  $S_y$  yields a net electric current parallel to the magnetic field. At room temperature, for the investigated QWs  $\omega_L \tau_s \ll 1$  holds, thus, the photocurrent is proportional to  $g^* B_y$ .

The spin-based contribution in the circular MPGE,  $\mathbf{j}_{\text{spin}}^{\text{CMPGE}}$ , depends in the following way on the QW width:

$$\mathbf{j}_{\text{spin}}^{\text{CMPGE}}(L_{\text{QW}}) \sim g^*(L_{\text{QW}}) \Omega(L_{\text{QW}}) \tau_s^2(L_{\text{QW}}). \quad (78)$$

This contribution is after Equation (78) proportional to the  $g^*$  factor and, consequently, acts similarly on the variation of the QW width<sup>3</sup>. In QW's with  $g^* = 0$ , this spin-dependent contribution  $\mathbf{j}_{\text{spin}}^{\text{CMPGE}}$  vanishes. The change in sign of the  $g^*$  factor in GaAs/AlGaAs QWs upon the variation of  $L_{\text{QW}}$  explains the circular MPGE's sign inversion qualitatively. By contrast, the difference in the zero points of  $g^*$  factor and photocurrent (as well as the unequal signs of current and  $g^*$  factor in the samples C and E), can not be explained by the spin mechanism. The clarification of this experimental finding requires the contribution of an orbital mechanism to the circular MPGE.

A helicity driven MPGE current based on an orbital mechanism was recently suggested in Ref. [20] and reads as:

$$\mathbf{j}_{\text{orb},\alpha}^{\text{CMPGE}} = P_{\text{circ}} |E_0|^2 \sum_{\gamma} R_{\alpha\gamma} B_{\gamma}. \quad (79)$$

The second rank pseudotensor  $\mathbf{R}$  exhibits the same space symmetry properties as the pseudotensor  $\mathbf{Q}$ , which describes the spin-galvanic effect. However, the tensor  $\mathbf{R}$  is invariant under time inversion. The microscopic origin of the orbital contribution to the circular MPGE is similar to the one for the earlier described linear MPGE. The current results from the influence of the Lorentz force on the orbital motion of the 2D electrons in the radiation field. Due to the illumination with circularly polarized radiation the electrons are forced into a cyclic motion. At the same time, the in-plane magnetic field is present, which leads in combination with SIA to an electron flow predominantly along the direction of  $\mathbf{B}$ . Switching the radiation's polarization from  $\sigma^+$  to  $\sigma^-$ , changes the current direction. In Ref. [20], the microscopic theory of this effect is

---

<sup>3</sup>Note, that recently in Ref. [126] an additional possible origin of the spin-galvanic effect was covered. Instead of the in Ref. [59] addressed SGE due to band spin splitting, it is based on the spin-dependent scattering given by Eq. (67). However, this mechanism also creates a contribution proportional to the Zeeman splitting but does not change the discussion about the MPGE's  $L_{\text{QW}}$ -dependence qualitatively.

considered. Here,  $\mathbf{B}$ -dependent corrections to the scattering probability (see Eq. (71)) provoke the orbital current contribution  $\mathbf{j}_{\text{orb}}^{\text{CMPGE}}$ , just as in the linear MPGE. The orbital contributions in the circular and linear MPGE are related to each other, according to  $\mathbf{j}_{\text{orb}}^{\text{CMPGE}} \sim \mathbf{j}_{\text{orb}}^{\text{L}} \omega \tau_p$  for  $\omega \tau_p \ll 1$  (see Ref. [19]). Hereby and with Equation (72) the QW width dependence of  $\mathbf{j}_{\text{orb}}^{\text{CMPGE}}$  can be estimated to:

$$\mathbf{j}_{\text{orb}}^{\text{CMPGE}}(L_{\text{QW}}) \sim \left( \frac{z_{21}}{E_{21}} \right)^2. \quad (80)$$

After Eq. (80), the orbital contribution to the circular MPGE does not change its sign under the variation of the QW width. Hence, the observed sign inversion of the total circular MPGE and the difference in the zero crossings of  $g^*$  factor and current, can be explained by the interplay of comparable spin and orbital contributions.

In the total circular MPGE current  $\mathbf{j}^{\text{CMPGE}} = \mathbf{j}_{\text{spin}}^{\text{CMPGE}} + \mathbf{j}_{\text{orb}}^{\text{CMPGE}}$  spin and orbital mechanisms contribute, which are both described by similar phenomenological equations. The observed sign inversion proves that the dominant contribution stems, in correspondence with the linear MPGE, from the spin-related mechanism, thus the spin-galvanic effect. While the SGE dominates the current for most of the investigated samples, the existence of the orbital circular MPGE is also clearly demonstrated. In particular, for QWs with  $L_{\text{QW}} \approx 6.5$  nm the spin-galvanic effect vanishes and the current is solely caused by the orbital circular MPGE.

## 6.4 Summary

In this chapter the origins of both linear and circular SIA-induced MPGEs were studied in  $n$ -type (001)-grown GaAs/AlGaAs QWs of different well width. Currents proportional to BIA were neglected, because BIA itself depends strongly on  $L_{\text{QW}}$ . To investigate the interplay of the well known spin-related mechanism and a possible orbital contribution, the dependence of sign and strength of the Landé factor  $g^*$  on  $L_{\text{QW}}$  in GaAs/AlGaAs QWs was used [21]. Additionally, all samples were characterized by PL and TRKR measurements,

hereby, among others the  $g^*$  factor was estimated in each sample. To summarize, the here performed experiments demonstrate that the  $L_{\text{QW}}$ -dependences of both total SIA-induced MPGE currents are very similar to the  $g^*$  factor's dependence on  $L_{\text{QW}}$ . This proves the preponderance of the spin-based mechanism in both, linear and circular MPGE. Hereby, it became evident that the microscopic origin of the spin contribution in the circular MPGE is given by the spin-galvanic effect. Moreover, the experimental results, in particular the difference in zero points of current and  $g^*$  factor, can only be explained by the supplementary contribution of an orbital mechanism in the current formation. Thus, in both, linear as well as circular MPGE, the interplay of spin and orbital mechanisms is detected. Furthermore, while for most QW widths the main contribution to both MPGEs is spin-based, in samples with a vanishing  $g^*$  factor, however, both MPGEs are caused by orbital mechanisms solely. The measurements were accompanied by theoretical calculations, estimating the QW width dependence of both contributions in the MPGE, which are in a good agreement. In this work, for the first time a method was developed, which allows to separate and analyze the qualitatively different spin and orbital mechanisms in both roots of the MPGE. This method is based on the variation of the electron  $g^*$  factor upon changing the QW width. Further possibilities to vary the  $g^*$  factor, would be the doping with magnetic impurities or the use of narrow band materials, where  $g^*$  and the spin-orbit interaction are enhanced. In addition, both orbital MPGEs can be examined independently in materials with negligible spin-orbit interaction, as e.g. Si-based metal-oxide-semiconductor low dimensional structures.

## 7 Conclusions

To summarize, in this work the anisotropy of the band spin splitting, which is caused by the interference of BIA and SIA, was investigated experimentally in low dimensional III-V semiconductor heterostructures. Herewith, basic rules for the design of QW structures with a defined SIA/BIA-ratio were obtained. These goals were achieved applying a newly developed opto-electronic method, based on the analysis of the MPGE's anisotropy, as well as the well established methods employing the CPGE and the SGE. Moreover, through this work, QWs with equal strengths of Rashba and Dresselhaus spin splitting were gained. Such materials are a crucial prerequisite for future spintronic devices, since they allow among other things the formation of a spin helix. Furthermore, the study of photogalvanic effects together with magneto-transport experiments in QWs with strong SOI and numerical simulations permitted to estimate the influence of  $\mathbf{k}$ -cubic terms on the PSH formation. An other aim of this work was to study the microscopic origins underlying the formation of the MPGE current. Here, we demonstrated that both spin and orbital mechanisms contribute in the formation of the linear as well as the circular MPGE in GaAs/AlGaAs QWs.

In the first part of this work, it was demonstrated that the MPGE due to unpolarized radiation is a proper tool to analyze SIA and BIA. Herewith, both inversion asymmetries were investigated in (001)-oriented GaAs/AlGaAs QWs at room temperature [7]. In the experiment a modulation of the SIA/BIA-ratio was observed upon a variation of the doping position. This proves the importance of the impurity position for SIA, while BIA is not affected. Furthermore, the results illustrated the influence of the impurity segregation on SIA and verified that the high growth temperatures, of high-quality (001)-oriented GaAs QWs, evoke the segregation. An advantage of this method to study SIA and BIA is its feasibility even at room temperature, where many other methods cannot be used. Through the investigation of samples with different  $\delta$ -doping positions, we obtained QWs with almost equal magnitudes of Rashba and Dresselhaus constants. They should exhibit extraordinarily long spin relaxation times and allow the formation of a persistent spin helix. Thus, these QWs are very promising candidates regarding future spintronic devices.

The second part covered the study of BIA and SIA in (001)-grown InGaAs/InAlAs QWs, which allows to investigate the influence of a strong spin-orbit interaction on the PSH formation [13]. The experiments evidenced the existence as well as the gate control of a PSH state even in the presence of a strong,  $\mathbf{k}$ -cubic SOI through an accurate engineering of Rashba and Dresselhaus SOIs. To analyze the corresponding spin splittings, three independent methods based on the study of the anisotropies in CPGE, SGE and WAL, were employed. All three methods revealed a Rashba/Dresselhaus-ratio of about 1 for a 4 nm broad QW, while in a 7 nm wide QW the strengths of these SOIs differ. In magneto-transport measurements a clearcut WAL-WL-WAL transition was detected for the 4 nm broad QW upon tuning a gate electric field. This proves the PSH state, while in the 7 nm sample the difference between Rashba and Dresselhaus terms was too large to fulfill the PSH condition by applying a gate voltage. Moreover, the independently obtained experimental results agree well with quantum transport calculations, and both experiments and theory reveal the robustness of the PSH, which can even be achieved in materials with a substantial  $\mathbf{k}$ -cubic SOI contribution. The crucial requirement therefor is that  $\alpha$  and  $\beta$  are similar without gate voltage. This condition can be achieved in very narrow and almost symmetric QWs due to a specially designed doping profile. However, in contrast to systems with dominating  $\mathbf{k}$ -linear spin splitting, the PSH condition deviates from  $\alpha = \pm\beta$ , and even from  $\alpha = \pm\tilde{\beta}$ .

The last part of this work, explored the microscopic origins of the linear as well as circular MPGE in (001)-grown GaAs/AlGaAs QWs. To investigate the interplay of spin and orbital mechanisms, the dependence of sign and strength of the Landé factor  $g^*$  on  $L_{\text{QW}}$  in these structures was used [21]. The obtained experimental results clearly verify that both MPGEs result from spin and orbital contributions. Furthermore, they show the preponderance of the spin-related mechanism for most quantum well widths, which results in a photocurrent proportional to the  $g^*$  factor. However, for structures with a vanishing  $g^*$  factor, both MPGEs are solely caused by orbital mechanisms. Our findings demonstrate that modifying the electron  $g^*$  factor, by a variation of the QW width, can be used for the separation of these qualitatively different mechanisms. Another possibility to influence  $g^*$ , would be doping with magnetic impurities

or using narrow band materials, where  $g^*$  and the spin-orbit interaction are enhanced. Moreover, in materials with a vanishingly small SOI, as Si-based metal-oxide-semiconductor low dimensional structures, the orbital MPGE can be studied independently.

## References

- [1] I. Žutić, J. Fabian, and S. Das Sarma, *Spintronics: Fundamentals and applications*, Rev. Mod. Phys. **76**, 323 (2004).
- [2] S. A. Wolf, D. D. Awschalom, R. A. Buhrman, J. M. Daughton, S. von Molnar, M. L. Roukes, A. Y. Chtchelkanova, and D. M. Treger, *A Spin-Based Electronics Vision for the Future*, Science **294**, 1488 (2001).
- [3] D. D. Awschalom, D. Loss, and N. Samarth, *Semiconductor Spintronics and Quantum Computation*. in Nanoscience and Technology, eds. K. von Klitzing, H. Sakaki, and R. Wiesendanger (Springer, Berlin, 2002).
- [4] R. Winkler, *Spin-Dependent Transport of Carriers in Semiconductors (Handbook of Magnetism and Advanced Magnetic Materials)*. John Wiley & Son, New York, 2007.
- [5] J. Fabian, A. Matos-Abiague, C. Ertler, P. Stano, and I. Žutić, *Semiconductor Spintronics*, Acta Phys. Slovaca **57**, 565 (2007).
- [6] M. I. Dyakonov, *Spin Physics in Semiconductors*. Springer, Berlin, 2009.
- [7] V. Lechner, L. E. Golub, P. Olbrich, S. Stachel, D. Schuh, W. Wegscheider, V. V. Bel'kov, and S. D. Ganichev, *Tuning of structure inversion asymmetry by the  $\delta$ -doping position in (001)-grown GaAs quantum wells*, Appl. Phys. Lett. **94**, 242109 (2009).
- [8] J. Nitta, T. Akazaki, and H. Takayanagi, *Gate control of spin-orbit interaction in an inverted  $In_{0.53}Ga_{0.47}As/In_{0.52}Al_{0.48}As$  heterostructure*, Phys. Rev. Lett. **78**, 1335 (1997).
- [9] G. Engels, J. Lange, Th. Schäpers, and H. Lüth, *Experimental and theoretical approach to spin splitting in modulation-doped  $In_xGa_{1-x}As/InP$  quantum wells for  $B \rightarrow 0$* , Phys. Rev. B **55**, R1958 (1997).
- [10] E. I. Rashba Sov. Phys. Solid State **2**, 1109 (1960).

- [11] G. Dresselhaus, *Spin-orbit coupling effects in zinc blende structures*, Phys. Rev **100**, 580 (1955).
- [12] V. V. Bel'kov, P. Olbrich, S. A. Tarasenko, D. Schuh, W. Wegscheider, T. Korn, C. Schüller, D. Weiss, W. Prettl, and S. D. Ganichev, *Symmetry and Spin Dephasing in (110)-Grown Quantum Wells*, Phys. Rev. Lett. **100**, 176806 (2008).
- [13] M. Kohda, V. Lechner, Y. Kunihashi, T. Dollinger, P. Olbrich, C. Schönhuber, I. Caspers, V. V. Bel'kov, L. E. Golub, D. Weiss, K. Richter, J. Nitta, and S. D. Ganichev, *Gate-controlled Persistent Spin Helix State in Materials with Strong Spin-Orbit Interaction*, arXiv: 1205.5630v1 [cond-mat.mes-hall] (2012).
- [14] N. S. Averkiev and L. E. Golub, *Giant spin relaxation anisotropy in zinc-blende heterostructures*, Phys. Rev. B **60**, 15582 (1999).
- [15] J. Schliemann, J. C. Egues, and D. Loss, *Nonballistic Spin-Field-Effect Transistor*, Phys. Rev. Lett. **90**, 146801 (2003).
- [16] B. A. Bernevig, J. Orenstein, and S. C. Zhang, *Exact  $SU(2)$  Symmetry and Persistent Spin Helix in a Spin-Orbit Coupled System*, Phys. Rev. Lett. **97**, 236601 (2006).
- [17] X. Cartoixá, D. Z.-Y. Ting, and Y.-C. Chang, *A resonant spin lifetime transistor*, Appl. Phys. Lett. **83**, 1462 (2003).
- [18] Y. Kunihashi, M. Kohda, H. Sanada, H. Gotoh, T. Sogawa, and J. Nitta, *Proposal of spin complementary field effect transistor*, Appl. Phys. Lett. **100**, 113502 (2012).
- [19] S. A. Tarasenko, *Electron scattering in quantum wells subjected to an in-plane magnetic field*, Phys. Rev. B **77**, 085328 (2008).
- [20] S. A. Tarasenko, *Direct current driven by ac electric field in quantum wells*, Phys. Rev. B **83**, 035313 (2011).
- [21] V. Lechner, L. E. Golub, F. Lomakina, V. V. Bel'kov, P. Olbrich, S. Stachel, I. Caspers, M. Griesbeck, M. Kugler, M. J. Hirmer, T. Korn,

- C. Schüller, D. Schuh, W. Wegscheider, and S. D. Ganichev, *Spin and orbital mechanisms of the magneto-gyrotropic photogalvanic effects in GaAs/AlGaAs quantum well structures*, Phys. Rev. B **83**, 155313 (2011).
- [22] J. J. Sakurai, *Advanced Quantum Mechanics*. Addison-Wesley, Reading, 1967.
- [23] L. M. Roth, B. Lax, and S. Zwerdling, *Theory of Optical Magneto-Absorption Effects in Semiconductors*, Phys. Rev. **114**, 90 (1959).
- [24] C. Weisbuch and C. Hermann, *Optical detection of conduction-electron spin resonance in GaAs, Ga<sub>1-x</sub>In<sub>x</sub>As, and Ga<sub>1-x</sub>Al<sub>x</sub>As*, Phys. Rev. B **15**, 816 (1977).
- [25] R. Winkler, *Spin-Orbit Coupling Effects in Two-Dimensional Electron and Hole Systems*. Springer, Berlin, 2003.
- [26] E. L. Ivchenko and S. D. Ganichev, *Spin-Photogalvanics*. in *Spin Physics in Semiconductors*, p. 245, ed. M. I. Dyakonov (Springer, Berlin, 2008).
- [27] L. D. Landau, E. M. Lifshits, and L. P. Pitaevskii, *Electrodynamics of Continues Media*. Elsevier, Amsterdam, 1984.
- [28] J. F. Nye, *Physical Properties of Crystals: Their Representation by Tensors and Matrices*. Oxford Univ. Press, Oxford, 1985.
- [29] V. M. Agranovich and V. L. Ginzburg, *Crystal Optics with Spatial Dispersion, and Excitons*. Springer, Berlin, 1984. (Springer Series in Solid-State Sciences Vol. 42).
- [30] V. A. Kizel', Yu. I. Krasilov, and V. I. Burkov, *Experimental studies of crystal gyrotropy*, Usp. Fiz. Nauk **114**, 295 (1974).
- [31] J. Jerphagnon and D. S. Chemla, *Optical activity of crystals*, J. Chem. Phys. **65**, 1522 (1976).

- [32] S. D. Ganichev and W. Prettl, *Intense Terahertz Excitation of Semiconductors*. Oxford Univ. Press, Oxford, 2006.
- [33] S. D. Ganichev and W. Prettl, *Spin photocurrents in quantum wells*, J. Phys.: Condens. Matter **15**, R935 (2003).
- [34] W. Zawadzki and P. Pfeffer, *Spin splitting of subbands energies due to inversion asymmetry in semiconductor heterostructures*, Semicond. Sci. Technol. **19**, R1 (2004).
- [35] N. S. Averkiev and L. E. Golub, *Spin relaxation anisotropy: microscopic mechanisms for 2D systems*, Semicond. Sci. Technol. **23**, 114002 (2008).
- [36] M. I. Dyakonov and V. Yu. Kachorovskii, *Spin relaxation of two-dimensional electrons in noncentrosymmetric semiconductors*, Fiz. Tekh. Poluprovodn. **20**, 178 (1986).
- [37] Y. A. Bychkov and E. I. Rashba, *Properties of a 2D electron gas with lifted spectral degeneracy*, Pis'ma Zh. Eksp. Teor. Fiz. **39**, 66 (1984).
- [38] V. K. Kalevich and V. L. Korenev, *Effect of electric field on the optical orientation of 2D electrons*, Pis'ma Zh. Eksp. Teor. Fiz. **52**, 859 (1990).
- [39] J. P. Lu, J. B. Yau, S. P. Shukla, M. Shayegan, L. Wissinger, U. Rössler, and R. Winkler, *Tunable spin-splitting and spin-resolved ballistic transport in GaAs/AlGaAs two-dimensional holes*, Phys. Rev. Lett. **81**, 1282 (1998).
- [40] J. P. Heida, B. J. van Wees, J. J. Kuipers, T. M. Klapwijk, and G. Borghs, *Spin-orbit interaction in a two-dimensional electron gas in a InAs/AlSb quantum well with gate-controlled electron density*, Phys. Rev. B **57**, 11911 (1998).
- [41] C.-M. Hu, J. Nitta, T. Akazaki, H. Takayanagi, J. Osaka, P. Pfeffer, and W. Zawadzki, *Zero-field spin splitting in an inverted  $In_{0.53}Ga_{0.47}As/In_{0.52}Al_{0.48}As$  heterostructure: band nonparabolicity influence and the subband dependence*, Phys. Rev. B **60**, 7736 (1999).

- [42] G. Salis, Y. Kato, K. Ensslin, D. C. Driscoll, A. C. Gossard, and D. D. Awschalom, *Electrical control of spin coherence in semiconductor nanostructures*, Nature (London) **414**, 619 (2001).
- [43] J. H. Smet, R. A. Deutschmann, F. Ertl, W. Wegscheider, G. Abstreiter, and K. von Klitzing, *Gate-voltage control of spin interactions between electrons and nuclei in a semiconductor*, Nature (London) **415**, 281 (2002).
- [44] E. I. Rashba, *Properties of semiconductors with an extremum loop. I. Cyclotron and combinational resonance in a magnetic field perpendicular to the plane of the loop*, Fiz. Tverd. Tela **2**, 1224 (1960).
- [45] U. Rössler, F. Malcher, and G. Lommer, *Spin-Splitting in Structured Semiconductors*. in Springer Series in Solid State Sciences Vol. **87**, High Magnetic Fields in Semiconductor Physics II, ed. G. Landwehr (Springer, Berlin, 1989), p. 376.
- [46] L. Vervoort and P. Voisin, *Giant optical anisotropy of semiconductor heterostructures with no common atom and the quantum-confined Pockels effect*, Phys. Rev. B **56**, 12744 (1997).
- [47] U. Rössler and J. Kainz, *Microscopic interface asymmetry and spin-splitting of electron subbands in semiconductor quantum structures*, Solid State Commun. **121**, 313 (2002).
- [48] F. Meier and B. P. Zakharchenya, *Optical Orientation (Modern Problems in Condensed Matter Sciences)*. North-Holland Physics Publishing, Amsterdam, 1984. (ed. F. Meier and B. P. Zakharchenya).
- [49] E. L. Ivchenko, *Optical Spectroscopy of Semiconductor Nanostructures*. Alpha Science Int., Harrow, 2005.
- [50] B. Jusserand, D. Richards, G. Allan, C. Priester, and B. Etienne, *Spin orientation at semiconductor heterointerfaces*, Phys. Rev. B **51**, 4707 (1995).

- [51] S. D. Ganichev, V. V. Bel'kov, S. A. Tarasenko, S. N. Danilov, S. Giglberger, Ch. Hoffmann, E. L. Ivchenko, D. Weiss, W. Wegscheider, Ch. Gerl, D. Schuh, J. Stahl, J. De Boeck, G. Borghs, and W. Prettl, *Zero-bias spin separation*, Nature Phys. **2**, 609 (2006).
- [52] S. Giglberger, L. E. Golub, V. V. Bel'kov, S. N. Danilov, D. Schuh, C. Gerl, F. Rohlfig, J. Stahl, W. Wegscheider, D. Weiss, W. Prettl, and S. D. Ganichev, *Rashba and Dresselhaus spin splittings in semiconductor quantum wells measured by spin photocurrents*, Phys. Rev. B **75**, 035327 (2007).
- [53] S. D. Ganichev, V. V. Bel'kov, L. E. Golub, E. L. Ivchenko, Petra Schneider, S. Giglberger, J. Eroms, J. De Boeck, G. Borghs, W. Wegscheider, D. Weiss, and W. Prettl, *Experimental Separation of Rashba and Dresselhaus Spin Splittings in Semiconductor Quantum Wells*, Phys. Rev. Lett. **92**, 256601 (2004).
- [54] V. V. Bel'kov and S. D. Ganichev, *Magneto-gyrotropic effects in semiconductor quantum wells*, Semicond. Sci. Technol. **23**, 114003 (2008).
- [55] V. V. Bel'kov and S. D. Ganichev, *Zero-bias spin separation (Handbook of Spintronic Semiconductors)*. Pan Stanford Publishing, Singapore, 2010. (ed. W. M. Chen and I. A. Buyanova).
- [56] S. D. Ganichev, S. A. Tarasenko, V. V. Bel'kov, P. Olbrich, W. Eder, D. R. Yakovlev, V. Kolkovsky, W. Zaleszczyk, G. Karczewski, T. Wojtowicz, and D. Weiss, *Spin currents in diluted magnetic semiconductors*, Phys. Rev. Lett. **102**, 156602 (2009).
- [57] P. Olbrich, J. Allerdings, V. V. Bel'kov, S. A. Tarasenko, D. Schuh, W. Wegscheider, T. Korn, C. Schüller, D. Weiss, and S. D. Ganichev, *Magnetogyrotropic photogalvanic effect and spin dephasing in (110)-grown GaAs/Al<sub>x</sub>Ga<sub>1-x</sub>As quantum well structures*, Phys. Rev. B **79**, 245329 (2009).
- [58] V. V. Bel'kov, S. D. Ganichev, E. L. Ivchenko, S. A. Tarasenko, W. Weber, S. Giglberger, M. Olteanu, H.-P. Tranitz, S. N. Danilov,

- Petra Schneider, W. Wegscheider, D. Weiss, and W. Prettl, *Magneto-gyrotropic photogalvanic effects in semiconductor quantum wells*, J. Phys.: Condens. Matter **17**, 3405 (2005).
- [59] S. D. Ganichev, E. L. Ivchenko, V. V. Bel'kov, S. A. Tarasenko, M. Sollinger, D. Weiss, W. Wegscheider, and W. Prettl, *Spin-galvanic effect*, Nature (London) **417**, 153 (2002).
- [60] N. S. Averkiev, L. E. Golub, and M. Willander, *Spin relaxation anisotropy in two-dimensional semiconductor systems*, J. Phys.: Condens. Matter **14**, R271 (2002).
- [61] S. D. Ganichev, *The infrared spin-galvanic effect in semiconductor quantum wells*, Physica E **20**, 419 (2004).
- [62] W. Hanle, *Über magnetische Beeinflussung der Polarisation der Resonanzfluoreszenz*, Zeitschrift für Physik **30**, 93 (1924).
- [63] S. D. Ganichev, E. L. Ivchenko, S. N. Danilov, J. Eroms, W. Wegscheider, D. Weiss, and W. Prettl, *Conversion of Spin into Directed Electric Current in Quantum Wells*, Phys. Rev. Lett. **86**, 4358 (2001).
- [64] S. D. Ganichev, V. V. Bel'kov, Petra Schneider, E. L. Ivchenko, S. A. Tarasenko, W. Wegscheider, D. Weiss, D. Schuh, E. V. Beregin, and W. Prettl, *Resonant inversion of the circular photogalvanic effect in n-doped quantum wells*, Phys. Rev. B **68**, 035319 (2003).
- [65] E. L. Ivchenko and G. E. Pikus, *Superlattices and Other Heterostructures. Symmetry and Optical Phenomena*. Springer, Berlin, 1997.
- [66] G. E. Pikus and A. N. Titkov, *Optical Orientation (Modern Problems in Condensed Matter Sciences)*. North-Holland Physics Publishing, Amsterdam, 1984. (ed. F. Meier and B. P. Zakharchenya).
- [67] J. Fabian and S. Das Sarma, *Spin relaxation of conduction electrons*, J. Vac. Sci. Technol. B **17**, 1708 (1999).

- [68] G. L. Bir, A. G. Aronov, and G. E. Pikus, *Spin relaxation of electrons scattered by holes*, Zh. Eksp. Teor. Fiz. **69**, 1382 (1975).
- [69] M. I. D'yakonov and V. I. Perel', *Spin orientation of electrons associated with the interband absorption of light in semiconductors*, Sov. Phys. JETP **33**, 1053 (1971).
- [70] R. J. Elliott, *Theory of the Effect of Spin-Orbit Coupling on Magnetic Resonance in Some Semiconductors*, Phys. Rev. **96**, 266 (1954).
- [71] Y. Yafet, *Solid State Physics*. Academic, New York, 1963. (ed. F. Seitz and D. Turnbull).
- [72] W. J. H. Leyland, G. H. John, R. T. Harley, M. M. Glazov, E. L. Ivchenko, D. A. Ritchie, I. Farrer, A. J. Shields, and M. Henini, *Enhanced spin-relaxation time due to electron-electron scattering in semiconductor quantum wells*, Phys. Rev. B **75**, 165309 (2007).
- [73] W. Knap, C. Skierbiszewski, A. Zduniak, E. Litwin-Staszewska, D. Bertho, F. Kobbi, J. L. Robert, G. E. Pikus, F. G. Pikus, S. V. Iordanskii, V. Mosser, K. Zekentes, and Yu. B. Lyanda-Geller, *Weak antilocalization and spin precession in quantum wells*, Phys. Rev. B **53**, 3912 (1996).
- [74] F. E. Meijer, A. F. Morpurgo, T. M. Klapwijk, and J. Nitta, *Universal Spin-Induced Time Reversal Symmetry Breaking in Two-Dimensional Electron Gases with Rashba Spin-Orbit Interaction*, Phys. Rev. Lett. **94**, 186805 (2005).
- [75] M. M. Glazov and L. E. Golub, *Nondiffusive Weak Localization in Two-Dimensional Systems with Spin-Orbit Splitting of the Spectrum*, Semiconductors **40**, 1209 (2006).
- [76] S. Hikami, A. Larkin, and Y. Nagaoka, *Spin-orbit interaction and magnetoresistance in the 2 dimensional random system*, Prog. Theor. Phys. **63**, 707 (1980).
- [77] C. A. Brau, *Free-Electron Lasers*, Science **239**, 1115 (1988).

- [78] F. K. Kneubühl and M. W. Sigrist, *Laser*. Teubner, Wiesbaden, 2005.
- [79] O. Svelto, *Principles of lasers*. Plenum Press, New York, 1998.
- [80] T. Y. Chang and T. J. Bridges, *Laser action at 452, 496, and 541  $\mu\text{m}$  in optically pumped  $\text{CH}_3\text{F}$* , *Optics Commun.* **1**, 423 (1970).
- [81] K. J. Button, *Pulsed Optically Pumped Far Infrared Lasers*. in *Infrared and Millimeter Waves Vol. 1: Sources of Radiation*, p. 129, ed. K. J. Button, (Academic Press Inc., London, 1979).
- [82] D. G. Biron, R. J. Temkin, B. Lax, and B. G. Danly, *High-intensity  $\text{CO}_2$  laser pumping of a  $\text{CH}_3\text{F}$  Raman FIR laser*, *Opt. Lett.* **4**, 381 (1979).
- [83] D. G. Biron, B. G. Danly, R. J. Temkin, and B. Lax, *Far-Infrared Raman Laser with High Intensity Laser Pumping*, *IEEE J. Quantum Electron.* **17**, 2146 (1981).
- [84] G. W. Chantry, *Long-wave optics Vol. 2: Applications*. Academic Press, London, 1984.
- [85] M. Born and E. Wolf, *Principles of optics*. Pergamon Press, Oxford, 1964.
- [86] S. D. Ganichev, W. Weber, J. Kiermaier, S. N. Danilov, P. Olbrich, D. Schuh, W. Wegscheider, D. Bougeard, G. Abstreiter, and W. Prettl, *All-electric detection of the polarization state of terahertz laser radiation*, *J. Appl. Phys.* **103**, 114504 (2008).
- [87] S. N. Danilov, B. Wittmann, P. Olbrich, W. Eder, W. Prettl, L. E. Golub, E. V. Beregunin, Z. D. Kvon, N. N. Mikhailov, S. A. Dvoretzky, V. A. Shalygin, N. Q. Vinh, A. F. G. van der Meer, B. Murdin, and S. D. Ganichev, *Fast detector of the ellipticity of infrared and terahertz radiation based on  $\text{HgTe}$  quantum well structures*, *J. Appl. Phys.* **105**, 013106 (2009).
- [88] W. Zinth and H. J. Körner, *Physik III*. Oldenbourg, München, 1998.

- [89] E. V. Loewenstein, R. R. Smith, and R. L. Morgan, *Optical Constants of Far Infrared Materials. 2: Crystalline Solids*, Appl. Opt. **12**, 398 (1973).
- [90] F. Brehat and B. Wyncke, *Measurement of the optical constants of crystal quartz at 10 K and 300 K in the far infrared spectral range*, Int. J. Infrared Milli. **18**, 1663 (1997).
- [91] S. Faniel, T. Matsuura, S. Mineshige, Y. Sekine, and T. Koga, *Determination of spin-orbit coefficients in semiconductor quantum wells*, Phys. Rev. B **83**, 115309 (2011).
- [92] T. Heinzl, *Mesoscopic Electronics in Solid State Nanostructures*. WILEY-VCH, Weinheim, 2003.
- [93] L. Pfeiffer, K.W. West, H.L. Stormer, J.P. Eisenstein, K.W. Baldwin, D. Gershoni, and J. Spector, *Formation of a high quality two-dimensional electron gas on cleaved GaAs*, Appl. Phys. Lett. **56**, 1697 (1990).
- [94] S. Datta and B. Das, *Electronic analog of the electro-optic modulator*, Appl. Phys. Lett. **56**, 665 (1990).
- [95] T. D. Stanescu and V. Galitski, *Spin relaxation in a generic two-dimensional spin-orbit coupled system*, Phys. Rev. B **75**, 125307 (2007).
- [96] J. D. Koralek, C. P. Weber, J. Orenstein, B. A. Bernevig, S.-C. Zhang, S. Mack, and D. D. Awschalom, *Emergence of the persistent spin helix in semiconductor quantum wells*, Nature **458**, 610 (2009).
- [97] M. Duckheim, D. Loss, M. Scheid, K. Richter, I. Adagideli, and P. Jacquod, *Spin accumulation in diffusive conductors with Rashba and Dresselhaus spin-orbit interaction*, Phys. Rev. B **81**, 085303 (2010).
- [98] M. C. Lüffe, J. Kailasvuori, and T. S. Nunner, *Relaxation mechanisms of the persistent spin helix*, Phys. Rev. B **84**, 075326 (2011).

- [99] F. G. Pikus and G. E. Pikus, *Conduction-band spin splitting and negative magnetoresistance in  $A_3B_5$  heterostructures*, Phys. Rev. B **51**, 16928 (1995).
- [100] O. Zaitsev, D. Frustaglia, and K. Richter, *Semiclassical theory of weak antilocalization and spin relaxation in ballistic quantum dots*, Phys. Rev. B **72**, 155325 (2005).
- [101] P. Wenk and S. Kettmann, *Direction dependence of spin relaxation in confined two-dimensional systems*, Phys. Rev. B **83**, 115301 (2011).
- [102] S. D. Ganichev, S. A. Emel'yanov, and I. D. Yaroshetskii, *Spectral sign inversion of photon drag at far-IR wavelengths*, Sov. Phys. JETP Lett. **35**, 368 (1982).
- [103] S. V. Iordanskii, Yu. B. Lyanda-Geller, and G. E. Pikus, *Weak localization in quantum wells with spin-orbit interaction*, JETP Lett. **60**, 206 (1994).
- [104] M. Wimmer and K. Richter, *Optimal block-tridiagonalization of matrices for coherent charge transport*, J. Comput. Phys. **228**, 8548 (2009).
- [105] L. D. Landau and E. M. Lifshits, *Statistical Physics, Third Edition, Part 1: Volume 5 (Course of Theoretical Physics, Volume 5)*. Butterworth-Heinemann, Oxford, 1980.
- [106] E. I. Rashba and M. D. Sturge, *Excitons*. (North-Holland, Amsterdam, 1982).
- [107] J. F. Dai, H. Z. Lu, C. L. Yang, S. Q. Shen, F. C. Zhang, and X. D. Cui, *Magnetoelectric Photocurrent Generated by Direct Interband Transitions in InGaAs/InAlAs Two-Dimensional Electron Gas*, Phys. Rev. Lett. **104**, 246601 (2010).
- [108] S. D. Ganichev, Petra Schneider, V. V. Bel'kov, E. L. Ivchenko, S. A. Tarasenko, W. Wegscheider, D. Weiss, D. Schuh, B. N. Murdin, P. J. Phillips, C. R. Pidgeon, D. G. Clarke, M. Merrick, P. Murzyn, E. V.

- Beregulin, and W. Prettl, *Spin galvanic effect due to optical spin orientation*, Phys. Rev. B **68**, 081302 (2003).
- [109] M. I. Dyakonov, *Basics of Semiconductor and Spin Physics*. in *Spin Physics in Semiconductors*, p. 1, ed. M. I. Dyakonov (Springer, Berlin, 2008).
- [110] M. W. Wu, J. H. Jiang, and M. Q. Weng, *Spin dynamics in semiconductors*, Phys. Rep. **493**, 61 (2010).
- [111] J. B. Miller, D. M. Zumbühl, C. M. Marcus, Y. B. Lyanda-Geller, D. Goldhaber-Gordon, K. Campman, and A. C. Gossard, *Gate-Controlled Spin-Orbit Quantum Interference Effects in Lateral Transport*, Phys. Rev. Lett. **90**, 076807 (2003).
- [112] L. Meier, G. Salis, I. Shorubalko, E. Gini, S. Schön, and K. Ensslin, *Measurement of Rashba and Dresselhaus spin-orbit magnetic fields*, Nature Physics **3**, 640 (2007).
- [113] D. Stich, J. H. Jiang, T. Korn, R. Schulz, D. Schuh, W. Wegscheider, M. W. Wu, and C. Schüller, *Detection of large magnetoanisotropy of electron spin dephasing in a high-mobility two-dimensional electron system in a [001] GaAs/Al<sub>x</sub>Ga<sub>1-x</sub>As quantum well*, Phys. Rev. B **76**, 073309 (2007).
- [114] J. L. Cheng, M. W. Wu, and I. C. da Cunha Lima, *Anisotropic spin transport in GaAs quantum wells in the presence of competing Dresselhaus and Rashba spin-orbit coupling*, Phys. Rev. B **75**, 205328 (2007).
- [115] M. Scheid, M. Kohda, Y. Kunihashi, K. Richter, and J. Nitta, *All-Electrical Detection of the Relative Strength of Rashba and Dresselhaus Spin-Orbit Interaction in Quantum Wires*, Phys. Rev. Lett. **101**, 266401 (2008).
- [116] L. Meier, G. Salis, E. Gini, I. Shorubalko, and K. Ensslin, *Two-dimensional imaging of the spin-orbit effective magnetic field*, Phys. Rev. B **77**, 035305 (2008).

- [117] Y. Kunihashi, M. Kohda, and J. Nitta, *Enhancement of Spin Lifetime in Gate-Fitted InGaAs Narrow Wires*, Phys. Rev. Lett. **102**, 226601 (2009).
- [118] P. S. Eldridge, J. Hübner, S. Oertel, R. T. Harley, M. Henini, and M. Oestreich, *Spin-orbit fields in asymmetric (001)-oriented GaAs/Al<sub>x</sub>Ga<sub>1-x</sub>As quantum wells*, Phys. Rev. B **83**, 041301(R) (2011).
- [119] I. A. Yugova, A. Grelich, D. R. Yakovlev, A. A. Kiselev, M. Bayer, V. V. Petrov, Yu. K. Dolgikh, D. Reuter, and A. D. Wieck, *Universal behavior of the electron  $g^*$ -factor in GaAs/Al<sub>x</sub>Ga<sub>1-x</sub>As quantum wells*, Phys. Rev. B **75**, 245302 (2007).
- [120] M. J. Snelling, G. P. Flinn, A. S. Plaut, R. T. Harley, A. C. Tropper, R. Eccleston, and C. C. Phillips, *Magnetic  $g$ -factor of electrons in GaAs/AlGaAs quantum wells*, Phys. Rev. B **44**, 11345 (1991).
- [121] E. L. Ivchenko, A. A. Kiselev, and M. Willander, *Electronic  $g^*$ -factor in biased quantum wells*, Sol. St. Com. **102**, 375 (1997).
- [122] E. A. de Andrada e Silva, G. C. La Rocca, and F. Bassani, *Spin-orbit splitting of electronic states in semiconductor asymmetric quantum wells*, Phys. Rev. B **55**, 16293 (1997).
- [123] C. Drexler, V. V. Bel'kov, B. Ashkinadze, P. Olbrich, C. Zoth, V. Lechner, Ya. V. Terent'ev, D. R. Yakovlev, G. Karczewski, T. Wojtowicz, D. Schuh, W. Wegscheider, and S. D. Ganichev, *Spin polarized electric currents in semiconductor heterostructures induced by microwave radiation*, Appl. Phys. Lett. **97**, 182107 (2010).
- [124] M. Oestreich and W. W. Rühle, *Temperature Dependence of the Electron Landé  $g$  Factor in GaAs*, Phys. Rev. Lett. **74**, 2315 (1995).
- [125] W. Zawadzki, P. Pfeffer, R. Bratschitsch, Z. Chen, S. T. Cundiff, B. N. Murdin, and C. R. Pidgeon, *Temperature dependence of the electron spin  $g$  factor in GaAs*, Phys. Rev. B **78**, 245203 (2008).

- [126] L. E. Golub, *New Mechanism of the Spin-Galvanic Effect*, JETP Lett. **85**, 393 (2007).

## Danksagung

Ich möchte mich an dieser Stelle ganz herzlich bei allen bedanken, die mich während der Promotion begleitet und zum Gelingen dieser Dissertation maßgeblich beigetragen haben.

Besonders möchte ich Sergey Ganichev danken, in dessen Arbeitsgruppe ich diese Doktorarbeit anfertigen durfte und der dieses interessante Thema an mich vergeben hat. Stets opferte er seine wertvolle Zeit, um meine Fragen zur Theorie und zum Experiment zu beantworten.

Im weiteren bedanke ich mich bei meinen Eltern und Großeltern, die mir mein Physikstudium ermöglicht haben und immer hinter mir stehen.

Einen weiteren Dank möchte ich an Sergey Danilov und Vasily Bel'kov aussprechen, die mir bezüglich des experimentellen Aufbaus und der durchgeführten Experimente immer gute und nützliche Ratschläge erteilen konnten. Ganz herzlich möchte ich mich auch für die theoretische Unterstützung von Eugeneous Ivchenko, Sergey Tarasenko und Leonid Golub bedanken.

Weiterhin geht mein Dank auch an alle meine Kollegen und die Ehemaligen der Arbeitsgruppe, sie waren immer für anregende Diskussionen bereit und sorgten für das hervorragende Arbeitsklima der AG Ganichev. Zu allererst danke ich hierbei meinen Diplomanden Sebastian Stachel, Faina Lomakina, Ines Caspers und Christoph Schönhuber für die tolle Zusammenarbeit. Für das Korrekturlesen möchte ich Peter Olbrich und Sebastian Stachel danken. Darüberhinaus geht mein Dank an Johannes Karch, Christoph Drexler, Tina Zoth, Christina Reitmaier, Thomas Stangl, Florian Müller, Marion Hirmer, Peter Lutz, Ursula Hagner, Patricia Vierling, Markus Fehrenbacher, Josef Kamann, Thomas Schönberger, Bernhard Wittmann, Michael Schmalzbauer, Chonyung Jiang, Cynthia Karl, Wolfgang Weber, Juri Allerdings, Wolfgang Eder, Christoph Brinsteiner, Helgi Diehl, Daniel Plohmann und Stephan Giglberger. Für die technische und formale Unterstützung bedanke ich mich bei Anton Humbs, Ulla Turba, Claudia Rahm und Hannelore Lanz.

Last but not least danke ich besonders meinen Freunden - ihr wisst wer gemeint ist. Kochen, Klettern und Kaffeeklatsch war und ist immer wieder wunderbar mit euch und ein toller Ausgleich zur Doktorarbeit.